

FINITE-ELEMENT MODELLING OF THE HUMAN MIDDLE EAR

McGill University,
Montréal, Québec

February 2005

A thesis submitted to the Faculty of Graduate Studies and Research in partial
fulfilment of the requirements for the degree of

Master of Engineering

© Chadia Mikhael, 2005

ABSTRACT

Most models of the middle ear are based on oversimplified geometries and iterative material-property fitting to experimental data which may yield physiologically incorrect estimates.

The aim of our work was to build an accurate human middle-ear finite-element model that is based on accurate geometry and *a priori* material-property estimates.

A human temporal-bone specimen was obtained for which the middle-ear response had been measured by means of laser Doppler vibrometry. High-resolution micro-computed tomography data for the specimen were used for accurately defining structure geometry. This model comprises the tympanic membrane, the ossicles, two joints, and four ligaments. We assigned estimated material-property values derived from the literature.

We compared the response of our model with those of other human middle-ear models, and with experimental measurements including those from the same ear. Sensitivity of the model to several of its parameters was also investigated.

RÉSUMÉ

Étant basés sur des géométries trop simplifiées et sur des itérations des propriétés matérielles épousant les données expérimentales, la plupart des modèles de l'oreille moyenne pourraient fournir des estimations physiologiques erronées.

Le but de notre travail était d'élaborer un modèle aux éléments finis précis de l'oreille moyenne humaine, basé sur une géométrie précise et des estimations *a priori* des propriétés matérielles.

La réponse de l'oreille moyenne d'un os temporal humain a été mesurée à l'aide d'un vibromètre Doppler à laser. Le spécimen a été balayé avec un appareil à microtomographie par ordinateur à haute résolution. Les données ainsi obtenues ont servi pour préciser la structure géométrique. Ce modèle est composé de la membrane tympanique, les osselets, deux articulations, et quatre ligaments. Nous avons utilisé les valeurs des propriétés matérielles provenant de la littérature pour le modèle.

La réponse de notre modèle a été comparée à d'autres modèles de l'oreille moyenne humaine, et à des mesures expérimentales incluant ceux de l'oreille même. La sensibilité du modèle à plusieurs de ses paramètres a aussi été examinée.

ACKNOWLEDGEMENTS

I would like to thank my supervisor, Professor W. Robert J. Funnell for all his guidance and support throughout this work, and for his patience while editing the many drafts of my thesis.

I am also thankful for all the great friends I met in the BioMedical Engineering department. Thanks to them, this experience has been an enjoyable one. I am especially grateful for Fadi, Jessica, Mackenzie, and Nidal who patiently revised my work.

I am forever indebted to my parents Said and Fifi Mikhael, my brother George and my sister Sana for their unconditional love and support, and for encouraging me to pursue my dreams, no matter how impossible they seemed.

I also would like to thank M. Bance and René van Wijhe, of Dalhousie University, for the middle-ear specimen and the corresponding vibration measurements.

This work was supported by the Canadian Institutes of Health Research (CIHR) and the Natural Sciences and Engineering Research Council of Canada (NSERC).

TABLE OF CONTENTS

CHAPTER 1	1
INTRODUCTION	1
CHAPTER 2	3
ANATOMY OF THE EAR	3
2.1 OUTER EAR	3
2.2 MIDDLE EAR	4
2.2.1 Tympanic Membrane	5
2.2.2 Middle-Ear Spaces	7
2.2.3 Malleus	8
2.2.4 Incus	10
2.2.5 Stapes	11
2.2.6 Ossicular Articulations.....	12
2.2.6.1 Incudomalleal articulation	12
2.2.6.2 Incudostapedial articulation	14
2.2.7 Middle-Ear Muscles.....	14
2.2.7.1 Tensor tympani muscle.....	15
2.2.7.2 Stapedius muscle.....	15
2.2.7.3 Smooth muscle in the fibrocartilaginous ring	15
2.2.8 Middle-Ear Ligaments.....	16
2.2.8.1 TM-malleus attachment	16
2.2.8.2 Malleal ligaments	18
2.2.8.3 Incudal ligaments	19
2.2.8.4 Ligament visibility study.....	19
2.3 INNER EAR	20
CHAPTER 3	24
MECHANICS OF THE MIDDLE-EAR	24
3.1 TRANSFORMER MECHANISM	24
3.2 EXPERIMENTAL OBSERVATIONS	25
3.2.1 Tympanic Membrane	25
3.2.2 Ossicular Chain	26
3.2.3 Samples of Experimental Measurements	28
3.3 FINITE-ELEMENT MODELS	29
CHAPTER 4	35
THE FINITE-ELEMENT METHOD	35
4.1 INTRODUCTION	35
4.2 HISTORY OF THE FINITE-ELEMENT METHOD	36

4.3 FINITE-ELEMENT MESH.....	37
4.3.1 Choosing the Mesh Resolution	37
4.3.2 Element Types	37
4.4 MECHANICS FUNDAMENTALS	38
4.4.1 Nodal Degrees of Freedom.....	38
4.4.2 Strains and Stresses in 2-D Problems	39
4.4.3 Young's Modulus.....	40
4.4.4 Poisson's Ratio.....	41
4.5 THE VARIATIONAL METHOD	41
CHAPTER 5	45
METHODS.....	45
5.1 X-RAY MICRO-COMPUTED TOMOGRAPHY.....	45
5.1.1 Introduction	45
5.1.2 Micro-CT Data	47
5.2 HISTOLOGY	47
5.3 LASER DOPPLER VIBROMETRY	48
5.3.1 Introduction	48
5.3.2 Vibrometry Measurements	49
5.4 SEGMENTATION	50
5.4.1 Introduction	50
5.4.2 Snake Algorithm	51
5.4.3 Fie	51
5.4.4 Segmentation Guidelines	52
5.4.5 Open and Closed Contours	52
5.4.6 Tr3 Text File	53
5.4.6.1 Contour attributes	54
5.4.6.2 Connecting contours	54
5.4.6.3 Closing openings at the ends of structures.....	57
5.4.6.4 Subsets	58
5.4.6.5 Material properties	58
5.4.6.6 Thickness.....	59
5.5 MESH GENERATION	60
5.5.1 Mesh	61
5.5.2 Bandwidth	63
5.6 SENSITIVITY ANALYSIS	63
CHAPTER 6	64
THE FINITE-ELEMENT MODEL	64
6.1 INTRODUCTION	64
6.2 PRELIMINARY MODEL	64
6.2.1 Tympanic Membrane	64
6.2.2 Ossicles	66

6.2.2.1 <i>Malleus</i>	66
6.2.2.2 <i>Incus</i>	66
6.2.2.3 <i>Stapes</i>	66
6.2.3 Ligaments and Joints	67
6.2.3.1 <i>Malleolar ligaments</i>	67
6.2.3.2 <i>Incudal ligaments</i>	67
6.2.3.3 <i>Stapes annular ligament</i>	67
6.2.3.4 <i>Ligament attaching the TM to the malleus</i>	68
6.2.3.5 <i>Incudomalleolar joint</i>	69
6.2.3.6 <i>Incudostapedial joint</i>	69
6.2.4 Muscles and Tendons	69
6.3 CONVERGENCE TEST	70
6.3.1 Number of Elements Per Diameter and Displacements.....	70
6.3.2 Slice Spacing and Displacements.....	72
6.3.3 The Selected Mesh.....	73
6.4 THE FINAL MODEL	74
6.4.1 Stapedial Annular Ligament	75
6.4.2 Incudomalleolar Joint	76
6.4.3 Muscles	76
6.5 LOADING	76
CHAPTER 7	77
RESULTS.....	77
7.1 INTRODUCTION	77
7.2 DISPLACEMENTS OF THE FINITE-ELEMENT MODEL.....	77
7.2.1 Eardrum Displacements.....	77
7.2.2 Axis of Rotation and Incudomalleolar Displacements	79
7.2.3 Stapes Displacement.....	82
7.3 PARAMETER SENSITIVITY	84
7.3.1 Sensitivity Analysis.....	84
7.3.2 Effect of TM-Malleus Attachment	87
7.4 COMPARISON WITH EXPERIMENTAL MEASUREMENTS.....	87
7.5 COMPARISON WITH OTHER FINITE-ELEMENT MODELS.....	89
7.6 DISCUSSION	89
CHAPTER 8	91
CONCLUSION	91
8.1 SUMMARY.....	91
8.2 FUTURE WORK.....	92
REFERENCES	95
APPENDIX A	108

LIST OF FIGURES

FIGURE	PAGE
2.1 The human ear consists of the outer, middle and inner ears.	3
2.2 Human middle ear - eardrum, ossicular chain, ligaments, muscles and tendons.	4
2.3 The tympanic membrane is composed the pars flaccida and the pars tensa.	5
2.4 The pars tensa consists of three layers: epidermis, lamina propria and mucosa.	6
2.5 A cross-section of the fibrocartilaginous ring in moustached bats.	7
2.6 The different regions of the middle ear.	8
2.7 A VRML model of the malleus, its ligaments and the tensor tympani muscle.	9
2.8 Average dimensions of the human malleus.	9
2.9 The incus includes the body and the short, long and lenticular processes.	10
2.10 Average incudal dimensions.	11
2.11 Average stapes dimensions.	12
2.12 The incudomalleal joint.	13
2.13 A close-up of the incudostapedial articulation.	14
2.14 TM-malleus ligament sections taken at several places along manubria.	17
2.15 A schematic representation of the inner-ear components.	20
3.1 Cross-sections of the TM taken along the manubrium.	26
3.2 The rotational axis of the malleus and incus.	27
3.3 Umbo and stapes displacements measured by Gyo et al. (1987).	31
3.4 A comparison between calculated (Koike et al., 2002) and measured (Gyo et al., 1987) umbo and stapes displacements, at 80 dB SPL.	31
4.1 Types of elements that can constitute a mesh.	38
5.1 Micro-CT scanner.	46
5.2 General setup of a laser Doppler vibrometer.	49
5.3 Examples of closed and open contours in Fie.	53
5.4 A screenshot from the mesh-generation software, Tr3.	55
5.5 A mesh of the tympanic membrane and the TM-malleus attachment.	56
5.6 A cylinder triangulated using 4 different resolutions.	62
6.1 VRML representation of the preliminary version of our middle-ear model.	65
6.2 A VRML model of the TM, the malleus and the TM-malleus attachment.	69
6.3 Convergence test for the middle ear: <i>xy</i> -resolution and corresponding maximum pars-tensa displacement.	71
6.4 Convergence test for the middle ear: <i>xy</i> -resolution and corresponding maximum stapes displacement.	71
6.5 Convergence test for the middle ear: <i>z</i> -resolution and corresponding maximum pars-tensa displacement.	72

6.6	Convergence test for the middle ear: z -resolution and corresponding maximum stapes displacement.	73
6.7	The effect of the preliminary model's mesh resolution on computation time.	74
6.8	A VRML representation of the final version of our model.	75
7.1	TM's response (medial view) to a static pressure of 1 Pa as viewed in Fod.	78
7.2	A medial view of ossicular chain displacement.	79
7.3	Ossicular displacements along the direction that is normal to the footplate.	80
7.4	A VRML model showing malleus and incus rotation (supero-anterior view).	81
7.5	Displacement vectors at the footplate are normal to the surface.	82
7.6	Varying magnitudes of displacement across the footplate.	83
7.7	Displacement of the ossicles along an axis that is normal to the footplate.	84
7.8	Sensitivity of the pars tensa to nine parameters.	85
7.9	Footplate sensitivity to nine parameters.	85
7.10	Sensitivity of footplate displacement to Y_{isj} .	86
7.11	Sensitivity of footplate displacement to Y_{sal} .	87

CHAPTER 1

INTRODUCTION

According to the World Health Organization, approximately 250 million people currently suffer from hearing loss, three million of whom reside in Canada (WHO, 2001). Because the population is rapidly aging, the number of hearing-impairment diagnoses is also quickly rising.

To better diagnose and treat this condition, it is essential to understand the mechanics of hearing. The mammalian ear comprises the outer, middle and inner ears. The main focus of this thesis will be on the middle ear, in particular that of human adults. One approach to studying middle-ear mechanics is computer analysis techniques which yield quantitative models. Such models are classified into lumped-parameter models, analytical models and finite-element models; finite-element models are the most popular for handling complex structures.

Once validated, the generated models can serve multiple purposes. These include (1) representing and better understanding the different pathological middle-ear conditions, (2) designing prostheses, and (3) teaching purposes.

Of the numerous middle-ear finite-element models which have been built in the past 30 years, most are based on oversimplified geometries and on iterative alterations of the structures' material-property values. The iterative procedure yields a match between a model's response and the corresponding experimental measurements to which it is being compared; the final material-property values may not, however, be physiologically correct. In addition, additional iterative alterations may be necessary in future simulations where structure modifications are introduced.

The objective of this work was to generate an accurate middle-ear finite-element model without performing the afore-mentioned alterations. This was done by accurately representing the geometry - based on x-ray micro-computed tomography data we obtained - and by relying on *a priori* material-property estimates from the literature. The

final model was validated by comparing its response with existing simulated and experimental measurements; the experimental measurements include measurements from the same middle ear.

The anatomy of the middle ear will be reviewed in Chapter 2. This will be followed by the fundamentals of middle-ear mechanics and a summary of several experimental and simulation results in Chapter 3. Chapter 4 provides a brief introduction to the finite-element method, along with a review of previous middle-ear models. An overview of the techniques that we used for this work is available in Chapter 5. These techniques include x-ray micro-computed tomography, laser Doppler vibrometry, histology, image segmentation, mesh generation and sensitivity analysis. The middle-ear finite-element model is described in Chapter 6, with thorough substructure and corresponding material-property details. In Chapter 7, the static response of the model is presented, and compared with (1) vibrometry of the same middle ear that the model was based on, (2) displacements for other temporal bones, and (3) displacements for other existing models. Sensitivity results of the model are also presented in this chapter. Our work is then summarized in Chapter 8, along with possible enhancements and future applications of this model.

CHAPTER 2

ANATOMY OF THE EAR

The vertebrate ear consists of three parts – the outer ear, middle ear and inner ear. This chapter includes a brief summary of each of the three parts, as they are found in human adults. A more detailed summary will be given for the middle ear, given that it is the main focus of this thesis.

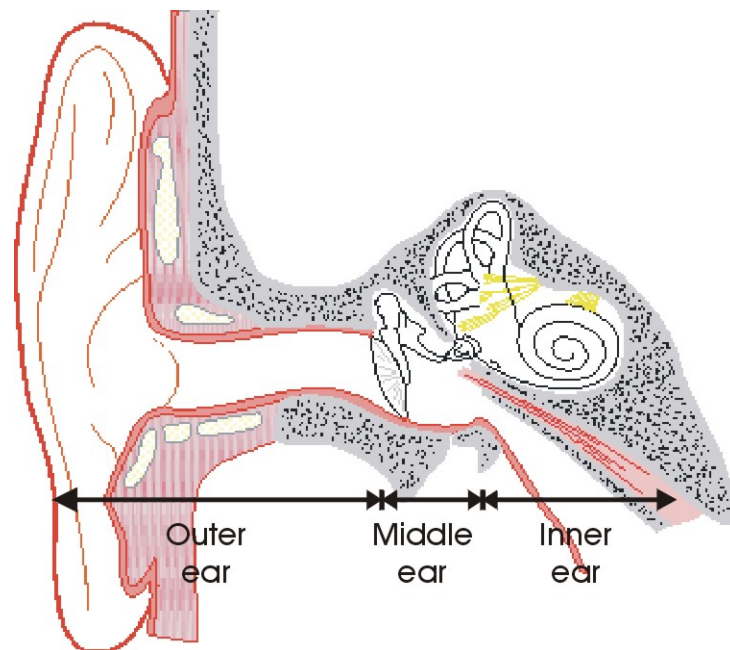


Figure 2.1 The human ear consists of the outer, middle, and inner ears. Modified after http://audilab.bmed.mcgill.ca/~funnell/AudiLab/teach/me_saf/me_saf.html

2.1 OUTER EAR

As seen in Figure 2.1, the outer ear includes the pinna (or auricle), concha, and the external auditory canal. The pinna, a curved and cartilaginous structure, is responsible for the first step in hearing – that of capturing nearby sound waves and directing them into the external auditory canal. Unlike those of many mammals, however, the human pinnae are not movable and lay almost flat against the head. The concha is the hollow bowl-like

portion of the cartilage which determines the angle at which the ear protrudes. The external auditory canal, consisting of a lateral cartilaginous portion and a medial bony portion, connects the outer ear to the middle ear. Sound waves travel through the air medium of the canal towards the eardrum.

2.2 MIDDLE EAR

Figure 2.2 is a schematic representation of the middle ear, an air-filled cavity sealed off by the eardrum laterally and by the stapes footplate medially, and traversed by an ossicular chain consisting of the malleus, incus and stapes. These structures are held in place via numerous ligaments, folds, muscles and tendons. Connecting the middle-ear space to the throat is the Eustachian tube, which equalizes the pressure on both sides of the eardrum.

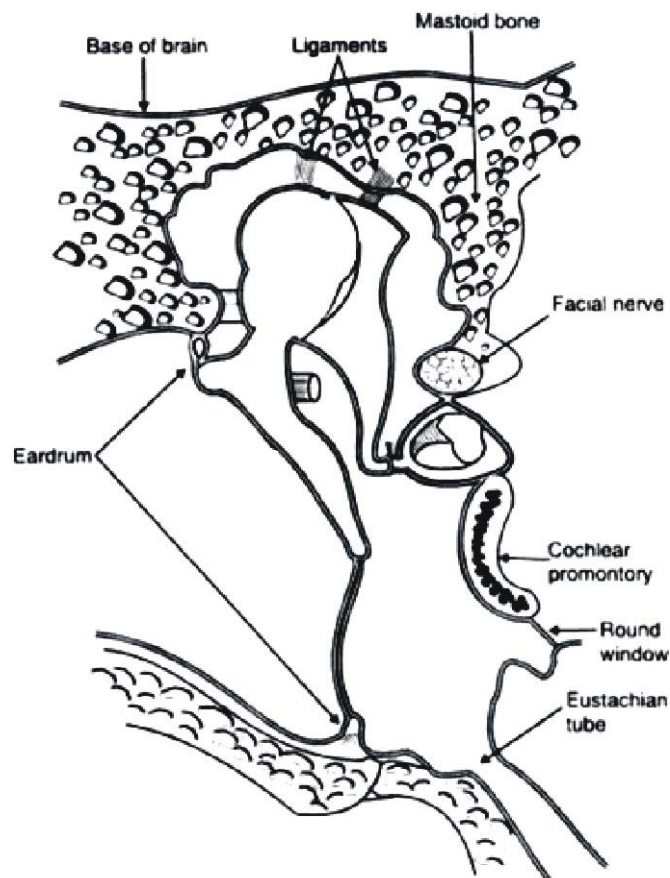


Figure 2.2 The human middle ear is composed of the eardrum, ossicular chain, ligaments, muscles and tendons. <http://hope4hearing.org/anatomy.htm>

2.2.1 Tympanic Membrane

At the end of the external auditory canal is the eardrum, or tympanic membrane (TM), which vibrates in response to the incoming sound waves. This membrane is 8 to 10 mm in diameter (Wever and Laurence, 1954) and somewhat conical in shape, with its apex pointing inwards. It forms an angle of approximately 140° with the superior wall of the external auditory canal (Gulya & Schuknecht, 1995).

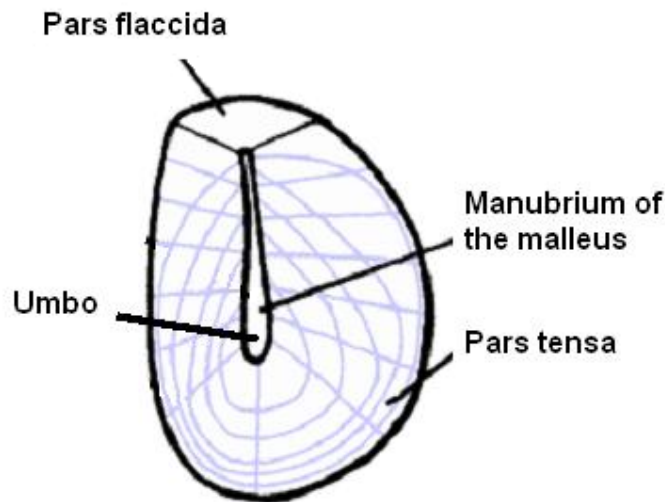


Figure 2.3 The tympanic membrane is composed of two regions: the pars flaccida (30 to 230 μm thick) and the pars tensa (30 to 90 μm thick) (Lim, 1970).

Modified after http://audilab.bmed.mcgill.ca/~funnell/AudiLab/teach/me_saf/me_saf.html

Figure 2.3 is a representation of the two parts of the eardrum – the pars tensa and pars flaccida. The pars tensa membrane is made of three layers – epidermal, mucosal and fibrous layers. The epidermal layer is lateral and continuous with the skin lining of the external auditory canal. The mucosal layer is medial and continuous with the mucosal lining of the middle-ear cavities. Between these two layers is the fibrous layer, or lamina propria. As seen in Figure 2.4, it consists of four layers – subepidermal connective tissue, radial fibres, circular fibres and submucosal connective tissue. The radial and circular fibres give the pars tensa its main stiffness. The pars flaccida, or Shrapnell’s membrane, is also composed of the epidermal, fibrous and mucosal layers. Although it lacks radial

and circular fibres in its fibrous layer (Gulya & Schuknecht, 1995), this membrane is thicker than the pars tensa (Lim, 1970).

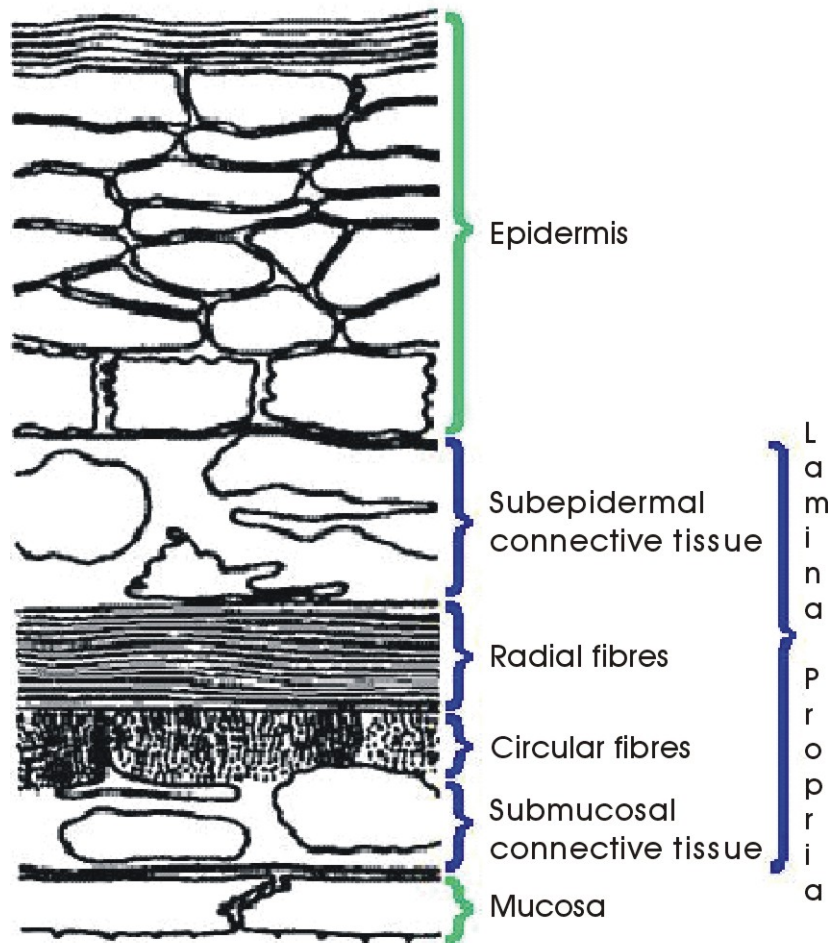


Figure 2.4 The pars tensa consists of three layers: epidermis, lamina propria and mucosa.

http://audilab.bmed.mcgill.ca/~funnell/AudiLab/teach/me_saf/me_saf.html

As portrayed in Figure 2.5, a fibrocartilaginous ring (sometimes referred to as the TM annular ligament) lies between the pars tensa and the tympanic annulus and serves as a connective tissue between them. A cross-section through this area is somewhat triangular in shape. The apex of the triangle, referred to as the apical zone (AZ), is collagenous and is rich in small vessels. The base, or the myovascular zone (MV), contains larger blood vessels and radially arranged muscle fibres (Henson and Henson, 2000), at least in some species.

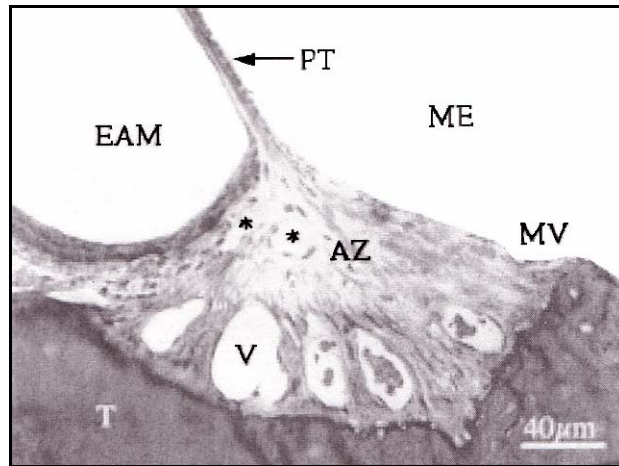


Figure 2.5 A cross-section of the fibrocartilaginous ring in moustached bats. The (upper) apical zone (AZ) connects to the TM, and the (lower) myovascular zone (MV) connects to the tympanic annulus (T). The small blood vessels of the AZ are indicated with asterisks. The relatively larger blood vessels (V) of the MV are surrounded by muscle fibres. EAM: external auditory meatus, ME: middle ear. From Henson and Henson (2000).

2.2.2 Middle-Ear Spaces

The middle-ear space, or tympanic cavity (Figure 2.6), is located in the petrous portion of the temporal bone. It is about 15 mm high and 2 to 4 mm wide – wider at the top than the bottom. This space, measuring approximately 2 cm³, can be divided into the epitymanum, mesotympanum and hypotympanum. The epitymanum consists of the region superior to the eardrum, and includes the malleus head and incus body. The mesotympanum is the area medial to the eardrum and bony tympanic annulus. It houses part of the incus, the stapes, and the two muscles, etc. The hypotympanum is the region inferior to the lowest part of the tympanic annulus.

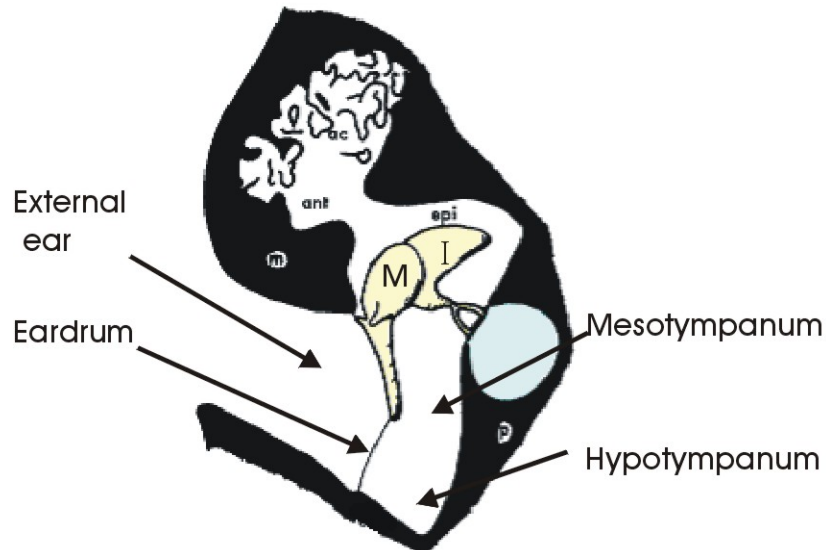


Figure 2.6 The different regions of the middle ear include the epitympanum (epi), mesotympanum, and hypotympanum. M: malleus, I: incus, ac: air cells, ant: antrum, m: mastoid, p: petrous.

Modified after http://audilab.bmed.mcgill.ca/~funnell/AudiLab/teach/me_saf/me_saf.html

2.2.3 Malleus

The malleus, or hammer, displayed in Figure 2.7, is the most lateral bone of the ossicular chain. It includes a head, neck, lateral process, anterior process, and manubrium. From the lateral side, it connects to the TM via a ligament which runs along the entire length of the manubrium (i.e., from the lateral process to the umbo). The medial side of the malleus head articulates with the incus body. The anterior process is a thin bony projection which extends from the neck and is connected to the wall of the petrotympanic fissure by the anterior malleolar ligament. It is sometimes found fractured or partially resorbed in adults, apparently without affecting their hearing (Gulya, 1995). Malleus dimensions reported by Kirikae (1960) are summarized in Figure 2.8.

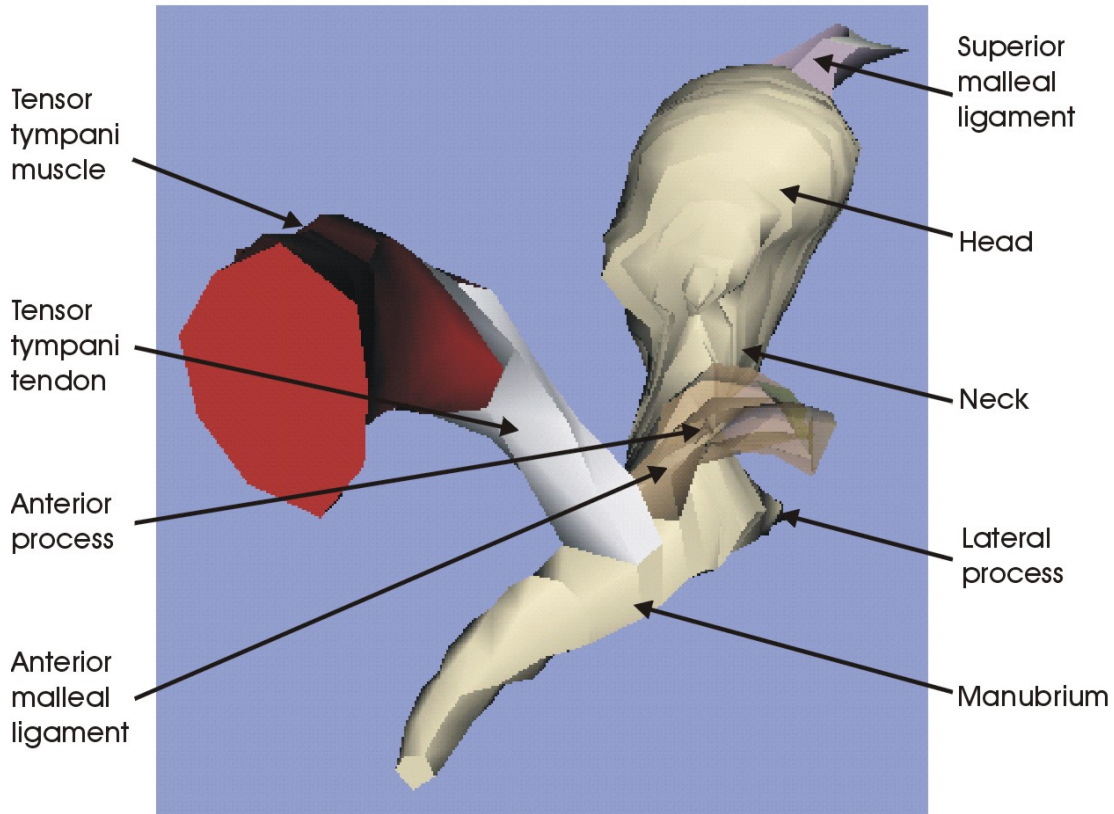


Figure 2.7 A VRML model of the malleus, its ligaments and the tensor tympani muscle. The malleus is composed of the head, neck, lateral process, anterior process and manubrium. Its ligaments include the superior and anterior malleal ligaments.

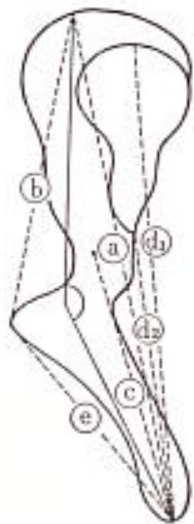


Figure 2.8 Average dimensions of the human malleus based on 714 samples ranging from 9 days to 81 years old: a: $8.01 \pm 0.09\text{mm}$, b: $5.00 \pm 0.10\text{mm}$, c: $4.21 \pm 0.10\text{mm}$, d₁: $7.43 \pm 0.10\text{mm}$, d₂: $4.65 \pm 0.09\text{mm}$, e: $4.51 \pm 0.08\text{mm}$ (Kirikae, 1960, p.61).

The tensor tympani muscle and several ligaments and folds contribute to connecting the malleus to the walls of the middle-ear space. Additional details on these structures will be provided in Sections 2.2.7 and 2.2.8, respectively.

2.2.4 Incus

The second bone in the ossicular chain is the incus, or anvil. It is located between the malleus and stapes, with which it articulates through two synovial joints known as the incudomalleal and incudostapedial joints, respectively. The incus can be divided into the body and the short, long, and lenticular processes. Together with the head of the malleus, the incus body rests in the epitympanum. As seen in Figure 2.9, the short process extends posteriorly, into the posterior incudal recess, and is secured to the posterior wall by the posterior incudal ligament. This strong ligament consists of lateral and medial portions. Detailed dimensions of the incus can be found in Figure 2.10.

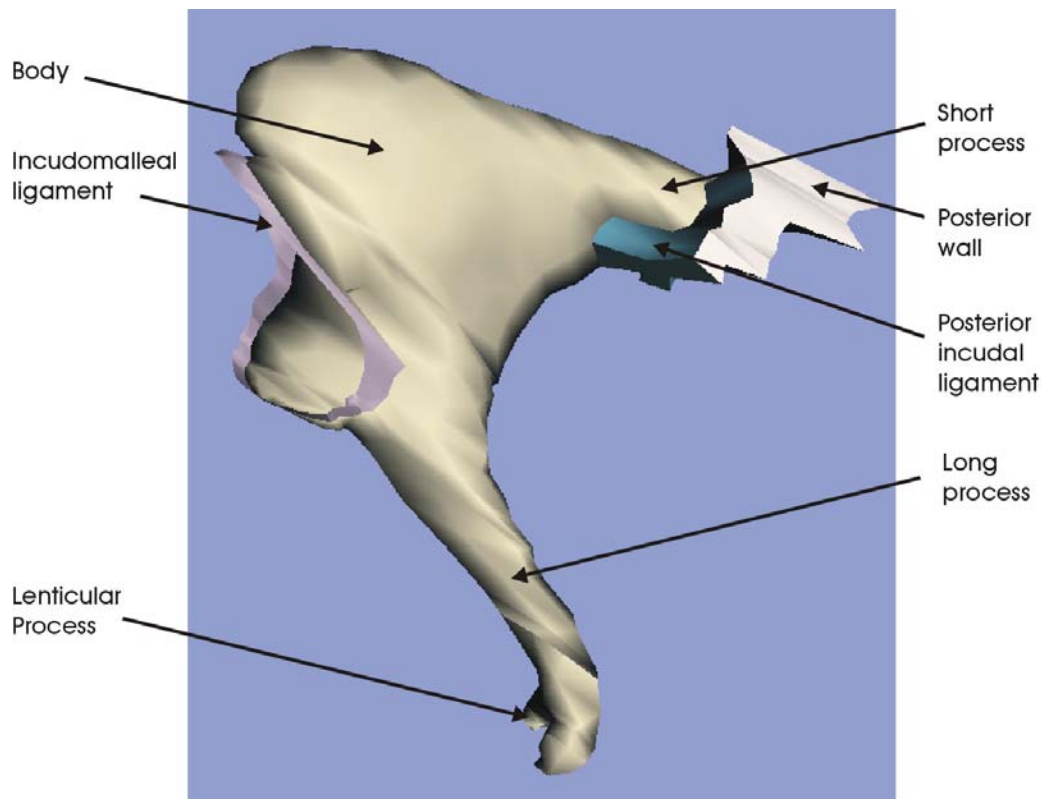


Figure 2.9 The incus includes the body and the short, long and lenticular processes. The concave surface of its body articulates with the malleus head via the incudomalleal joint. Its lenticular process articulates with the stapes head via the incudostapedial ligament.

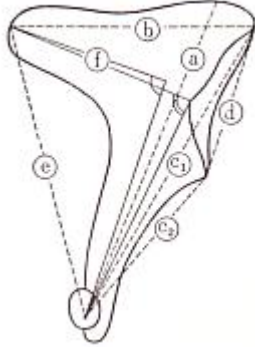


Figure 2.10 Average incudal dimensions based on microscopic observation of 818 human samples whose ages varied from 9 days to 81 years old: a: $6.79 \pm 0.07\text{mm}$, b: $4.81 \pm 0.07\text{mm}$, c: $3.33 \pm 0.06\text{mm}$, d: $3.26 \pm 0.05\text{mm}$, e: $5.99 \pm 0.08\text{mm}$, f: $3.83 \pm 0.09\text{mm}$ (Kirikae, 1960, pp. 61-62).

2.2.5 Stapes

The stapes, or stirrup, depicted in Figure 2.11, is the smallest and most medial ossicle of the middle-ear chain. It includes the head, two crura – the posterior crus and anterior crus – and the footplate. The head connects to the lenticular plate of the incus via the incudostapedial joint, and the footplate connects to the oval window via the fibrous annular ligament. This ligament joins the middle ear to the inner ear, creating the stapediovestibular articulation. The anterior crus is generally straighter than the posterior crus, but both vary in thickness and curvature among individuals. Similarly, various shapes, thicknesses and curvatures have been observed for the footplate (Gulya & Schuknecht, 1995). The average stapes dimensions are shown in Figure 2.11. Emerging from the pyramidal eminence is the stapedius tendon which variably joins the head and/or posterior crus to the stapedius muscle. This muscle is embedded in a bony sulcus located in the posterior wall of the middle-ear cavity.

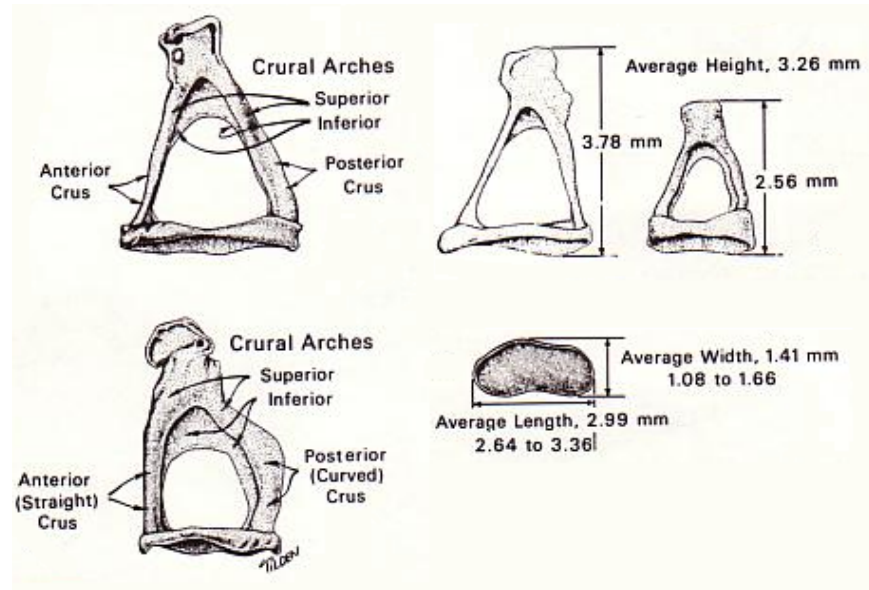


Figure 2.11 Average stapes dimensions (Gulya & Schuknecht, 1995). The stapes includes the head, the footplate, and two crura. The footplate attaches to the oval window, via the annular ligament, thereby moving the cochlear fluid and transmitting the sound energy to the inner ear.

2.2.6 Ossicular Articulations

Each of the middle-ear articulations is composed of a capsule and the cartilage-lined epiphyses of two neighbouring bones. The capsule wraps around the ends of these bones, and unites the periosteum of one to that of the other. Both incudomalleolar and incudostapedial articulations are non-weight-bearing, synovial, and diarthrodial.

2.2.6.1 Incudomalleolar articulation

A capsule wraps around the distal end of the malleus and the medial end of the incus. From the outermost layer to the innermost layer, the capsule includes: a middle-ear mucous membrane, a fibrous layer and a synovial membrane. It is thicker on the superomedial and the latero-inferior aspects where it forms the medial and lateral incudomalleolar ligaments, respectively (see Figure 2.12). These two ligaments are what give the capsule its strength to interlock the linked bones (Gulya & Schuknecht, 1995).

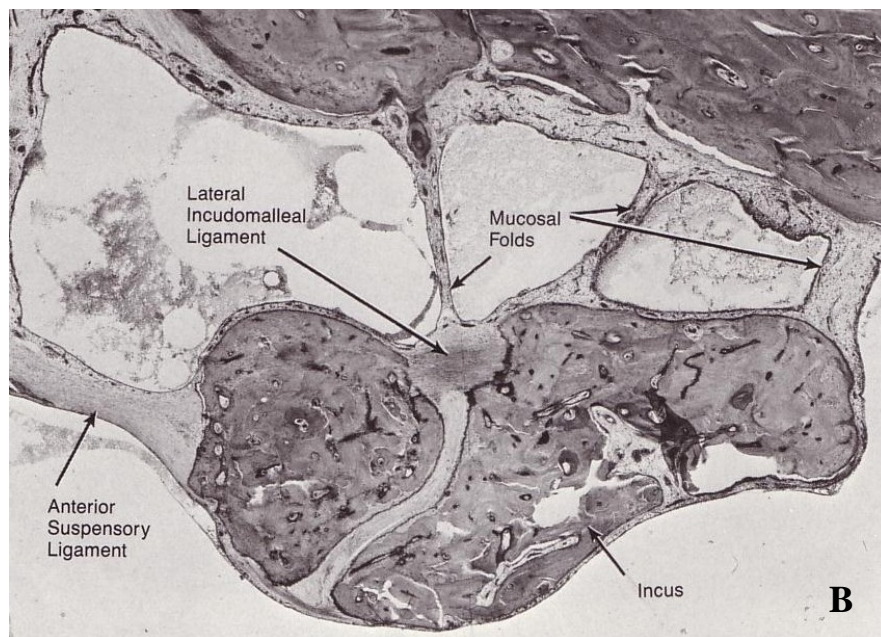
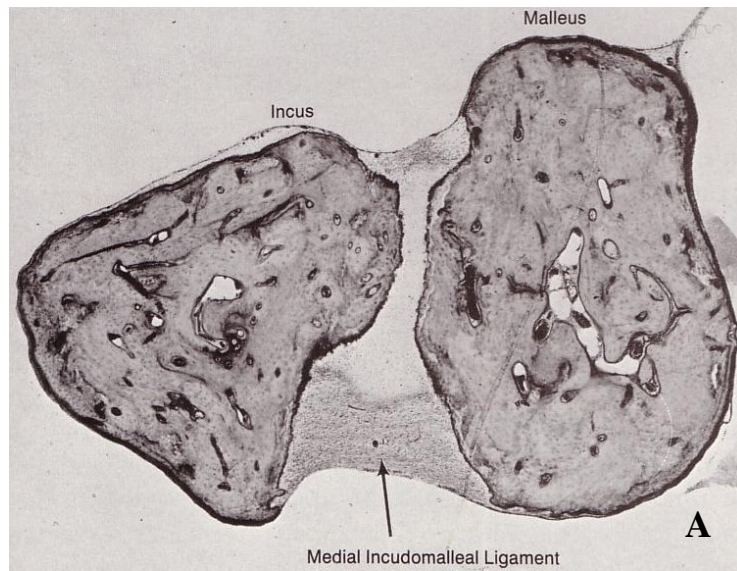


Figure 2.12 The incudomalleal joint consists of a capsule which wraps around the articulating malleal and incudal surfaces. Its strongest fibres form the (A) medial and (B) lateral incudomalleal ligaments (Gulya & Schuknecht, 1995).

2.2.6.2 Incudostapedial articulation

Inside the incudostapedial joint, the convex face of the lenticular process articulates with the concave face of the stapes head. Between the two ossicles, a joint space is noticeable (Figure 2.13), along with the rarely seen interarticular disc (Gulya & Schuknecht, 1995). The posterior capsule fibres are covered by the stapedius tendon with which they strongly fuse (Wolff *et al.*, 1957).

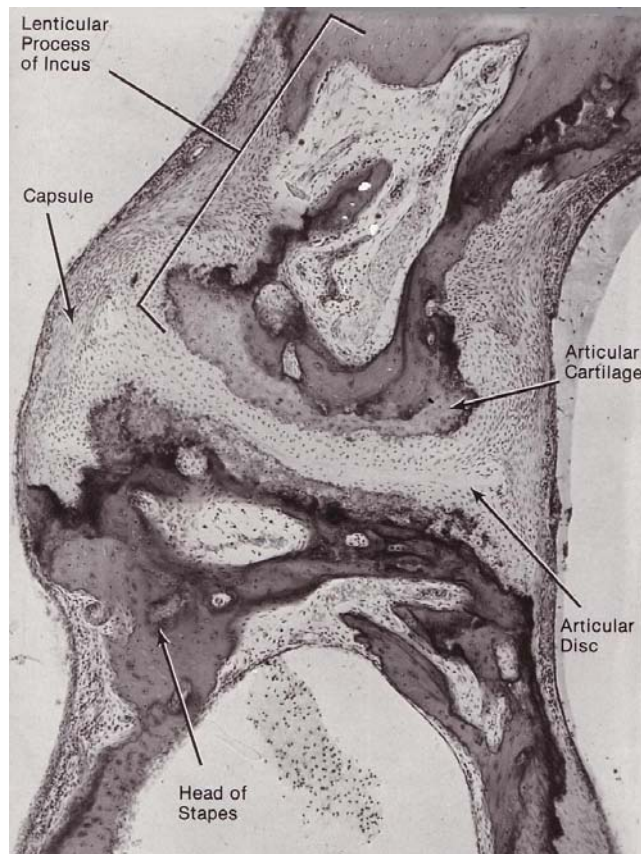


Figure 2.13 A close-up of the incudostapedial articulation. The capsule engulfs the cartilage-lined convex lenticular process and concave stapes head (Gulya & Schuknecht, 1995).

2.2.7 Middle-Ear Muscles

Located in the middle-ear cavity, anchoring the ossicles to the cavity wall, are two muscles, the tensor tympani muscle and stapedius muscle. These muscles usually contract simultaneously as a reflex response to high-intensity sounds, and therefore limit the

amount of mechanical energy transferred to the inner ear. In addition, recent studies have observed smooth muscle fibres located in the fibrocartilaginous ring attaching the pars tensa to the tympanic annulus.

2.2.7.1 Tensor tympani muscle

The tensor tympani (Figure 2.7) is a striated muscle, approximately 2 cm in length. It lies in a bony sheath in the temporal bone, and emerges into the middle-ear space from the anterior wall, where its fibres converge to form the tensor tympani tendon. This tendon joins the muscle to the medial and anterior surfaces of the malleus neck and manubrium. Upon contraction, the manubrium is pulled inward, along with the eardrum, thereby increasing tension at the latter's surface (Gulya & Schuknecht, 1995).

2.2.7.2 Stapedius muscle

This muscle is the smallest skeletal muscle in the human body, and is composed of both striated and non-striated fibres. It emerges from the pyramidal eminence of the posterior or mastoid wall of the tympanic cavity. Its fibres gradually converge to form the stapedius tendon which inserts into the stapes head and/or posterior crus. The muscle is innervated by the facial nerve, and its contraction fixates the stapes footplate and reduces the response of the middle ear (Gulya & Schuknecht, 1995).

2.2.7.3 Smooth muscle in the fibrocartilaginous ring

Recently, Henson and Henson (2000) observed smooth muscles in the basal end of a mustached bat's fibrocartilaginous ring. The muscle fibres were oriented radially, and filled the gaps between the blood vessels, while extending towards the tympanic ring. Henson and Henson suggest that they play a role in adjusting or modifying the tension of the tympanic membrane, but more studies are still needed to determine their exact function(s). Similar findings have also been reported in humans (e.g., Henson, 2001) and gerbils (Yang & Henson, 2002).

2.2.8 Middle-Ear Ligaments

A literature review on middle-ear ligament characterisation, location and naming is summarized in Table 2.1. The references chosen for the review include one terminology standard and four textbooks. As can be deduced from the table, there are disagreements among the authors concerning the naming and existence of certain ligaments, especially the malleal ligaments.

2.2.8.1 TM-malleus attachment

This ligament extends along the entire length of the manubrium and serves as an attachment between the TM and the malleus. It is fibrous at the manubrium ends but composed of mucosal filaments in the mid-region (Gulya & Schuknecht, 1995). Graham *et al.* (1978) reported significant differences in its composition in three regions – the umbo, the mid-manubrium and the upper third of the manubrium below the lateral process – as illustrated in Figure 2.14. At the umbo, they found a very thick layer of lamina propria which divides equally and wraps around the manubrium on both its medial and lateral sides (Figure 2.14A); this region is the strongest of the three. Similar observations were made at the mid-level; here, however, the fibres on the medial side of the manubrium appeared to be thinner (Figure 2.14B). In the upper third below the lateral process, the manubrium was further away from the eardrum, and the attachment was reduced to a mere “stalk” (Figure 2.14C); this region is therefore the weakest.

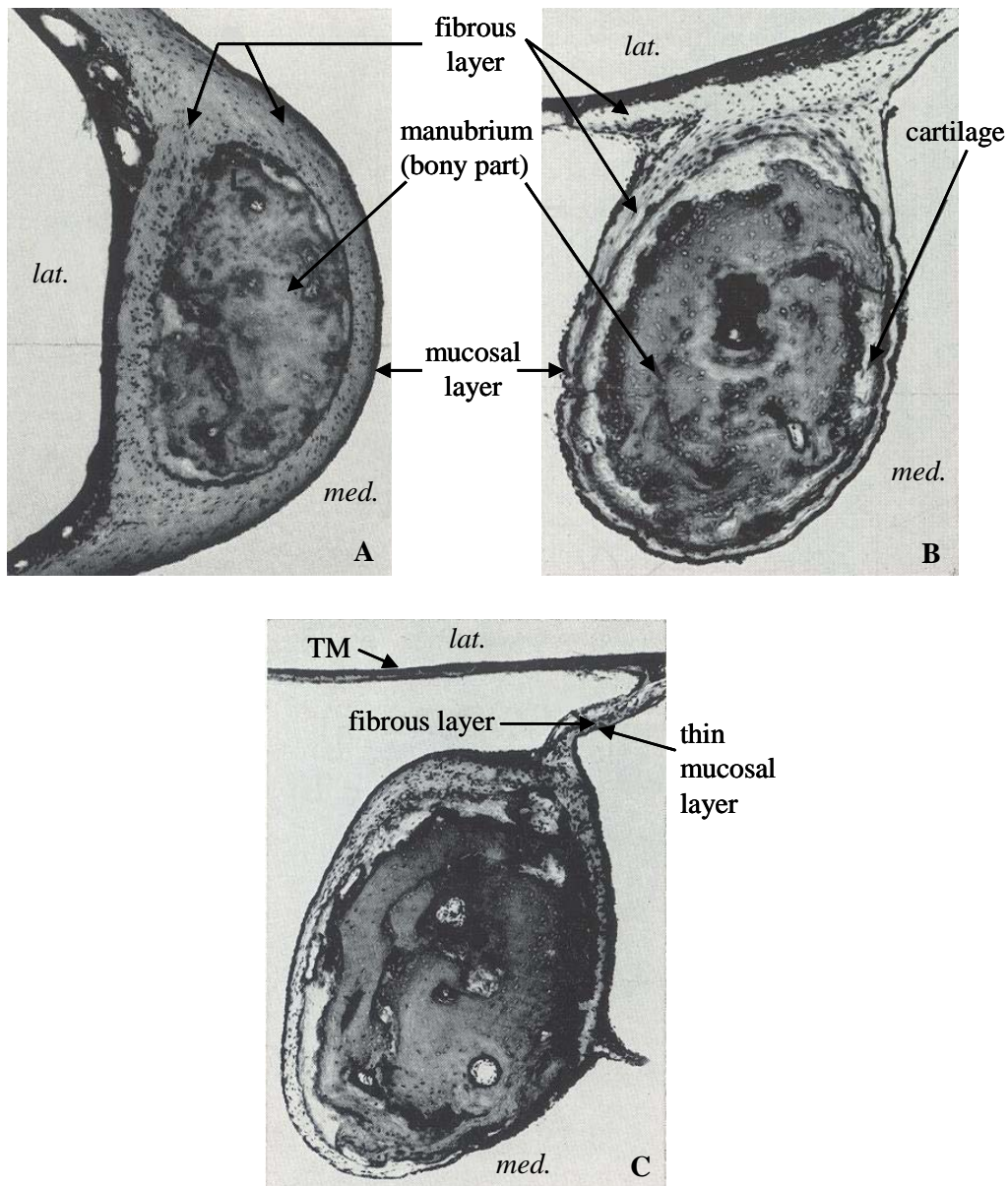


Figure 2.14 After studying TM-malleus ligament sections taken at several places along the manubria of ten human temporal bones, Graham *et al.* (1978) classified the attachment into three regions based on its composition: (A) the umbo region, where the fibres are in abundance and equally distributed about the manubrium, (B) the mid-manubrium region, where fewer fibres are medial to the manubrium, and (C) the upper one-third, where the attachment is its weakest (modified after Graham *et al.*, 1978) (*med.*: medial, *lat.*: lateral).

2.2.8.2 Malleolar ligaments

The largest inter-author differences were seen in descriptions of the malleolar ligaments.

- *Anterior malleolar ligament (AML)*: The AML serves to connect the anterior process of the malleus to the petrotympanic fissure. The majority of the authors are in agreement with its naming and location. Palva *et al.* (2001) also mentions an anterior malleolar ligamental fold which defines the anterior border of the lateral malleolar space.
- *Lateral malleolar ligament (LML)*: The LML is said to fan out laterally from the neck of the malleus to the bony rim of the notch of Rivinus. Palva *et al.* (2001) and Proctor (1989) also mention a lateral malleolar ligamental fold which forms the larger portion of the floor of the lateral malleolar space as well as the roof of Prussak's space.
- *Posterior malleolar ligament (PML)*: Not many authors agree on the existence of such a ligament. Some believe that it represents the thick portion of the posterior malleolar fold extending from the neck to the pretympanic spine (Gulya & Schuknecht, 1995). Others only report the posterior malleolar fold (Proctor, 1989), and some report neither one (e.g., references 4 and 5 of Table 2.1).
- *Superior malleolar ligament (SML)*: Wolff *et al.* (1957) described the SML as the ligament which joins the top of the malleus head to the tegmen tympani. Proctor (1989) reported a superior malleolar fold, in addition to the SML. Some authors, however, did not report either (references 1 and 4 of Table 2.1).
- *Suspensory ligaments*: Greater controversy exists when mentioning ligaments such as the anterior suspensory ligament (ASL), lateral suspensory ligament (LSL), and superior suspensory ligament (SSL). Out of the 6 reviewed references, Gulya and Schuknecht (1995) were the only authors who mentioned all three of these ligaments, which they claimed to play both 'suspensory' and 'damping' roles. The ASL was said to be above the AML, and Palva *et al.* (2001) seem to be in agreement with them. On the other hand, the LSL and SSL were not mentioned by the other authors, and the LML and SML were not mentioned by Gulya and Schuknecht. The LSL and LML, however, have similar insertion points; the SSL and SML also have similar insertion points. Therefore, it appears that all authors are referring to the same ligaments but with a slight difference in the naming.

2.2.8.3 Incudal ligaments

- *Posterior incudal ligament (PIL)*: This ligament is composed of two separate bundles which extend from the lateral and medial sides of the short process of the incus to the posterior incudal recess (Wolff *et al.*, 1957; Gulya & Schuknecht, 1995).
- *Superior incudal ligament (SIL)*: This ligament has only been listed in the International Anatomical Terminology (FCAT, 1998). Although Donaldson *et al.* (1992) indicated the point of attachment of this ligament in their Figure III-38, they did not provide any description of it, or reference to it, throughout their book.

2.2.8.4 Ligament visibility study

A recent study regarding the malleolar and incudal ligaments was done by Lemmerling *et al.*, (1997) using 1-mm-thick computed tomography sections. Two individuals were asked to rate the visibility of the ligaments of 75 ears. The points of origin and insertion of each of these ligaments, as defined by the authors, is summarized in Table 2.2. These ligaments were referred to as “suspensory ligaments” by the authors; they also correspond to the suspensory ligaments defined by Gulya and Schuknecht (1995). Lemmerling *et al.* concluded that the malleolar and incudal ligaments are visible only 26% to 68% of the time, with the exception of the LML which was reported visible 95% of the time. They therefore suggested the possibility of ligament abnormality in case where a ligament is clearly visible.

	Sensitivity (average of 2 observers)	Point of origin	Point of insertion
AML	68%	malleus head	anterior epitympanic wall
SML	46%	malleus head	roof of middle-ear cavity
LML	95%	malleus neck	bony margin of tympanic notch
PIL (medial)	26%	incus short process	fossa incudis
PIL (lateral)	35%		

Table 2.2. Visibility of the “suspensory ligaments”, as reported by Lemmerling *et al.* (1997).

2.3 INNER EAR

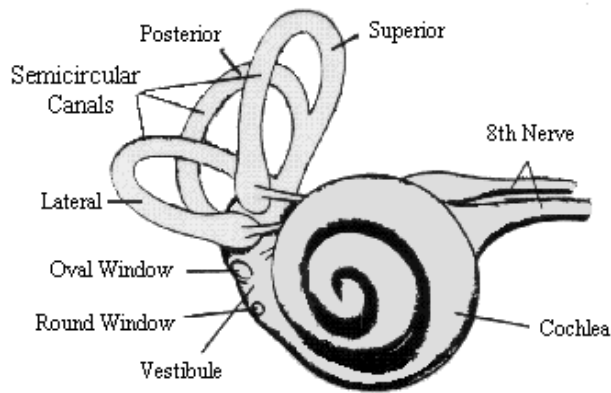


Figure 2.15 A schematic representation of the inner-ear components. The role of the inner ear is to transform the mechanical energy it receives from the middle ear into electrical energy, and send it to the brain via the 8th cranial nerve.

<http://www.bcm.tmc.edu/oto/studs/anat/tbone.html>

Unlike the other two ear compartments, the inner ear is liquid-filled. It converts mechanical energy into electrical impulses. It communicates with the middle ear via two openings – the oval window and round window. Its main components are the vestibule, cochlea and semicircular canals, seen in Figure 2.15. The vestibule, located medial to the oval window, is responsible for balance. Anterior to it is the cochlea, a snail-shaped organ responsible for receiving and converting sound waves into neural impulses. Posterior to the vestibule are the three semicircular canals, oriented at right angles with respect to one another, which detect angular acceleration¹.

Communication with the middle ear is established when the stapes footplate vibrates in and out of the oval window, and displaces the cochlear liquid. To reduce the cochlear pressure created by the inward motion of the footplate, the round window moves in and out of the cochlea, in opposite phase with the oval window. These two vibrations cause the cochlear liquid to vibrate and depolarize the auditory hair cells, thereby sending signals via the 8th cranial nerve to the brain (Fowler, 1948).

¹ <http://www.bcm.tmc.edu/oto/studs/anat/tbone.html>

Table 2.1 Structures, ligaments and joints of the middle ear as viewed by numerous authors. (Page numbers in **boldface** indicate illustrations).

	Gulya & Schuknecht, 1995	Palva, 2001 (often used 'fold' and 'ligament' interchangeably)	FCAT, 1998	Silverstein, 1972	Wolff <i>et al.</i> , 1957 ²	Proctor, 1989
MALLEUS						
<i>Anterior malleal ligament (AML)</i>	- holds anterior process to petrotympanic fissure (pp. 51, 52, 58)	- Yes (pp.5, 12, 12) - anterior malleal ligamental fold (fig 8, p.13)	-Yes, and anterior malleal fold	- Yes, and anterior malleal fold (p. 16)	NO	Yes
<i>Anterior suspensory ligament (ASL)</i>	- superior to AML; head to ant wall of epitympanum (pp. 52, 56, 57, 74)	- limits lateral malleal space anteriorly (pp.12, 52, 57, 74)	NO	NO	NO	NO
<i>Lateral malleal ligament (LML)</i>	- not mentioned in index, but appears in fig 1.26, p. 17 (extends laterally from the neck)	- a.k.a. external malleal ligament (pp. 5, 6, 9, 12) - its weaker bundles: from neck to opposite lateral attic wall, forming anterior ½ of lateral malleal space's floor (p.15) - strong bundles: from malleus to anterior tympanic spine; form anterior portion of roof of Prussak's space (p. 16) - lateral malleal ligamental fold (p. 13) strong; forms larger	Yes	Yes (p. 16)	- neck to posterior tympanic spine; for anchorage; (pp. 160, 161, 288, 289) - above neck, enclosed by horizontal fold of mucosa; to edge of Rivinian notch (pp.158-60)	Yes (p. 75) - lateral malleal fold: fans out between malleus neck and bony rim of notch of Rivinus (pp. 74, 75)

² A newer edition of this book exists (1971), but has not been checked yet.

		portion of floor of lateral malleal space = roof of Prussak's space				
<i>Lateral suspensory ligament (LSL)</i>	- neck to bony margin of Rivinus (or tympanic notch)(pp. 56, 57, 73)	NO	NO	NO	NO	NO
<i>Posterior malleal ligament (PML)</i>	- thick portion of posterior malleal fold; from neck to pretympanic spine (pp.57, 58, 174)	- strong bundle of fanlike fibers; run from neck to post tympanic spine (p.5) -fold: pp.12,13 (fig 8)	NO - posterior malleal fold	NO - posterior malleal fold (p. 16)	NO	Fold (fig 97, p.72)
<i>Superior malleal ligament (SML)</i>	NO	- just mentioned, no details (pp. 28, 38) - fold located anterior to SML but usually absent, (pp. 31, 38)	Yes	NO	- union of 2 mucosal layers enveloping epitymp; suspend'd fr bony trabecula of roof (tegmen) of epitymp (pp. 288, 289)	Yes (fig 101 p.74) + -fold (fig 98, p.72)
<i>Superior suspensory ligament (SSL)</i>	- betw head & tegmen of epitympanum (p. 57)	NO	NO	NO	NO	NO
INC-MALL JOINT	- lateral & medial (thickened portion of capsule) (pp. 71, 73, 74)	-	- Yes (no mention of lateral and medial ligaments)	- Yes (no mention of lateral and medial ligaments)	-fibers of capsule extend superiorly over malleus (pp. 6-9)	Yes

INCUS						
<i>Posterior incudal ligament (PIL)</i>	Yes (pp. 64, 52, 66, 68)	-Yes (pp. 28, 30, 39) -posterior incudal ligament fold: pp. 8, 30	Yes	-body to incudal fossa (p. 18)	-2 bundles (elastic fibers) (pp. 16, 17, 42, 84, 85, 133, 137)	Yes
<i>Superior incudal ligament (SIL)</i>	NO	NO	Yes	NO	NO	-point of attachment to incus shown in figure III-38 (p. 243); no other details

CHAPTER 3

MECHANICS OF THE MIDDLE-EAR

3.1 TRANSFORMER MECHANISM

The middle ear behaves as a coupling element between the sound waves of the air-filled outer ear and the liquid of the inner ear. Due to its density and elasticity, the acoustic impedance of air is approximately 347 times smaller than that of water. As a result, a direct coupling between two such media would result in poor energy transmission, hence the need for an impedance-matching transformer between them.

Acoustic impedance, Z , is defined as:

$$Z = \frac{P}{U} \quad (3.1)$$

where P is the sound pressure and U is the volume velocity (velocity times area). For the case of the middle ear, the pressure at the stapes is increased while its volume velocity is decreased.

The classical concept of the middle-ear transformer is based on the **surface-area** mechanism, the **ossicular-lever** mechanism, and the **curved-membrane** mechanism.

The **surface area** of the TM is greater than that of the footplate. Assuming tight coupling between the two structures, this difference will contribute to an increase in pressure at the footplate that is proportional to the ratio of the effective areas of the TM and footplate. Since these areas have been taken to be approximately 55 mm^2 and 3.2 mm^2 at the TM and stapes (Wever and Lawrence, 1954), respectively, the pressure would be increased by a factor of approximately 17. This factor, however, is valid only for the once-assumed TM movement about a fixed hinge, as well as piston-like stapes behaviour (Békésy, 1941). Since then, numerous studies have reported more complex behaviour patterns for both the TM (Khanna & Tonndorf, 1972) and the stapes (Decraemer *et al.*, 2000).

The **ossicular-lever** mechanism assumes a common axis of rotation for the ossicles which runs from the anterior process of the malleus to the posterior incudal ligament. The difference in length between the manubrium of the malleus and the long process of the incus relative to this axis has been supposed to result in a lever action and, in turn, pressure amplification at the stapes footplate. More details on this mechanism can be found in the works of Békésy (1941) and Wever and Lawrence (1954).

The **curved-membrane** effect was first proposed by Helmholtz in 1869, and later supported by Khanna and Tonndorf (1972). The mechanism is based on the curvature of the eardrum and the special arrangement of its fibres, which are believed to amplify the incoming sound pressure before it hits the manubrium. Funnell (1996) reported, based on simulations, that because of the curvature “certain regions of the eardrum are more effective in driving the manubrium than can be explained on the basis of their distance from the axis of rotation”. This behaviour was found not to require the tension and anisotropy that were assumed by Helmholtz.

These three proposed mechanisms are all simplistic and cannot really be cleanly separated.

3.2 EXPERIMENTAL OBSERVATIONS

3.2.1 Tympanic Membrane

TM displacement was first qualitatively described by Mach and Kessel (1874), using a magnifying lens. Perhaps the best TM vibrations measurements are those of Tonndorf and Khanna (1972) and Khanna and Decraemer (1996). They reported displacement maxima in the posterior and anterior regions at low frequencies and complex vibration patterns over the TM at frequencies greater than 2.5 kHz. TM displacements in the region which runs along the manubrium were smaller and smoother than those seen elsewhere on the TM (Tonndorf and Khanna, 1972; Funnell *et al.*, 1987).

Phase-shift moiré topography, by Dirckx and Decraemer (1991), revealed an extra complication in the TM displacement pattern where it connects to the manubrium. This

region lies between points 1 and 3 in Figure 3.1. Rigid-body movement was seen in the lower 3/5th portion of the manubrium, but inward membrane bending was seen in the upper 2/5th portion. These results are consistent with the previously discussed (Section 2.2.8.1) microscopic observations of Graham *et al.* (1978), suggesting weaker coupling between the TM and malleus in that region.

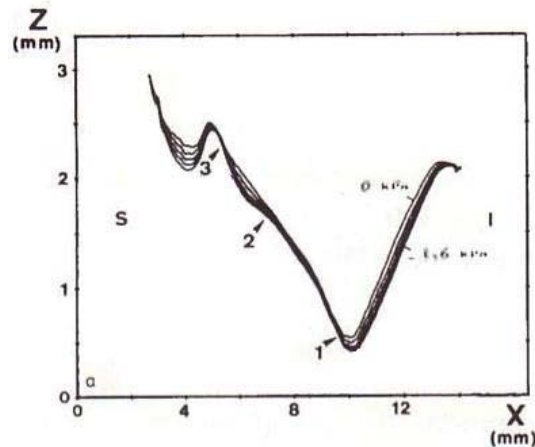


Figure 3.1 Cross-sections of the TM taken along the manubrium for positive middle-ear pressures between 0 and 1.6 kPa. The region between points 1 and 2 (the lower 3/5th portion of the manubrium) represents rigid-body movement, while that between points 2 and 3 (the upper two fifths of the manubrium) shows inward bending due to a weaker TM- malleus attachment in that region (Dirckx and Decraemer, 1991).

3.2.2 Ossicular Chain

The classical concept of ossicular-chain displacement portrayed rotation of the malleus and incus about a fixed imaginary axis which ran through the anterior process of the malleus and the posterior incudal ligament (Dahmann, 1929; Békésy, 1960). Gundersen *et al.* (1976) and others showed, however, that the location of the axis varied with frequency. Huber *et al.* (1996), for example, observed, using laser Doppler vibrometry on human temporal bones, that this axis moved slightly superiorly with increasing frequencies above 1 kHz (Figure 3.2). Furthermore, Khanna and Decraemer (1996) and Huber *et al.* (1996) observed a dominant rotational component in malleus displacement at

low frequencies, but more complex ossicular behaviour at higher frequencies; this behaviour consists of both translational and rotational components.

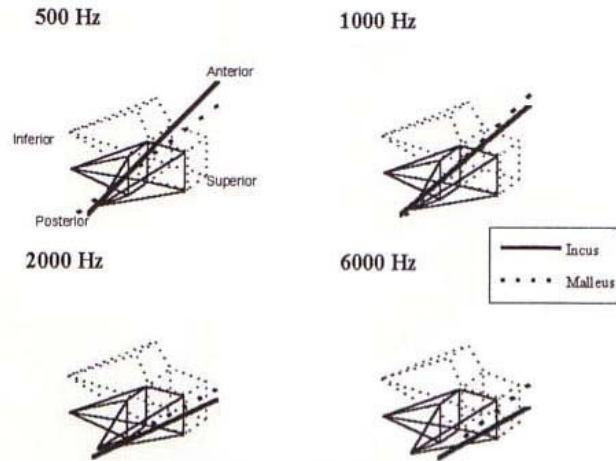


Figure 3.2 The rotational axis of the malleus and incus shifts superiorly with increasing frequencies beyond 1 kHz (Huber *et al.*, 1996). The initial positions of the simplified malleus-incus model and its axis of rotation are represented by thin and thick solid lines, respectively, while their final positions (when vibrating) are represented by thin and thick dotted lines, respectively.

The incudomalleolar joint is often considered to be rigid for acoustical transmission (Huttenbrink *et al.*, 1986; Gundersen *et al.*, 1976). Some researchers, however, have reported slippage, or relative motion, between the malleus and incus at frequencies greater than 1 kHz (e.g., Guinan *et al.*, 1966; Huber *et al.*, 1996).

The incudostapedial joint, on the other hand, is a non-rigid joint (Guinan and Peake, 1967). A modelling study has shown significant bending of the bony pedicle between the long process and lenticular process of the incus (Siah, 2002; Funnell *et al.*, in press). This indicates that at least some of the flexibility in that region may be attributable to the pedicle rather than to the joint itself.

Because of the footplate's important role in transmitting mechanical energy to the inner ear, its movement has been closely studied. Early studies by Guinan and Peake (1967) reported piston-like footplate motion at low frequencies. Recent studies have shown more complex motion – a combination of piston-like and rocking motion – at frequencies beyond 1 kHz (Khanna and Tonndorf, 1972; Heiland *et al.*, 1999; Huber *et al.*, 2001).

3.2.3 Samples of Experimental Measurements

Table 3.1 provides a sample of the many experimental vibration measurements taken from human temporal bone (TB) and live subjects over the years. It summarizes the works of Gyo *et al.* (1987), Nishihara and Goode (1996), Kempe *et al.* (1996), Huber *et al.* (2001) and Bance (from Dalhousie University).

These five reports use different age groups and cavity statuses, however, making inter-group comparisons difficult. The comparisons are also restricted by the differences in the points at which the measurements were recorded. We also noticed contradictions among the researchers' observations. For example, when comparing live and TB umbo vibrations, Nishihara and Goode (1996) reported smaller live middle-ear measurements at low frequencies (88.4 nm vs. 123.7 nm zero-to-peak), while both Kempe *et al.* (1996) and Huber *et al.* (2001) reported the opposite (39.3nm vs. 13.7 nm zero-to-peak, and a 10 dB difference, respectively). Another significant problem is the ambiguity in whether the measurements represent peak-to-peak (p-p), zero-to-peak (0-p), or root mean square (rms) values. The majority of the authors also mentioned significant inter- and intra-ear variability, in particular at low frequencies. Kempe *et al.*, 1996, for example, reported a difference of 8.5 dB for intra-ear measurements at 0.3 kHz and irreproducible results at this frequency. They also reported a difference of 5.7 dB for inter-ear measurements at frequencies higher than 3 kHz, but did not use enough subjects to be able to determine the statistical significance of this finding.

3.3 FINITE-ELEMENT MODELS

Finite-element models, or mathematical models, of the middle ear are capable of representing the geometry of the middle ear as well as simulating its mechanics. The fundamentals of the finite-element method will be discussed in Chapter 4.

The first middle-ear finite-element models were for the cat. They include those by Funnell (1975), Funnell and Laszlo (1978), and Funnell *et al.* (1987). The first complete human model was introduced by Wada *et al.* (1992). More recent models are by Prendergast *et al.* (1999), Koike *et al.* (2002), Sun *et al.* (2002) and Gan *et al.* (2004). Their low-frequency results are summarized, along with those of Wada *et al.*, in Table 3.2. All of them include the ossicles, joints, ligaments, tendons, and cochlear load; the choice of ligaments, however, differs from one group to another. Prendergast *et al.* (1999) and Koike *et al.* (2002) also included the external auditory canal, and Gan *et al.* (2004) included the middle-ear air cavity. Partial models of the human ear have also been developed, including those by Lesser and Williams (1988) and Beer *et al.* (1996). These groups studied the human eardrum and malleus responses under static and dynamic loading, respectively. In addition, several groups (e.g., Eiber, 1996; Abel *et al.*, 1998; Kelly *et al.*, 2003) have incorporated various prosthesis designs into their middle-ear models; these prostheses, depending on their designs, may serve as total or partial ossicular replacements in cases of ossicular chain interruption.

As indicated in Table 3.2, there were several uncertainties in the data format (e.g., 0-p, p-p, or rms). In fact, only Sun *et al.* (2002) stated whether they were reporting 0-p, p-p or rms displacement values. We therefore attempted to deduce these data formats from the clearly stated formats of the experimental studies to which the modellers had compared their results.

As seen in the third entry of Table 3.2, this issue of reported units remains unclear. Koike *et al.* (2002) calculated umbo and stapes displacements at 80 dB SPL (0.2 Pa, rms value), without mentioning whether they were using 0-p, p-p or rms values. They then compared their model's displacements to those of Gyo *et al.* (1987) taken at 124 dB SPL (31.7 Pa,

rms value), Figure 3.3. They normalized Gyo's displacements to 80 dB SPL and plotted them in the same graph along with their own displacements (Figure 3.4). When we attempted to normalize Gyo's readings ourselves, we obtained 69.4 nm p-p (or 34.7 nm 0-p) and 24.4 nm p-p (or 12.2 nm 0-p) at the umbo and stapes, respectively, at 0.1 kHz. From Figure 3.4, however, we can see that Koike *et al.* reported these normalized displacements as 20 nm and 9 nm, respectively. These clearly do not correspond to either the peak-to-peak or the zero-to-peak values that we obtained. Therefore, the units used by this group remain unclear. Notice, however, that by normalizing Gyo's peak displacements to 1 Pa, we obtain 200.7 nm at the umbo, and 89.2 nm at the stapes (Table 3.1). Comparing these values to his normalized displacements, as reported by Koike *et al.*, we see that they differ by a factor of 10. Therefore, it is possible that Koike *et al.* were reporting displacements that were normalized to 0.1 Pa, and not to 80 dB SPL.

The normalized measurements that we report in the table are correct assuming that the remaining three groups have correctly interpreted the experimental displacements with which they compare their work.

In general, these five studies portrayed similar umbo displacements (28 to 35.4 nm 0-p), with the exception of the study by Wada *et al.* (1992). Wada's displacements (74.3 nm 0-p) differed from the others by a factor of approximately 2.5. Stapes displacements, on the other hand, showed more variability from group to group. The smallest and largest displacements were 23 nm 0-p (Prendergast *et al.*, 1999) and 70.7 nm 0-p (Sun *et al.*, 2002), differing by a factor of 3.1. These differences may just reflect differences in the experimental data used to fit the models.

We shall refer to this table again in Chapter 7, where we compare the responses of these published models to those of our own model.

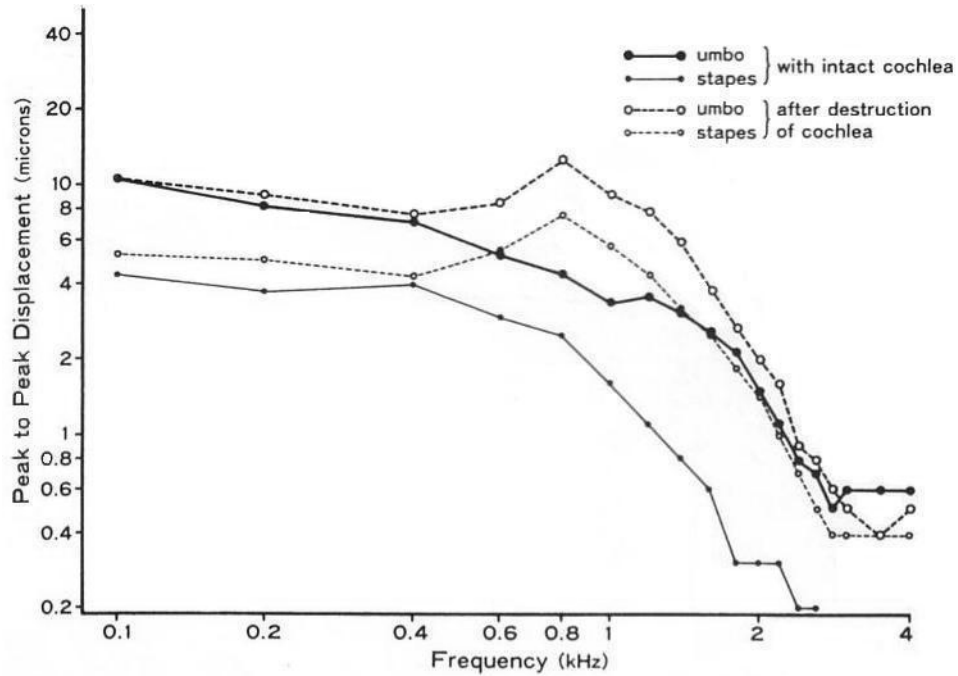


Figure 3.3 Umbo and stapes displacements measured by Gyo *et al.* (1987), at 124 dB SPL. The intact-cochlea displacements were normalized by Koike *et al.* (2002) to 80 dB SPL and compared to their corresponding model displacements. From Gyo *et al.* (1987).

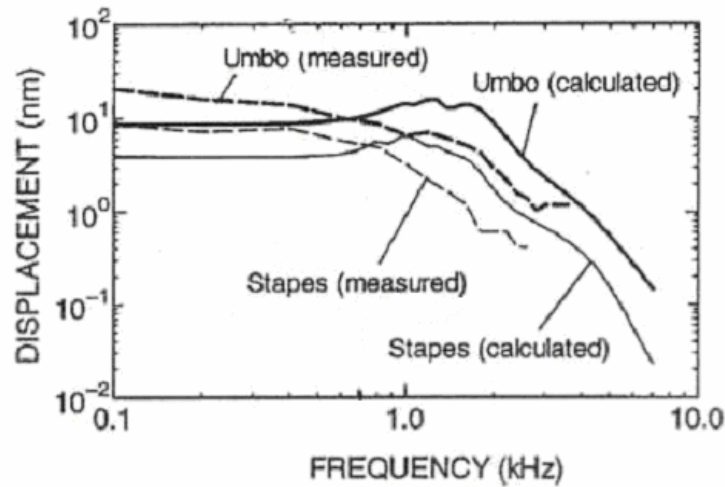


Figure 3.4 A comparison between calculated (Koike *et al.*, 2002) and measured (Gyo *et al.*, 1987) umbo and stapes displacements, at 80 dB SPL. The original measurements taken by Gyo *et al.* were at 124 dB SPL. From Koike *et al.* (2002).

Table 3.1 A review of several middle-ear experiments performed on human subjects and cadavers.

	Pressure & freq range	TM and/or stapes displacements	Ratios	Normalized Displacements (at 1Pa)	Comments
<p>Gyo et al. (1987)</p> <ul style="list-style-type: none"> ▪ video measuring system ▪ 14 TBs ▪ intact cochlea, sealed cavity 	124 dB SPL, 0.1 kHz	<ul style="list-style-type: none"> ▪ <i>umbo</i> displacement: 4500 nm 0-p ▪ <i>stapes</i> displacement: 2000 nm 0-p 	<p>$LR_{us}^1 = 2.3$ at $0.1 < f < 0.8$ kHz</p> <p>LR_{us} increased above 1.2 kHz and reached peak (~5.5) at upper frequency range limit (2.2 kHz)</p>	<p><i>umbo</i>: 200.7 nm 0-p</p> <p><i>stapes</i>: 89.2 nm 0-p</p>	<ul style="list-style-type: none"> ▪ LR_{us} larger than the accepted; may be due to “increased laxity of the suspensory ligaments and TM with age” ▪ one experiment on TB with cochlea removed: rotation decreased; piston-like umbo & stapes disp were similar to those with intact cochlea at $f < 400$ Hz, but greater at higher frequencies (e.g., 10 dB difference at 1 kHz)
<p>Nishihara & Goode (1996)</p> <ul style="list-style-type: none"> ▪ LDV² ▪ 99 human ears, 52 live subjects; avg age: 53; cavity closed ▪ 29 fresh TB’s (age and cavity conditions not provided) 	80 dB SPL, 0.2 kHz	<p><i>live umbo</i> displacements:</p> <ul style="list-style-type: none"> ▪ 64 normal ears: 12.5nm 0-p ▪ 35 pathologic ears: similar at low and mid-freq range <p><i>TB umbo</i> displacements:</p> <ul style="list-style-type: none"> ▪ 29 normal ears: 17.5 nm 0-p <p><i>∴ live measurements are stiffer than TB measurements</i></p>	N/A	<p><i>live umbo</i>: 88.4 nm 0-p</p> <p><i>TB umbo</i>: 123.7nm 0-p</p>	<ul style="list-style-type: none"> ▪ 10 μm p-p difference in live umbo displacements between two age groups (group A: 10 - 49 yrs, group B: 50 - 79 yrs) ▪ older subjects group: greater umbo displacements at $f < 3$ kHz

¹ LR_{us} = Lever ratio = umbo displacement : stapes head displacement

² LDV: laser Doppler vibrometry

<p>Kempe et al. (1996)</p> <ul style="list-style-type: none"> ▪ LDV ▪ used TB and live subjects (age and number not specified) ▪ open cavity 	<p>85 dB, 0.05 kHz</p>	<p><i>live umbo displacements:</i></p> <ul style="list-style-type: none"> ▪ 10 nm 0-p <p><i>TB umbo displacements:</i></p> <ul style="list-style-type: none"> ▪ 3.5 nm 0-p <p><i>∴ TB measurements are stiffer than live measurements</i></p>	<p>N/A</p>	<p><i>live umbo:</i> 39.3 nm 0-p</p> <p><i>TB umbo:</i> 13.7nm 0-p</p>	<ul style="list-style-type: none"> ▪ reproducible intra-ear measurements, except for at lowest freqs (e.g., difference of 8.5 dB at 0.3 kHz, 2.5 dB at 1 kHz, and 1.3 dB at 3 kHz) ▪ inter-ear variations are high (e.g., difference of 6 dB at 0.3 kHz, 3.1 dB at 1 kHz, and 5.7 dB at $f > 3$ kHz); not enough subjects to determine whether difference is statistically significant
<p>Huber et al. (2001)</p> <ul style="list-style-type: none"> ▪ LDV ▪ cavity open ▪ 7 live ears (3 – 69 yrs; avg age: 31) 	<p>80 dB SPL, 0.5 kHz</p>	<p><i>Stapes displacements:</i></p> <ul style="list-style-type: none"> ▪ $f < 1$ kHz: 1.5 to 2 nm peak <p><i>Compared mean TB and live stapes displacements:</i></p> <ul style="list-style-type: none"> ▪ $f < 1$ kHz: less than 10 dB difference <p><i>∴ TB measurements are stiffer</i></p>	<p>N/A</p>	<p><i>stapes:</i> 10.6nm 0-p</p>	<ul style="list-style-type: none"> ▪ no angle correction (laser beam 30° - 40° from normal to stapes footplate) ▪ cutting PIL had no significant effect on displacement (max difference = 2.9 dB) ▪ possibly overestimated low-freq response and underestimated high-freq response (by 1 – 3 dB)
<p>M. Bance (Dalhousie University)</p> <ul style="list-style-type: none"> ▪ LDV ▪ cavity open ▪ intact inner ear ▪ 77-yr-old male 	<p>80 dB SPL, 0.5 kHz</p>	<p><i>PT:</i> 140.6 nm 0-p <i>umbo:</i> 57.4 nm 0-p <i>stapes:</i> 29.0 nm 0-p</p>			<ul style="list-style-type: none"> ▪ displacements compared to those of our model

Table 3.2 A summary of several finite-element models of the human middle ear. Groups reported TM, umbo, and stapes displacements (in nanometers, nm) at either 80 (0.2 Pa, rms value) or 90 dB SPL (0.632 Pa, rms value). The displacements were then normalized to 94 dB SPL (or 1 Pa) for comparison purposes, assuming linearity of middle-ear vibration.

	INPUT	OUTPUT					
	PRESSURE & FREQUENCY	REPORTED DISPLACEMENT			NORMALIZED DISPLACEMENTS (nm/Pa)		
		TM	umbo	stapes	TM	umbo	stapes
Gan <i>et al.</i> (2004)	90 dB SPL, 0.2 kHz	100 nm p-p	-	30 nm p-p	111.9 nm 0-p	-	33.6 nm 0-p
Sun <i>et al.</i> (2002)	80 dB SPL, 0.25 kHz	-	8 nm p-p	18 nm p-p	-	28.3 nm 0-p	70.7 nm 0-p
		- displacements not flat at lowest frequencies					
Koike <i>et al.</i> ³ (2002)	80 dB SPL, 0.1 Hz	28 nm in inferior & anterior regions	4 nm	-	198 nm	61.5 nm	-
Prendergast <i>et al.</i> ⁴ (1999)	80 dB SPL, 0.1 kHz	-	10 nm p-p	6.5 nm p-p		35.4 nm 0-p	23 nm 0-p
Wada <i>et al.</i> ⁵ (1992) (displ's from Huber <i>et al.</i> , (2003) who used this model).	80 dB SPL, 0.1 kHz		21 nm p-p	10 nm p-p		74.3 nm 0-p	35.4 nm 0-p

³Did not specify whether displacement were 0-p, p-p or rms, but they compared their results to those of Gyo *et al.* (1987). When we converted Gyo's values from his article to the values that they claim Gyo got, they do not match.

⁴ Did not specify whether displacement were 0-p, p-p or rms, but we assumed that they are p-p displacements because they are plotted in same graph with experimental p-p measurements of Nishihara & Goode (1996) & Kempe *et al.* (1996).

⁵ Did not specify whether displacement were 0-p, p-p or rms, but we assumed that they are p-p displacements because they are plotted in same graph with experimental p-p measurements of Gyo *et al.*, (1987).

CHAPTER 4

THE FINITE-ELEMENT METHOD

4.1 INTRODUCTION

The finite-element method is a powerful numerical method that has been applied in many fields, including structural analysis, to yield an approximate solution to partial differential equations. A structure, or continuum, is divided into a finite number of substructures, and their individual mechanical responses are evaluated. Each of these substructures, or elements, is defined by a set of functions. Common nodes from different elements have identical nodal displacements. Analysis of each element's behaviour produces an element stiffness matrix and an element load vector. Once all the elements are analyzed, the results are combined to form a structure matrix equation, or set of equilibrium equations. Boundary conditions are then applied and the unknown nodal displacements are calculated; intra-element displacements can also be found, using interpolation.

The finite-element software used here is SAP IV, developed by Bathe et al. (1973). This software calculates the static or dynamic response of a linear system. It is written in Fortran and runs under Unix, Linux, Windows 95/98/NT and later versions.

Numerous methods have been adopted for deriving the equilibrium equations, the most common of which are the variational method (e.g., Bath, 1982; Gallagher, 1975) and the weighted-residual method (e.g., Gallagher, 1975; Becker, 2004).

With increases in computer speed and memory, the finite-element method today can handle complex problems in static and dynamic analysis of structures, heat transfer, fluid flow, electromagnetics, seismic response, etc. The focus of this chapter will be on its application to static structural analysis.

The next section will provide a brief history of this method. Section 4.3 will discuss the finite-element mesh, including mesh resolution and element types. Section 4.4 will then

provide the mechanics fundamentals and will be followed by Section 4.5 on the variational method.

4.2 HISTORY OF THE FINITE-ELEMENT METHOD

The term *finite element* was not mentioned until 1960 (Clough, 1960); however, progress towards the finite-element approach started much earlier. This history is based entirely on the summaries provided by Gallaher (1975) and Hutton (2004).

Initial attempts at framework analysis took place between 1850 and 1875; these later proved to be the foundations for matrix structural analysis. The next 45 years showed little development toward finite-element analysis, mainly due to the difficulty in solving equations with large numbers of unknowns. Later, around 1920, basic ideas on truss and framework analysis started forming (Maney, 1915; Ostenfeld, 1926). Shortly thereafter, they were complemented by Cross's (1932) moment-distribution studies, which enabled the analysis of more complex problems.

Early approximation methods for solving differential equations were introduced by Lord Rayleigh (1870), Ritz (1909) and Galerkin (1915). Although they serve as a basis for the finite-element method, the interpolation functions used in the solution process were taken to be continuous over the entire domain, rendering these methods applicable only to special cases. A more general method, introduced by Courant in 1943, triggered the start of the finite-element approach. It, unlike the previous methods, permits the use of piecewise-continuous functions.

With the development of aircraft engineering in the late 1940's, and thus the analysis of more complex structures, new methods were introduced. Among these was the displacement method, which given the applied system forces determines the corresponding system displacements. Examples of 'displacements' include physical displacement, temperature and fluid velocity.

Additional extensions of the finite-element method in the 1960's and 1970's rendered it applicable to plate and shell bending, to general three-dimensional problems in elastic

structural analysis, and to fluid flow and heat transfer. Numerous finite-element programs were developed over the years, including NASTRAN during the 1960's, and more recent ones such as ANSYS, ALGOR, and COSMOS/M. More details on the history of this approach can be found in finite-element books (e.g., Zienkiewicz, 1970; Noor, 1991).

4.3 FINITE-ELEMENT MESH

To solve for the unknown nodal displacements of a large structure, it is broken down into smaller structures, or elements. These elements are connected to one another at their vertices, or nodes. The process of dividing the structure is also known as mesh generation. Element shape and size may vary within a structure.

4.3.1 Choosing the Mesh Resolution

Selecting the resolution, or fineness, of the mesh involves a trade-off between computation time and accuracy. Generally, fine meshes yield more accurate results than coarse meshes, but they also demand more computer resources in terms of memory and computation time. Therefore, the chosen mesh is often the coarsest mesh whose displacements are still acceptable, i.e., 'close enough' to the exact values. Additional details on the mesh-selection procedure will be provided in Chapter 6.

4.3.2 Element Types

Figure 4.1 represents some of the most common element types that have been developed over the years for representing structures. They range from the simple framework elements to the basic thin-plate elements or the more complex solid elements (Gallagher, 1975). In this thesis, thin-shell elements and boundary (spring) elements will be used.

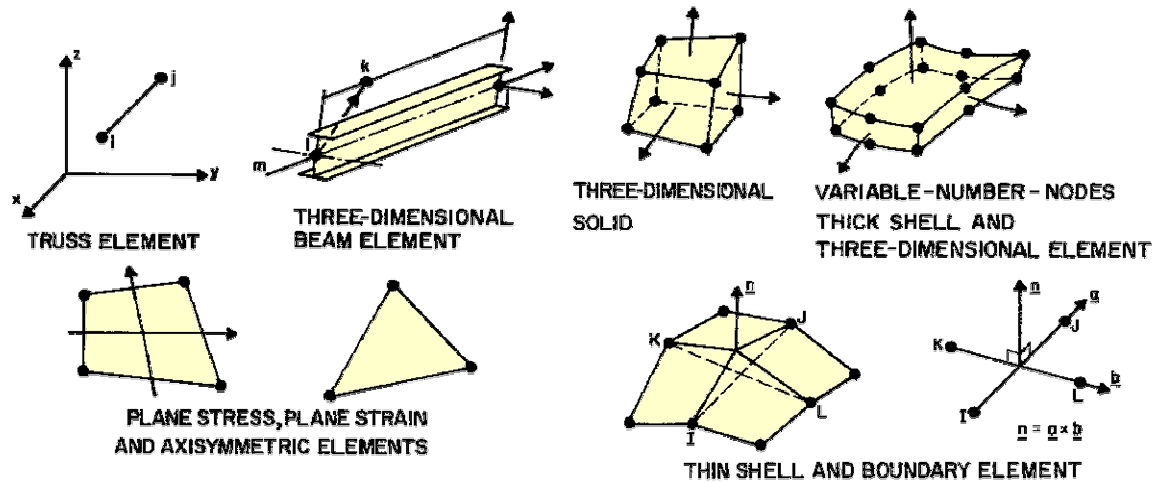


Figure 4.1 Types of elements that can constitute a mesh.

<http://audilab.bmed.mcgill.ca/~funnell/AudiLab/teach/fem/fem.html>

4.4 MECHANICS FUNDAMENTALS

This section will discuss the basic mechanics fundamentals that are needed for comprehending the finite-element procedure. For simplicity, the remaining part of this chapter will be limited to two dimensions. Scalars will be designated by non-bold letters, column vectors will be designated by bold letters between braces, and matrices will be designated by bold upper-case letters between square brackets.

4.4.1 Nodal Degrees of Freedom

The unknown variables of an element are the displacements of its nodes, also known as the nodal degrees of freedom, or d.o.f.'s. These nodal displacements in 3-D elements can be divided into a maximum of three translational and three rotational components.

For simplicity, let us consider a 2-D mesh of triangular elements that have two d.o.f.'s per node. The element nodal d.o.f. vector is defined by

$$\{d\} = [u_1 \ v_1 \ u_2 \ v_2 \ u_3 \ v_3]^T \quad (4.1)$$

where u_i and v_i correspond to the components of displacement of node i along the x and y axes, respectively. Similarly, the structure nodal d.o.f. vector can be represented by

$$\{\mathbf{D}\} = [u_1 \ v_1 \ u_2 \ v_2 \ \dots \ u_n \ v_n]^T \quad (4.2)$$

where n is the number of nodes that constitute the entire structure's mesh. Note that the element and structure coordinate systems are different.

One can calculate intra-element displacements, $\{\mathbf{s}(x,y)\}$, as

$$\{\mathbf{s}(x,y)\}_i = [\mathbf{N}] \{\mathbf{d}\}_i \quad (4.3)$$

where $[\mathbf{N}]$ and i correspond to the matrix of displacement interpolation functions and the element number, respectively. The interpolation functions describe the variation of displacement within each element.

4.4.2 Strains and Stresses in 2-D Problems

By definition, *strain* is a dimensionless variable that is proportional to the change in length. For the case of 2-D elasticity problems, the strain vector is

$$\{\boldsymbol{\epsilon}\}^T = [\epsilon_x \ \epsilon_y \ \gamma_{xy}] \quad (4.4)$$

where ϵ_x and ϵ_y are the normal strain components, and γ_{xy} is the shear strain component.

The strains within element i , represented by the vector $\{\boldsymbol{\epsilon}(x,y)\}_i$, are defined by

$$\{\boldsymbol{\epsilon}(x,y)\}_i = [\partial] \{\mathbf{s}\}_i \quad (4.5)$$

where $[\partial]$ is the differential operator. Substituting equation 4.3 into equation 4.5 yields

$$\{\boldsymbol{\epsilon}\}_i = [\partial][\mathbf{N}] \{\mathbf{d}\}_i = [\mathbf{B}] \{\mathbf{d}\}_i \quad (4.6)$$

where $[B]$ is the strain-displacement matrix.

Stress represents force per unit area. In 2-D elasticity problems, it is represented by the vector

$$\{\boldsymbol{\sigma}\} = [\sigma_x \ \sigma_y \ \tau_{xy}]^T \quad (4.7)$$

where σ_x and σ_y are the normal stress components, and τ_{xy} is the shear stress component.

The relation between stresses and strains is defined by *Hooke's law* as

$$\{\boldsymbol{\sigma}\} = [C]\{\boldsymbol{\varepsilon}\} \quad (4.8)$$

where $[C]$ is the matrix of material stiffnesses. For an elastic, isotropic, homogeneous material in plane stress, it becomes

$$[C] = \frac{E}{1-\nu^2} \begin{bmatrix} 1 & \nu & 0 \\ \nu & 1 & 0 \\ 0 & 0 & (1-\nu)/2 \end{bmatrix} \quad (4.9)$$

where E is the material's Young's modulus and ν is its Poisson's ratio.

4.4.3 Young's Modulus

A material's Young's modulus of elasticity, also known as its elastic modulus, represents its stiffness (in N/m^2 , or Pa). Examples of stiffness values of commonly encountered materials are summarized in Table 4.1.

	Gold	Aluminum alloys	Bone	Wood	Human tendon	Rubber (small strain)
Young's Modulus (GPa)	78.5	68.9	10-20	0.2-20	1.25-1.75 (toe region)	0.0069

Table 4.1 The Young's modulus of commonly-encountered materials.

4.4.4 Poisson's Ratio

Poisson's ratio, ν , is a dimensionless ratio which compares the transverse contraction strain to the longitudinal extension strain.

$$\nu = \epsilon_{\text{trans}} / \epsilon_{\text{longitudinal}} \quad (4.10)$$

According to the theory of isotropic elasticity, this ratio falls within the range of -1 to 0.5 (Fung, 1965). Examples of this value for different materials are: re-entrant polymer foams -0.7, cork close to 0, lead 0.2, steel 0.25 to 0.30, aluminum 0.33, and rubber 0.5. Given that the Poisson's ratio of common material ranges from 0.3 to 0.5, a value of 0.3 has been assumed acceptable for middle-ear structures (Funnell and Laszlo, 1982) and has been found to have no significant effect on their behaviour (Funnell, 1975).

4.5 THE VARIATIONAL METHOD

The variational method, also known as the energy or Ritz-Raleigh method, is used to formulate the element stiffness matrix. This section provides a brief overview of the method, based on the work of Cook *et al.* (1989, pp.109-112). Similar discussions of this method have been presented by Greene *et al.*, (1969), Desai and Abel (1972), Gallagher (1975), Becker (2004), etc.

The variational method applies the principle of *stationary potential energy* (Π) to the system. Mathematically, this principle is represented by

$$d\Pi = \sum_{i=1}^n \frac{\partial \Pi}{\partial \mathbf{D}_i} d\mathbf{D}_i = 0 \quad (4.11)$$

where \mathbf{D}_i represents the d.o.f.'s of the i -th structural node. Since $d\mathbf{D}_i$ are independent and arbitrary, then equation 4.11 implies that

$$\frac{\partial \Pi}{\partial \mathbf{D}_i} = 0, i = 1, 2, 3, \dots, n \quad (4.12)$$

in order that $d\Pi = 0$.

For a linearly elastic body in static equilibrium, the potential energy of the system equals the sum of the strain energy, U , and the work potential of the loads, Ω ; that is,

$$\Pi = U + \Omega \quad (4.13)$$

where

$$U = \frac{1}{2} \int_V \{\boldsymbol{\varepsilon}\}^T \{\boldsymbol{\sigma}\} dV = \frac{1}{2} \int_V \{\boldsymbol{\varepsilon}\}^T [\mathbf{C}] \{\boldsymbol{\varepsilon}\} dV \quad (4.14)$$

and

$$\Omega = - \int_V \{\mathbf{s}\}^T \{\mathbf{F}\} dV - \int_S \{\mathbf{s}\}^T \{\boldsymbol{\Phi}\} dS - \{\mathbf{D}\}^T \{\mathbf{P}\} \quad (4.15)$$

$\{\mathbf{F}\}$, $\{\boldsymbol{\Phi}\}$, and $\{\mathbf{P}\}$ represent the body force vector, the surface traction vector, and the concentrated force vector, respectively. Note that \int_V and \int_S imply integration over the entire volume and surface of the structure, respectively.

Next, equations 4.6 and 4.3 are substituted into equations 4.14 and 4.15, respectively. After simplification, we can express strain energy by

$$U = \frac{1}{2} \int_V \{\mathbf{d}\}^T [\mathbf{B}]^T [\mathbf{C}] [\mathbf{B}] \{\mathbf{d}\} dV \quad (4.16)$$

and the work potential of the loads by

$$\Omega = -\int_V \{d\}^T \{N\}^T \{F\} dV - \int_S \{d\}^T \{N\}^T \{\Phi\} dS - \{D\}^T \{P\} \quad (4.17)$$

Therefore, the total potential energy of the entire system becomes

$$\Pi = \frac{1}{2} \sum_{i=1}^M \{d\}_i^T [k]_i \{d\}_i - \sum_{i=1}^M \{d\}_i^T \{r\}_i - \{D\}^T \{P\} \quad (4.18)$$

where

$$[k]_i = \int_{V_i} [B]^T [C] [B] dV \quad (4.19)$$

corresponds to the *stiffness matrix* of element i , and

$$\{r\}_i = \int_{V_i} \{N\}^T \{F\} dV + \int_{S_i} [N]^T \{\Phi\} dS \quad (4.20)$$

corresponds to its *load vector*; M is the number of elements that constitute the structure.

Therefore, we may rewrite equation (4.18) as

$$\Pi = \frac{1}{2} \{D\}^T [K] \{D\} - \{D\}^T \{R\} \quad (4.21)$$

where

$$[K] = \sum_{i=1}^M [k]_i \quad \text{and} \quad \{R\} = \{P\} + \sum_{i=1}^M \{r\}_i \quad (4.22)$$

represent the *system stiffness matrix* and the *system load vector*, respectively. Before the additions in equation (4.22), the matrices are expanded to $n \times n$ matrices, where n is the number of d.o.f.'s in the structure. This is done so that the multiplication $[K]\{D\}$ in equation (4.21) is defined.

Finally, to satisfy the principle of stationary potential energy (equation 4.12), we differentiate equation 4.21 with respect to the nodal degrees of freedom. This yields the following structure matrix equation

$$[K]\{D\} = \{R\} \quad (4.23)$$

One may now solve for the nodal degrees of freedom, while taking the boundary conditions into consideration.

CHAPTER 5

METHODS

This chapter will provide an overview of the techniques that were adopted in order to generate a middle-ear finite-element model. Section 5.1 discusses x-ray micro-computed tomography as well as the details of the particular data that we acquired. Section 5.2 briefly reviews the steps involved in preparing histological sections and the role such sections played in this project. Laser Doppler vibrometry is then introduced in Section 5.3, along with the setup details of one specific experiment. Section 5.4 discusses segmentation techniques in general, and then focuses on the snake algorithm and the segmentation software used here. Section 5.5 discusses the mesh-generation software used in our lab.

5.1 X-RAY MICRO-COMPUTED TOMOGRAPHY

5.1.1 Introduction

Computed Tomography (CT) imaging, also known as CAT (Computed Axial Tomography) scanning, was invented in 1972 by the British engineer Godfrey Hounsfield of EMI Laboratories, England. It is a non-destructive imaging technology which has served as the basis for several modalities, including x-ray CT, magnetic resonance imaging (MRI), and positron emission tomography (PET). The word “tomography” comes from the Greek words “tomos” meaning “slice” or “section”, and “graphe” meaning “drawing”. CT involves scanning a volume from different angles, and later reconstructing and viewing its details using a computer. This volume could be a combination of soft tissue, bone, and blood vessels. Of all the modalities, only x-ray CT will be discussed here since it is the one used for our work.

X-ray CT scanners make use of x-ray technology and a computer, to scan a volume and then reconstruct it, respectively. They are capable of imaging internal structures, as well as distinguishing between thin bone and air spaces, like those found in the temporal bone (e.g., Som and Curtin, 1996). Since their invention 31 years ago, x-ray CT scanners have

undergone great development in their design and technology, thereby permitting the diagnosis of a wide array of injuries and illnesses, including those of the middle ear (e.g., Swartz 1983; Swartz *et al.*, 1983a,b; Fuse *et al.*, 1992). The different designs include conical, axial and spiral (or helical) scanners.

The x-ray CT machine passes an x-ray beam through the object to be scanned. As depicted in Figure 5.1, the object is located between an x-ray source and several detectors. The designs vary slightly from one scanner to another but in general the source emits a conical beam of x-rays towards an array of detectors. As these rays pass through the object, they are absorbed to different degrees, due to the variation in composition of the structure. Therefore, when received by the detectors, they create a matrix, or array, of elements of different strengths (or attenuation coefficients). One x-ray beam creates one image. Therefore, object rotation of 180° is necessary in order to have data representing the volume of interest (Thompson, 1985). These data are then reconstructed to yield slices using one of the four available reconstruction algorithms – simple back projection, integral equations, Fourier transform, and series expansion (Hendee and Ritenour, 1992).

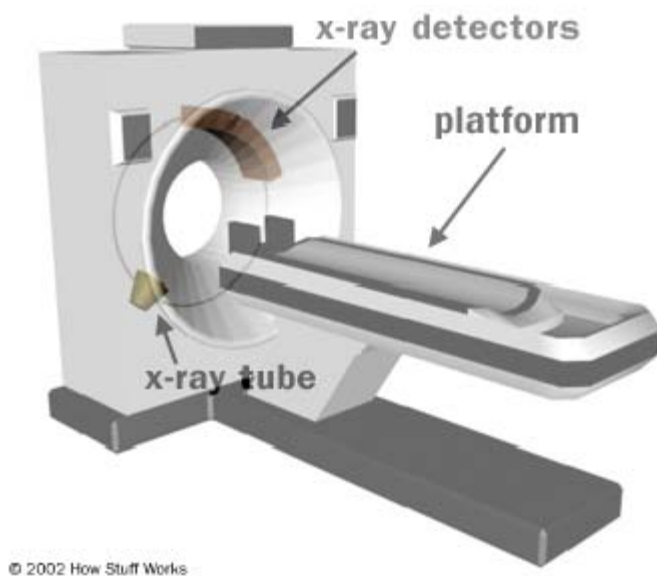


Figure 5.1 In scanners designed to image humans, the x-ray tube and detectors are mounted on a ring which rotates about the volume; however, in the smaller scanners designed to image small specimens, it is the object that rotates. From <http://science.howstuffworks.com/c-at-scan2.htm>.

For this project, we chose to use x-ray micro-computed tomography (x-ray micro-CT), a modality which images structures at the micrometer (μm) level (Flannery *et al.*, 1987). In

the SkyScan 1072 scanner that we used, a cone beam is emitted from the source to intercept the specimen mounted on a rotating stand. A 1024 x 1024 12-bit digital cooled charge-coupled detector (CCD) located on the other side of the specimen receives the attenuated x-ray beams. The pixel size of the created images can be chosen to be less than 1.8 μm , but the beam size and the resolution limit are 5 μm .

5.1.2 Micro-CT Data

We obtained high-resolution micro-CT data, using a SkyScan 1072 scanner, for creating a realistic 3-D model of a human ear. The scanned specimen was an ear of a 77-year-old male for which the middle-ear response had been measured by means of vibrometry (discussed in Section 5.3). This specimen, and the measurements, were made available by M. Bance at Dalhousie University, Halifax.

The sample was placed on a stand and rotated a total of 180°, in 0.9° steps. The data were then back projected, using the software Cone-Beam Reconstruction (found at <http://www.skyscan.be>), to give 1024 sections of 1024 by 1024 pixels each, and a voxel size of 19 μm . This was followed by downsampling, which yielded 512 sections of 512 by 512 pixels each, and a voxel size of 38 μm . A sample image can be seen in Figure 5.3.

5.2 HISTOLOGY

According to the Merriam-Webster dictionary, histology is “a branch of anatomy that deals with the minute structure of animal and plant tissues as discernible with the microscope”. To enable differentiation between the different types of tissues and to further study them, sample preparation is essential.

Preparing middle-ear sections for histology involves fixation, decalcification, embedding, sectioning, staining, and mounting. The tissue is first placed in a fixative solution, e.g., formalin, to preserve its proteins and prevent enzymatic and other post-mortem changes. Next, the sample is immersed in a decalcifying solution, such as formic acid, for several days. This removes the heavily concentrated calcium deposits in bone (or enamel) that may interfere with sectioning and lead to torn tissue. The sample is then

embedded in a sliceable material such as paraffin or plastic. This preserves the tissue's morphology for decades. Next, sections, as thin as one micron, can be cut using a microtome. They are then dried in a warm oven for 15 minutes so as to adhere to the microscopic slides on which they are being mounted. Before mounting the sections on the slides, the tissue is stained using one of numerous staining techniques, the choice of the technique depending on the tissue features of interest (e.g., Ham, Cormack, 1979).

Histological sections of various human ears (but not of the ear whose response was measured) were very helpful in creating the 3-D model of the middle ear. They aided in determining detailed ligament structure and points of insertion. These features were not clearly identifiable in the computed-tomography data due to the fineness of the ligaments and the artifacts in the images.

5.3 LASER DOPPLER VIBROMETRY

5.3.1 Introduction

Laser Doppler vibrometry is a non-contact optical measurement technique. It is based on the Doppler shift in frequency of coherent light reflected, or backscattered, from a moving object. Figure 5.2 shows the basic setup of a laser Doppler vibrometer (LDV).

A helium neon (HeNe) laser emits a beam of light that splits, at a beam splitter (BS1), into two beams – a reference beam and a measurement beam. The measurement beam passes through a second beam splitter (BS2) and hits the moving target at which the laser is aimed. This beam then reflects back and passes through a third beam splitter (BS3) where it mixes with the reference beam. The combined beam is directed towards a detector which determines the shift in frequency of the measurement beam. This shift, known as the Doppler shift, is caused by a change in the length of the path of the measurement beam, which occurs with target movement.

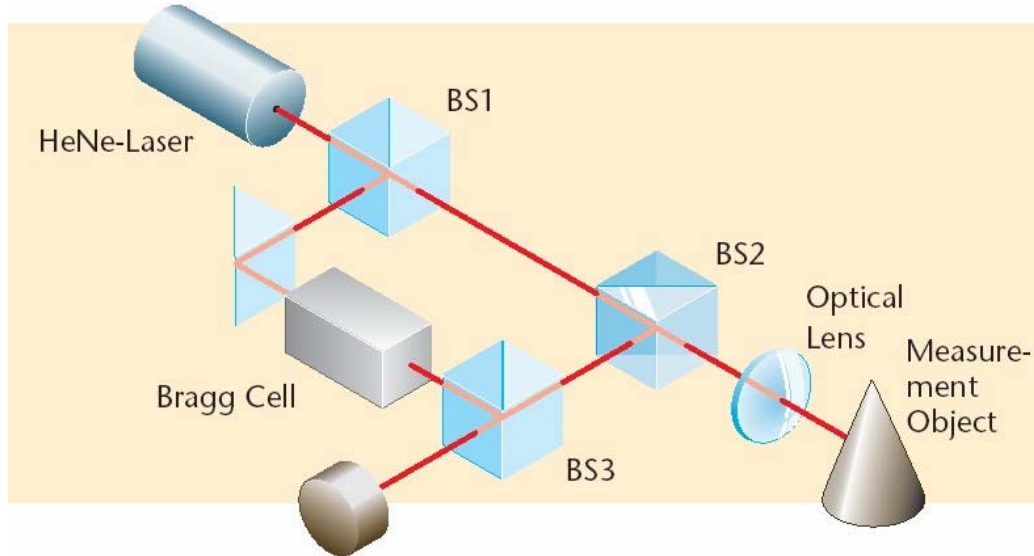


Figure 5.2 General setup of a laser Doppler vibrometer. It measures target velocity based on the shift in frequency of reference and measurement beams emitted from a helium neon laser (Polytec).

Via interpolation and digital demodulation, the vibrometer then determines object velocity. The displacement measurements can then be deduced, from velocity measurements, by integration. It is important, however, to treat velocity and displacement measurements differently; velocity sensitivity is an important determinant of LDV performance. Low-frequency performance has been reported as relatively poor (Hariharan, 2003; Polytec).

5.3.2 Vibrometry Measurements

Vibration measurements of the same middle-ear specimen as the one mentioned above (in Section 5.1.2) were made by M. Bance of Dalhousie University, Halifax. The middle-ear cavity was opened but the inner ear was intact. An ER2-earphone (Etymotic Research, Elk Grove Village, IL) placed about 1 cm from the eardrum delivered sound signals generated by a commercial package (Vibsoft®, Polytec PI, Tustin, CA). These signals consisted of frequency sweeps from 0.2 to 8 kHz at 90 dB SPL. The velocity was measured at six locations – three on the TM (posterior inferior, posterior superior, and umbo regions), and three on the stapes footplate (centre, posterior, and anterior regions).

At these locations, 0.5-mm² pieces of reflective tape were used as targets to increase reflectivity. The velocity readings were then converted into displacements. Since our study is limited to the low-frequency range, we only report Bance's averaged low-frequency measurements (250-300 Hz) for comparison with the displacements of our model.

5.4 SEGMENTATION

5.4.1 Introduction

Image segmentation is the process of identifying object boundaries in images. It is commonly used in computer vision and image analysis (e.g., Ayache, 1995; Stytz *et al.*, 1991). For our case, segmentation was used to identify middle-ear structures including the middle-ear ossicles, ligaments and muscles.

To segment the regions of interest, manual, semi-automatic and/or automatic segmentation can be used. Manual segmentation is tedious and irreproducible, and requires expert knowledge. Automatic segmentation, on the other hand, is faster, but usually needs to be checked and edited afterwards (Gibbon *et al.*, 1997). The safer option, and the one used in this project, is semi-automatic segmentation. It employs a specific algorithm to detect contour shape while permitting user supervision and guidance.

Over the years, numerous segmentation techniques have been proposed. Low-level techniques include thresholding, region growing, clustering and mathematical morphology. These methods are computationally fast and usually simple, but suffer from locality problems which may lead to loss of important information. High-level techniques include active contours (Kass *et al.*, 1986), discrete dynamic contours (Lobregt and Viergever, 1995), geometric deformable models (Miller, 1990) and geometric active contours (Caselles, 1995; Malladi *et al.*, 1995). Although computationally expensive, they offer better results than the low-level techniques, and are used extensively in numerous applications. These high-level techniques are all based on or equivalent to the same principle, that of active contours, or snakes, first introduced by Kass *et al.* (1986).

The contours behave as splines or curves that are driven towards object boundaries by minimizing an energy functional.

5.4.2 Snake Algorithm

The snake algorithm aims to converge a manually-segmented contour to the boundaries of the structure which the contour outlines. This contour consists of vertices that are joined by straight-line segments. By minimizing an energy functional, or cost function, for each of its vertices, it exhibits a dynamic behaviour and eventually converges to the structure's boundaries. This algorithm may fail, however, if the initial contour is too far from the structure's boundaries, as well as in regions with low boundary contrast or narrow cavities (Hatamzadeh-Tabrizi, 2003).

The cost function for each vertex of the discrete dynamic model involves a combination of internal, external and damping forces that are weighted by the user to obtain a desirable result. The internal forces (i.e., stretching and bending forces) come from the shape of the contour and serve to preserve its smoothness. For the case of discrete dynamic contours, this is accomplished by minimizing the local curvature at each vertex. The external forces are based on the image data and optional external constraints. Possible options for external forces include the gradient of the image, gradient vector flow (Xu and Prince, 1997) and pressure forces (Cohen, 1991). These forces attempt to drive the model towards the image's "landscape", or its strong features (Lobregt and Viergever, 1995). Damping force terms provide stability to the dynamic curve. They are of particular significance when there are two states with local energy minima and the model is oscillating between them (Lobregt & Viergever, 1995; Hatamzadeh-Tabrizi, 2003).

5.4.3 Fie

To segment the desired structures of the dataset, a home-grown programme named Fie was used. Fie, which stands for "Fabrication d'imagerie extraordinaire", has been evolving since 1989 to meet the demands of its users. This programme has been used for various image-analysis and related tasks (e.g., Herrera et al., 1991, 1997). It was

implemented in Fortran, and runs under GNU/Linux and Microsoft Windows 95 and later.

It can be downloaded from <http://audilab.bmed.mcgill.ca/~funnell/Audilab/sw/fie.html>.

As used here, it inputs an image file in TIFF, raw, or JPEG format and outputs a text file that is later used for mesh generation.

Several steps are taken to segment the structures. First, one of several colour-palette options is chosen, the most helpful of which was found to be the grey-level palette. It employs the concept of thresholding to aid in distinguishing between bone, soft tissue, and other. Two thresholds can be set: all grey-level values beneath the lower threshold are set to shades of blue, and all those beyond the upper one are set to shades of yellow. Once a rough sketch of a contour is drawn, either the snake algorithm or splines can be used to modify and resample its shape.

5.4.4 Segmentation Guidelines

The process of segmentation is complex and laborious. To keep track of all the contours, it is essential to name them systematically. In this work, we adopted the following style: The first part of the name is an abbreviation of the name of the structure which the contour represents; multiple contours representing the same structure have a number appended to their name. The final part of the name is the number of the slice in which the contour first appears.

Another convention used throughout the segmentation process is that all contours are segmented in the counter-clockwise direction. Therefore, the mesh elements' front faces face outward, while the back faces face inward. This convention is essential for correct model connectivity and error-free simulation results.

5.4.5 Open and Closed Contours

While segmenting the structures of interest, one has the choice between two types of contours – closed and open contours.

A closed contour is a contour that represents a closed region, which may or may not be connected to any other region in that slice. An example of a closed contour representing the incus (contour A) can be seen in Figure 5.3.

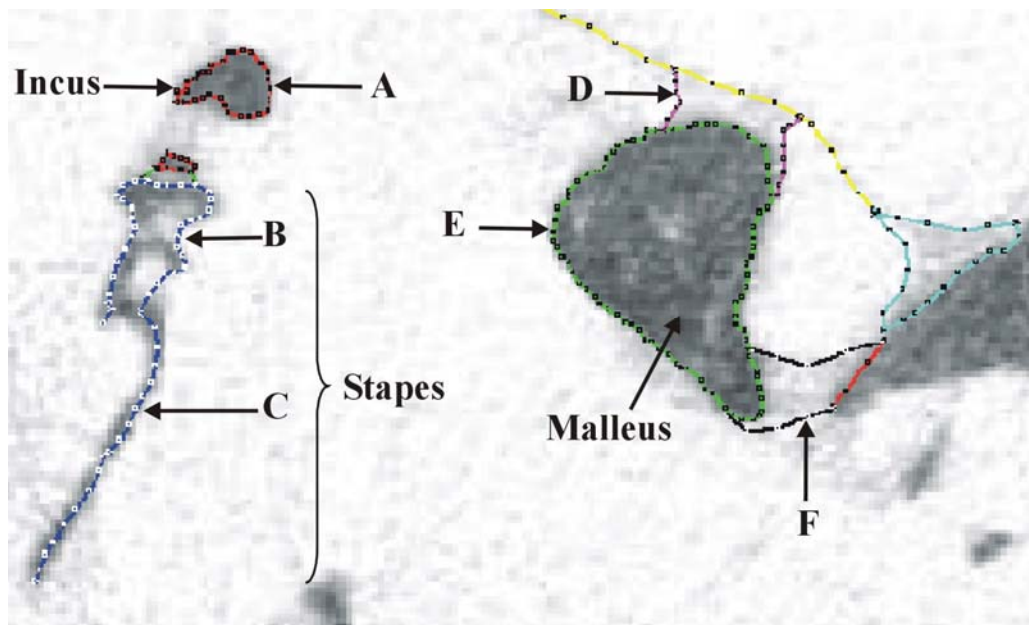


Figure 5.3 Examples of closed (contour A) and open (contours B – F) contours which were segmented in Fie to outline the regions of interest.

Contours in Fie are open by default (e.g., contours B to F in Figure 5.3). It is used for joining structures, such as ligaments and ossicles, or splitting structures when their anatomy changes in the consequent slices. Open contours can also represent thin structures, such as the TM, which are to be modeled as single layers. The advantage of this contour type is its ability to link complex structures, with the help of the connectivity options, thereby granting the user greater control over the structures.

5.4.6 Tr3 Text File

All the data related to the scanned volume and segmented contours are saved in a Tr3 text file. Its first part lists all the contour names, accompanied by their properties. These

properties include colour, connectivity, resolution, nodal boundary conditions, and material properties; all comments are preceded by semi-colons.

5.4.6.1 Contour attributes

Definitions of the possible contour attributes are provided in Appendix A.

The following is an example of a contour definition:

Example 1:

```
pars_tens1_193: -c 5;Salmon -xyr 20 -tr 0.5 -mat 1 -th 75.u -b CS -p 1. pars tensa
```

The contour ‘pars_tens1_193’ is a cyan (-c 5) open contour. It represents a portion of the pars tensa which first appears in slice 193. When viewed, the contour will be salmon in colour and will have a transparency of 0.5 (-tr 0.5). When triangulated, it will be subdivided with a resolution of 20 elements across the structure (-xyr 20). Since a z-resolution was not specified, every slice will be used in the triangulation. Its material type is set to 1 (-mat 1), and the thickness of its shell elements is 75 μm (-th 75.u¹). In addition, it is clamped at its first, or start, node. A pressure of 1 MPa (-p 1) is applied normal to the surface created by its shell elements.

5.4.6.2 Connecting contours

Connecting contours is essential for joining substructures and preserving structure continuity. This connection may be either between contours in the same slice, or between contours in different slices. An example of how connections are made across different slices is shown in Figure 5.4 and is further discussed in Section 5.5.

To link contours within the same slice, the start-at and finish-at attributes can be added to a contour’s definition as seen in example 2 below. The contours may connect at their first and/or last nodes to other contours’ first and/or last nodes.

¹ u is the symbol used for μ .

Example 2:

lig_incmall_lat167: -c 4;thistle -xyr 100 -mat 1 -th 50.u -s s mall_int_imlig167 -f s incus_167 incudo-malleal ligament

In this example, the contour 'lig_incmall_lat167' is a blue (-c 4) open contour. It represents the lateral side of the incudomalleal ligament. Mesh generation will yield a 50- μ m-thick structure (-th 50.u), of material type 1 (-mat 1), consisting of 100 elements across its diameter. This structure starts at the start node, or first node, of the contour 'mall_int_imlig167', and finishes at the start node of the contour 'incus_167'.

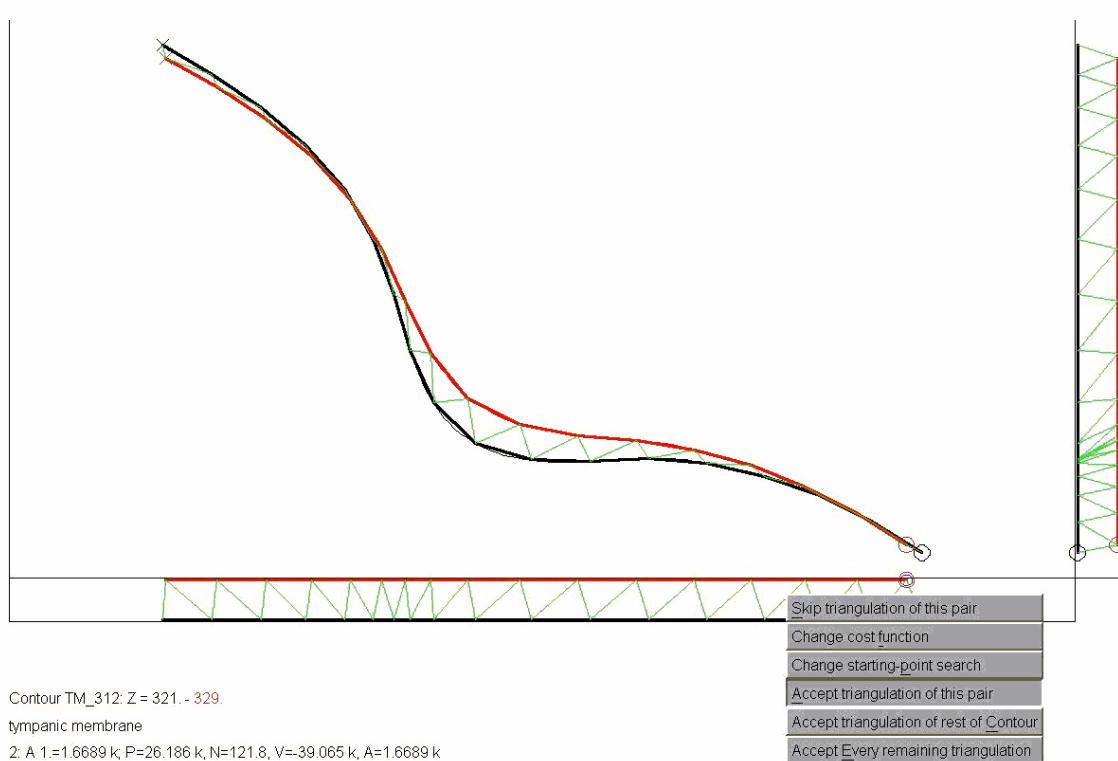


Figure 5.4 A screenshot from the mesh-generation software, Tr3, taken while joining two slices (slice 321 to slice 329) in which eardrum contour TM_312 appears.

Due to the scanned volume's complexity, contours representing the same structure may split from and join to others from one slice to another. This creates new contours with

different attributes, especially the start-at and/or finish-at attributes, hence the need for assigning different contour names. A separate section of the tr3 file, headed by the word “JOINS”, is used for specifying how contours with different names should be connected across slices.

Whether one is joining one contour to another, or multiple contours to one another, the concept is the same: the contours are connected by a 3-D surface created via triangulation. An example where multiple contours from multiple structures are being joined is illustrated in Figure 5.5.

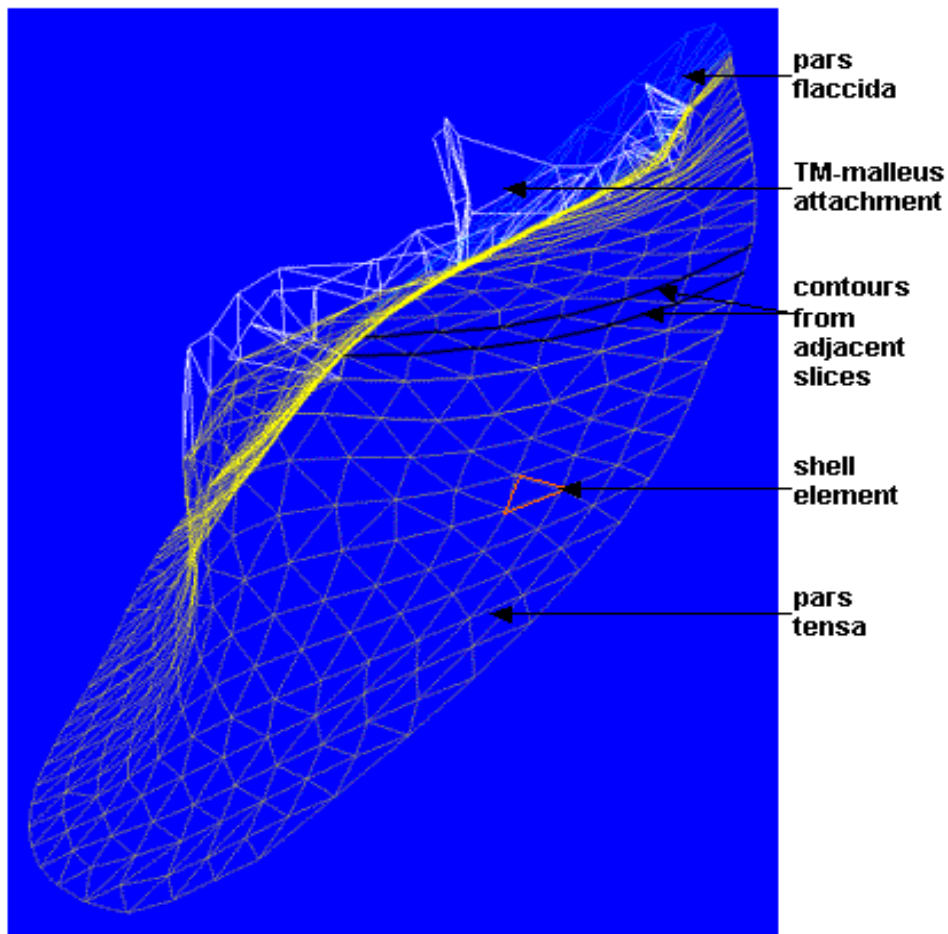


Figure 5.5 A mesh of the tympanic membrane and the TM-malleus attachment. It is made from joined contours of the pars tensa, pars flaccida, and TM-malleus attachment.

Example 3:

incus_170: inc_int_imlig170 incus_170 to inc_int_imlig195 incus_195 ;incus

The intention of the join named 'incus_170' is to join the last slice in which the contours 'inc_int_imlig170' and 'incus_170' appear to the first slice in which contours 'inc_int_imlig195' and 'incus_195' appear, keeping in mind the z-resolution of each.

The JOIN function may also serve to join only the first and/or last nodes of a contour to another contour. This is done by including the symbols '>' and '<', to denote the first and last nodes of a contour, respectively. This feature is mainly used to close gaps in the case of major changes in a structure's representation from one slice to the next.

Example 4:

malleus_jn1_241: malleus3_241> malleus3_241< to mall_ant_proc_242> ;malleus

The role of the malleus join named 'malleus_jn1_241' is to join the imaginary line whose endpoints are the first and last nodes of 'malleus3_241' to the first node of the contour 'mall_ant_proc_242'.

5.4.6.3 Closing openings at the ends of structures

Since triangulation joins contours in adjacent slices, the first multiple-point contour of a structure does not connect to anything in the previous slice, creating an undesired opening. Similarly, a multiple-point contour in the last slice of a structure does not connect to anything in the next slice, creating an undesired opening. To prevent such openings, one of two measures may be taken: either representing the last slice in which the structure appears by a single-point contour, or 'capping' the contour or contours.

The single-point contour is the easier option. It is done by assigning a one-node contour to represent the last slice in which the structure appears. This option produces a conical closing of the hole.

Capping a contour or contours, on the other hand, produces a flat closing. In the CAPS section, one can specify the open area to be triangulated. The area, which may be at either the first or last slice in which the contour or contours appear, is chosen by including the word HEAD or TAIL in the cap definition, respectively. A simple application of capping may be seen in the example below.

Example

inc_lentpl_234: TAIL inc_lentpl234 inc_int_isjt234 ;incus lenticular plate

The cap ‘inc_lentpl_234’ triangulates the open area created by the contours ‘inc_lentpl234’ and ‘inc_int_isjt234’. Since the contour names are preceded by the word ‘TAIL’, the cap will appear at the last slice in which the contours exist.

5.4.6.4 Subsets

Due to the potentially large number of substructures in a dataset, and the desire to create models of different combinations of substructures, with different resolutions or attributes, a SUBSETS section can be added to the Tr3 text file. By dividing the contours into subsets, only the desired subsets are triangulated for further model evaluation.

This section permits the modification of the contours’ attributes and is very useful in the case of experimenting with different contour resolutions.

5.4.6.5 Material properties

The MATERIALS section of the file consists of lines with the following syntax:

nmat ym pr den

The section lists all the material types of the dataset accompanied by their properties. *nmat* denotes the sequence number of the material type, *ym* denotes the Young’s modulus, *pr* denotes Poisson’s ratio, and *den* denotes the density of the material. The

units of these properties depend on the units used in the rest of the file. All materials are assumed to be linear and isotropic.

For our dataset, this section was defined as follows:

MATERIALS

1	20.M	0.3	1000.	;strong connective tissue (N/m ² , kg/m ³)- ligaments
2	200.M	0.3	1500.	;bone: malleus and incus
3	2.M	0.3	1000.	;strong connective tissue: stapedius muscle, tensor tympani muscle
4	200.M	0.3	1500.	;bone: stapes minus footplate
5	40.M	0.3	1000.	;strong connective tissue - pars tensa
6	200.M	0.3	1500.	;bone: medial side of stapes footplate
7	200.M	0.3	1500.	;bone: lateral side of stapes footplate
8	10.k	0.3	1000.	;stapedius annular ligament
9	50.M	0.3	1000.	;incudostapedial joint
10	200.M	0.3	1000.	;incudomalleolar joint
11	20.M	0.3	1000.	;pars flaccida
12	20.M	0.3	1000.	;superior malleal ligament (SML)
13	20.M	0.3	1000.	;anterior malleal ligament (AML)
14	20.M	0.3	1000.	;posterior incudal ligament (PIL)

END

The postprocessor, Fod, displays on the left side of the screen the range of displacements of each of the material types. Therefore, to easily observe these values, structures with the same materials properties were split into different material types. Examples of this display will be provided in Chapter 7.

5.4.6.6 Thickness

For the model of the TM, we needed to specify its thickness. The eardrum's thin membrane, however, was difficult to identify in the noisy micro-CT data. We therefore resorted to examining eardrums in histological atlases (Gulya and Schuknecht, 1995; Palva *et al.*, 2001) and directly in available histological sections of human middle ears;

and to reviewing observations from the middle-ear literature (Kirikae, 1960; Ladak and Funnell, 1995).

Solids are represented as hollow shells in the current version of Tr3 (see Section 5.5). The ‘thickness’ of each structure was established from direct measurement via the micro-CT slices. The slice that best resembled the average structure or shape was chosen. Next, the structure’s thickness (in that slice) was measured. Contours outlining that structure were then assigned a thickness equivalent to one third of the structure’s thickness. The cross-sections of the structure were represented by a single closed contour or by multiple open contours which were attached to one another to form a closed contour. In sections in which a structure became much narrower, different contour names were assigned and a different thickness value was used. This was the method used for all the bones, ligaments, muscles and tendons of the middle ear. It is acceptable for bones at the low frequencies we use to test our model because bones at these frequencies behave as rigid structures.

The thicknesses we assigned to the middle-ear structures are reported in Chapter 6.

5.5 MESH GENERATION

To perform finite-element analysis on a structure, a mesh representation of the structure is needed. Numerous methods have been adopted over the years for the purpose of mesh generation.

For this thesis, the home-grown Tr3 programme, under development in our lab since 1982, was used for mesh generation. This programme, given the plain-text (.tr3) model-definition file produced by Fie, triangulates 3-D surfaces between contours in adjacent slices of a dataset (Funnell, 1984a,b). It outputs two main files: a .wrl file and a .sap file. The .wrl file is a VRML model file which allows interactive visualization of the model (<http://www.web3d.org/x3d/vrml/>). The .sap file includes all the information about the mesh’s nodes and elements – such as their coordinates, boundary conditions and material properties – that will be needed for finite-element simulation. Like Fie, Tr3 is implemented in Fortran and runs under GNU/Linux, and Microsoft Windows 95 and later.

It can be downloaded from <http://audilab.bmed.mcgill.ca/~funnell/AudiLab/sw/tr3.html>. A screenshot from this software is provided in Figure 5.4.

5.5.1 Mesh

Due to software limitations, our mesh is generated using triangular thin-shell elements. It represents all the middle-ear structures of interest, including the TM, the ossicles, ligaments, and muscles. Mesh generation using solid elements, such as tetrahedra, would better represent these structures; however, this model was limited to the simpler elements due to the difficulties of volume mesh generation and the current limitations of our mesh generator and finite-element analysis program (SAP IV).

Each element node has six degrees of freedom corresponding to translation and rotation about each axis. Clamping, or fixing, a node eliminates its degrees of freedom.

The mesh resolution of a structure is defined in terms of the number of elements per diameter (or xy -resolution) and the slice spacing (or z -resolution). It plays an important role in the behaviour of the finite-element model. Larger mesh resolutions imply more nodes, and greater accuracy for model geometry and displacement. Such a mesh also demands greater computation time due to the increase in the sizes of the matrices used for the calculation process. On the other hand, smaller mesh resolutions imply fewer elements and smaller computation time. This resolution, however, limits model accuracy and generally reduces the calculated displacements.

The triangular elements can be of arbitrary shape, although ideally they should be nearly equilateral. Triangles that are too thin cause numerical problems, and also create wrinkling that increases the effective stiffness and overestimates the surface areas of the structures, as can be seen in Figure 5.6. Funnell (1984b) observed that

“n [the number of sections] should be made only as large as necessary to adequately describe the variations in shape from section to section, and ...k [the number of elements

per diameter] should then be made large enough that the widths of the triangles are comparable to (or smaller than) their heights.”

The ideal mesh resolution is one which fairly represents the geometry of all the structures of interest, and yields sufficiently accurate simulation results with the least amount of computation time. The results of experiments done during the preliminary stages of our modelling to relate computation time and mesh resolution are discussed in Chapter 6.

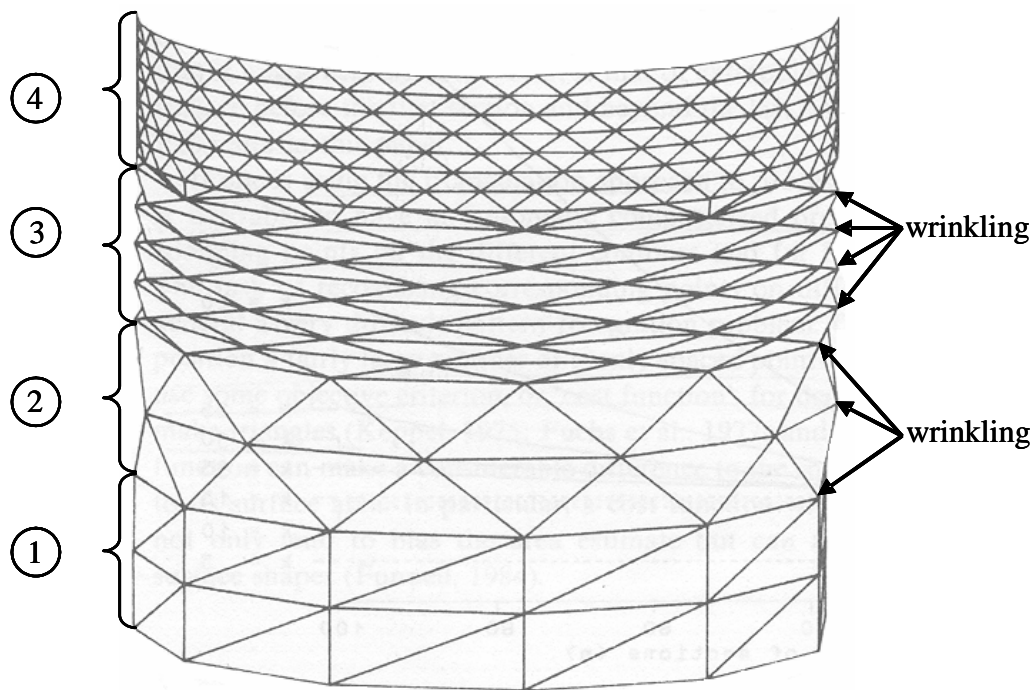


Figure 5.6 A cylinder triangulated using 4 different resolutions. (1) Bottom layer: 2 sections, triangulated with a 11 elements per diameter. Corresponding nodes in different slices are aligned above one another. (2) Same resolution as bottom layer but nodes are staggered, hence wrinkling. (3) Number of sections triangulated is increased to 8. Width of triangle much larger than its height, hence increased wrinkling. (4) Increased number of elements per diameter to 40. Element height is approximately equal to element width and wrinkling is greatly reduced. (After Funnell, 1984)

5.5.2 Bandwidth

A matrix comprises zero and non-zero elements that are generally dispersed throughout its rows and columns. Its bandwidth is defined as the band of maximum width of non-zero numbers lying along the matrix's diagonal. Therefore, generally, larger matrices have larger bandwidths.

Computation time also increases with the increase in bandwidth. In the finite-element package (SAP IV), an algorithm that can take advantage of the banded nature of a matrix is used. Therefore, for the same size of a matrix, matrix inversion will be faster if the bandwidth is smaller. In finite-element simulations, this time is mainly dependent upon the stiffness matrix, hence our attempt to minimize its bandwidth via a bandwidth minimization programme named *bwm*. This programme renumbers the nodes, using the algorithm of Crane *et al.* (1976), in such a manner that the bandwidth is minimized. For the case of our dataset, the bandwidth based on the node numbering from Tr3 was reduced in one particular case from 1609 to 239, i.e., by 85%.

5.6 SENSITIVITY ANALYSIS

To determine the most influential model parameters, we observed the model's behaviour in response to variations in nine of its parameter values: (1) the Young's modulus (Y) of the pars tensa, pars flaccida, anterior malleal ligament, superior malleal ligament, posterior incudal ligament, incudostapedial joint, and stapes annular ligament (or Y_{PT} , Y_{PF} , Y_{AML} , Y_{SML} , Y_{PIL} , Y_{ISJ} , Y_{SAL} , respectively), and (2) the thickness (T) of the pars flaccida and pars tensa (or T_{PF} and T_{PT} , respectively). One at a time, these parameters were set to $\frac{1}{4}$, $\frac{1}{2}$, $1\frac{1}{2}$ and 2 times their nominal values. Because of the surprisingly small effects that Y_{SAL} and Y_{ISJ} turned out to have in this range, we expanded the testing range for these two parameters. The results of this analysis are presented in Chapter 7.

CHAPTER 6

THE FINITE-ELEMENT MODEL

6.1 INTRODUCTION

This chapter presents the finite-element model that we developed for the human middle ear. The mesh is composed of thin-shell elements. For simplicity, we assumed all structures to be isotropic and homogeneous with linear elastic responses. Section 6.2 describes the preliminary version of the model, with details on each structure's thickness, material properties, and mesh resolution. This is followed by Section 6.3 where we discuss this model's convergence results. Section 6.4 defines the final model.

6.2 PRELIMINARY MODEL

This version of the model, depicted in Figure 6.1, is composed of the tympanic membrane (pars tensa and pars flaccida), malleus, incus, stapes, anterior malleal ligament, superior malleal ligament, both bundles of the posterior incudal ligament, tensor tympani tendon and muscle, stapedius tendon, and stapes annular ligament.

6.2.1 Tympanic Membrane

The eardrum model comprises the pars flaccida and the pars tensa. Distinction was made between the two regions, despite the difficulties we faced in identifying them because of the noisy dataset and the low resolution. The membrane has an xy -resolution of 10 or 20, and a z -resolution of 1, 4, or 8. The higher z -resolutions were assigned to regions where the eardrum's shape changed significantly across the slices. The pars flaccida was given a Young's modulus of 20 MPa and a uniform thickness of 200 μm (Ladak and Funnell, 1995). For the pars tensa, the Young's modulus and thickness were set to 40 MPa and 75 μm , respectively (Kirikae, 1960).

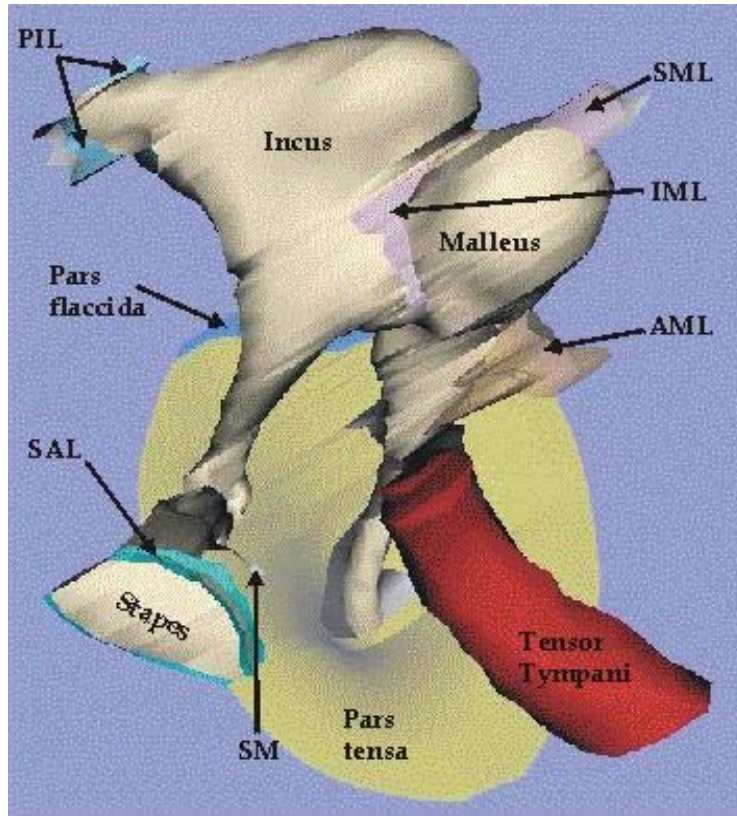


Figure 6.1 A VRML representation of the preliminary version of our complete middle-ear model.

The noisy dataset made it difficult to determine the exact boundaries and position of the eardrum. This created undesired wrinkling and an increase in structure stiffnesses, hence the need for smoothing. First, the endpoints of the contours shaping the pars flaccida and pars tensa were smoothed in Fie across slices to give the eardrum a smooth outline. Next, the entire curved conical surface was smoothed in Fie via a spline-fitting algorithm, thereby reducing wrinkles.

The fibrocartilaginous ring is a practically rigid ring (Wijhe, 2000) which was omitted from our model. The eardrum was therefore directly clamped at its endpoints, representing the ring attachment to the walls of the external auditory canal.

6.2.2 Ossicles

The malleus, incus and stapes were all given a Young's modulus of 200 MPa (Funnell *et al.*, 1992). This value is typical of bone and is so high that the ossicles are practically rigid.

The contours pertaining to the three ossicles were identified using the snake algorithm and a two-threshold grey palette, both of which were provided in Fig.

6.2.2.1 Malleus

Contours representing the malleus were assigned one of four thicknesses, depending on the malleus region which they defined. The thicknesses were 200 μm at the head, 63 μm at the neck, 90 μm at the manubrium, and 10 μm at the anterior process. We determined these values by averaging malleus thicknesses as measured in the micro-CT slices. The mesh resolution within the bone varies slightly, depending on sudden changes in its curvature. The mesh has an average resolution of 15 elements/diameter and a slice spacing of 2 or 4.

6.2.2.2 Incus

The average thicknesses of incus-related contours are as follows: the body 156 μm , short process 145 μm , long process 36 μm , and lenticular process 21 μm . These values were deduced from the micro-CT slices. The mesh has an average resolution of 15 elements/diameter and a slice spacing of 4.

6.2.2.3 Stapes

The stapes of this dataset has an atypical shape: an unusually thick posterior crus and an unusually small gap between the crura; however, this probably is not of any significance in the low-frequency range to which we are limiting our analysis. The thicknesses assigned to its contours were: head 42 μm , posterior and anterior crura 21 μm , and footplate 31 μm . This structure's mesh has approximately 10 elements/diameter and a slice spacing of 4.

6.2.3 Ligaments and Joints

6.2.3.1 Malleal ligaments

The superior (SML) and anterior malleal ligaments (AML) have a Young's modulus of 20 MPa (Funnell, 1996). Their element thicknesses are 63 μm , and they have an xy -resolution of 20 elements/diameter, at a slice spacing of 4.

At one end these ligaments are attached to the malleus, and at the other they are clamped (i.e., constrained to have zero displacements and rotations) to represent their attachment to the cavity wall.

The lateral malleal ligament was not included in our model because (1) a structure which may have resembled it was only seen in few (3 or 4) slices of the dataset, and its boundaries were not clearly identifiable, and (2) it has not been used in some former models (e.g., Koike *et al.*, 2002; Prendergast *et al.*, 1999). The posterior malleal ligament was also excluded, since it was only reported by two out of the six references we reviewed in Chapter 2, and was unidentifiable in this dataset.

6.2.3.2 Incudal ligaments

The posterior incudal ligament (PIL) is represented by two separate bundles, both of which were given a Young's modulus of 20 MPa and an average thickness of 47 μm . Given their simple structure, they were assigned an xy -resolution of 15 elements/diameter, and an average slice spacing of 4.

Since the superior incudal ligament was not identifiable in this dataset and was only mentioned by a few authors (FCAT, 1998; Proctor, 1989), we did not include it in our model.

6.2.3.3 Stapes annular ligament

The stapes annular ligament (SAL) is connected to the stapes footplate on one side, and is clamped on the other where it is attached to the oval window. In this model, the ligament was assigned a low Young's modulus (Y_{SAL}), 0.49 MPa, based on the work of Koike *et*

al. (2002). To deduce a physiologically reasonable value, they used three isolated stapes models which were identical with the exception of Y_{SAL} 's value; Y_{SAL} was set to 3.7 MPa, 0.49 MPa, or 0.065 MPa. The slope of the acoustic impedance of each model was then compared to that measured by Merchant et al. (1996). The ligament Young's modulus of the model with the slope closest to that of Merchant et al. was then selected (0.49 MPa).

The ligament's mesh resolution is 3 elements/diameter and it has a slice spacing of 4. Based on the micro-CT slice measurements, its thickness was set to 20 μm .

6.2.3.4 Ligament attaching the TM to the malleus

As already mentioned in Chapter 2, this connection (shown in Figure 6.2) has been described as being composed of dense fibrous tissue at its umbo and short process ends, and weak mucosal filaments in the mid-region (Gulya & Schuknecht, 1995). Assuming that these stronger regions are similar in composition to other middle-ear ligaments, we gave them a Young's modulus of 20 MPa. The weaker region was then assigned $1/10^{\text{th}}$ the Young's modulus, i.e., 2 MPa. Both regions were triangulated using an xy -resolution of 10 elements/diameter, an average z -resolution of 4 slices, and a thickness of 35 μm .

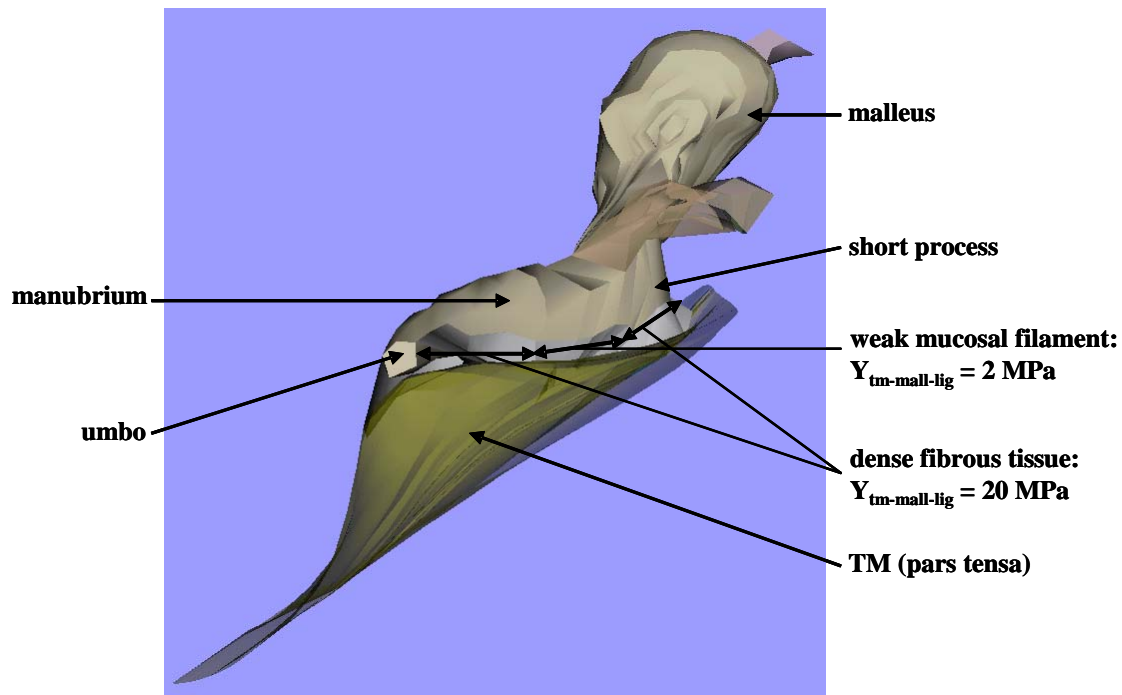


Figure 6.2 A VRML model of the TM, the malleus, and the TM-malleus attachment. The attachment's ends, near the umbo and near the short process, are strong and fibrous, unlike the weaker mid-region.

6.2.3.5 Incudomalleolar joint

At low frequencies the malleus and incus move as a single body (Kirikae, 1960; Gundersen *et al.*, 1976; Huttenbrink *et al.* 1986). Therefore, in this model, we assigned the joint a large stiffness of 100 MPa. Its thickness and xy - and z -resolutions were set to 50 μm , 15 elements/diameter and 4 slices, respectively.

6.2.3.6 Incudostapedial joint

We gave the incudostapedial joint a Young's modulus of 50 MPa (Siah, 2002) and a thickness of 21 μm . Its average xy - and z -resolutions are 4 elements/diameter and 2 slices, respectively.

6.2.4 Muscles and Tendons

No muscle activity is present in cadaver or temporal-bone studies. Therefore, we assigned the model's muscles (tendons) a low Young's modulus, 2 MPa. The tensor tympani

muscle (and tendon) has an xy -resolution of 15 elements/diameter and a z -resolution of 4. The stapedius muscle (and tendon) has an xy -resolution of 5 elements/diameter, and a z -resolution of 4.

6.3 CONVERGENCE TEST

Convergence testing was performed on our preliminary middle-ear model. In each simulation either the numbers of elements per diameter or the slice spacings of all the structures were changed by the same factor. This was followed by analysis of the TM and stapes displacements and of the time required for each simulation. Based on these two factors, we were able to determine a suitable mesh resolution.

6.3.1 Number of Elements Per Diameter and Displacements

Five different resolutions were chosen for the convergence test with respect to the number of elements per diameter, or xy -resolution. Results of this test are summarized in Figures 6.3 and 6.4.

TM displacements reach a plateau region beyond a mesh size of 5016 elements. A small variation (approximately 2.2%) can be seen between the displacements at 5016 and 6008 elements.

The stapes displacement rises to within 91.3% of its value at 6008 elements at a mesh resolution of 2975 elements. The slight drop at 6008 elements presumably reflects a sensitivity of the stapes displacement to small details of the meshes of some parts of the model that change as the resolution changes.

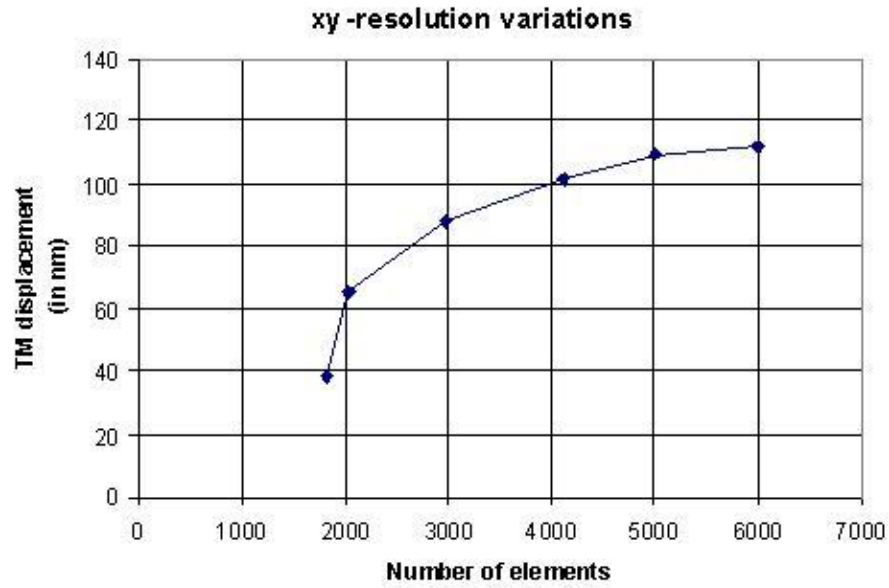


Figure 6.3 Convergence test for the middle ear: *xy*-resolution and corresponding maximum pars-tensa displacement.

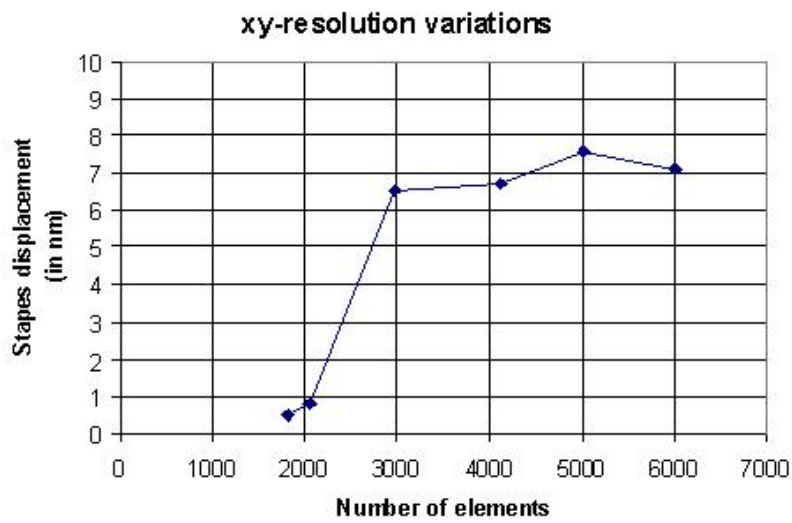


Figure 6.4 Convergence test for the middle ear: *xy*-resolution and corresponding maximum stapes displacement.

6.3.2 Slice Spacing and Displacements

Three different z -resolutions were used to determine an acceptable z -resolution, or slice spacing. As seen in Figures 6.5 and 6.6 below, TM and stapes displacements both decrease with an increase in z -resolution. The reason for the drop in displacement may be that the slice spacing becomes very small compared with the size of the elements along the diameter (Fahle and Palme, 1983). As previously mentioned (Section 5.5.1), this contributes to an increase in wrinkling and thus in stiffness of the model, thereby reducing its displacement. The higher z -resolution causes drops in the TM and stapes displacements of 12.4% and 61.2%, respectively. Therefore, to represent the structures reasonably well but to avoid excessive wrinkling, it was decided to use the z -resolution corresponding to a mesh of 4115 elements.

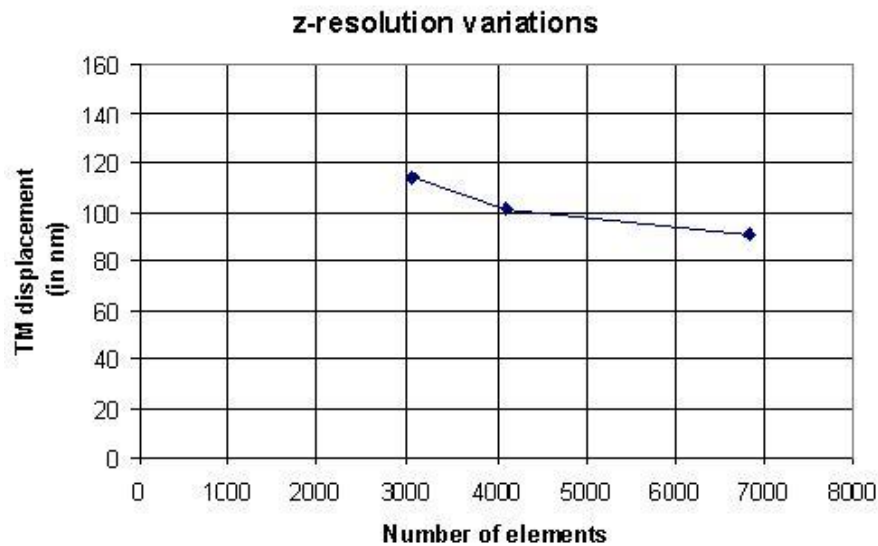


Figure 6.5 Convergence test for the middle ear: z -resolution and corresponding maximum pars-tensa displacement. Increasing the number of elements from 4115 to 6848 creates a drop of 12.4% in pars tensa displacement.

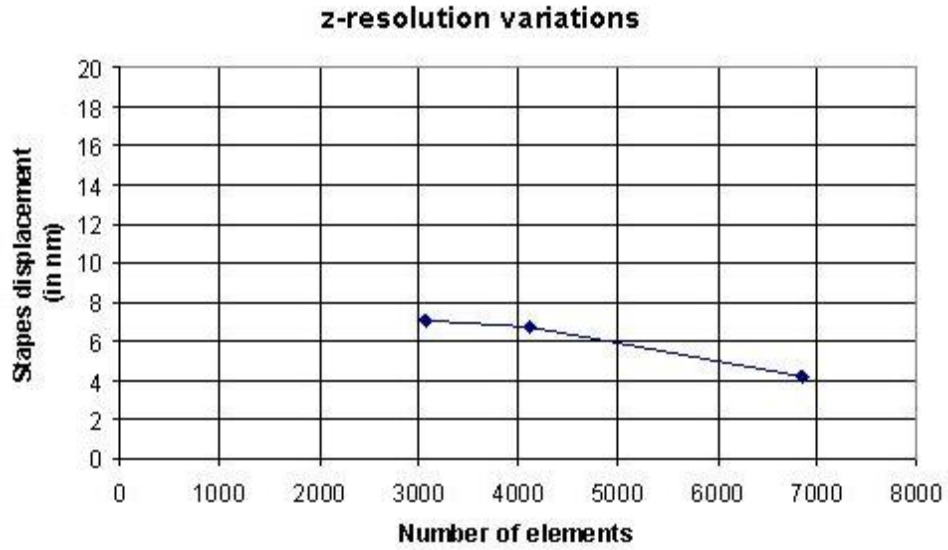


Figure 6.6 Convergence test for the middle ear: z -resolution and corresponding maximum stapes displacement. Increasing the number of elements from 4115 to 6848 creates a drop of 61.2% in stapes displacement.

6.3.3 The Selected Mesh

This preliminary mesh comprises 4115 thin-shell elements and 2015 nodes. Although higher resolutions may have shown more accurate responses, Figure 6.7 reveals that, with little additional increase in the mesh's resolution, computation would have become much more expensive.

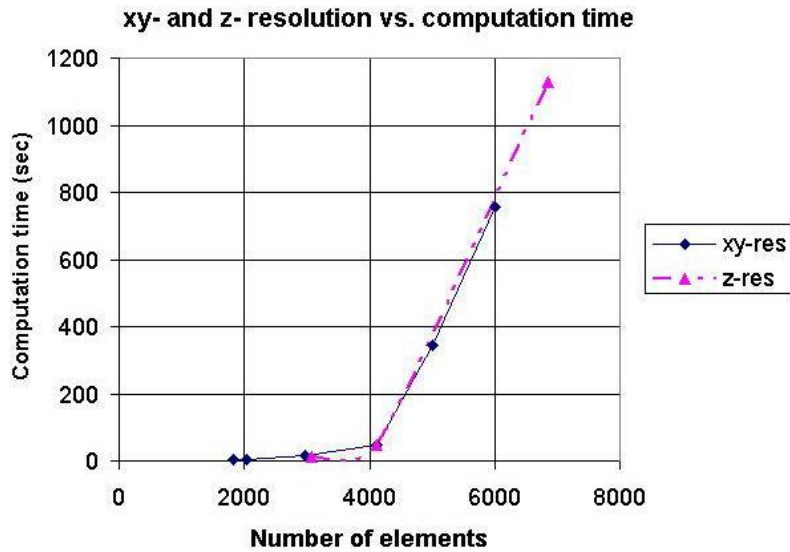


Figure 6.7 The effect of the preliminary model’s mesh resolution on computation time. Using a mesh of 5000 elements or more becomes computationally expensive. For every 1000 additional elements, computation time increases by 400 seconds.

6.4 THE FINAL MODEL

After selecting the mesh resolution of the preliminary model, three changes were made to create the final model, which is seen in Figure 6.8. These changes were in the stapedial annular ligament, the incudomalleolar joint, and the muscles. Convergence was not retested for the model, and the previously mentioned resolutions were used. Since some structures were excluded here, the mesh was reduced to 3831 thin-shell elements and 1871 nodes.

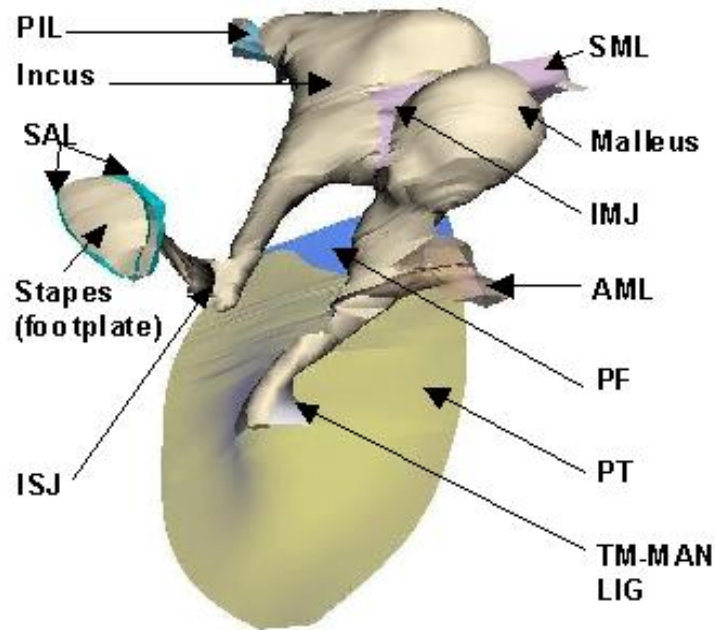


Figure 6.8 A VRML representation of the final version of our model. The two model versions are identical in terms of structure, with the exception of the tensor tympani tendon and muscle and the stapedius muscle, which we excluded from the revised model seen here.

6.4.1 Stapedial Annular Ligament

In the modified model, we chose to use the Young's modulus deduced by Lynch *et al.* (1982), 10 kPa, which was also used by Sun *et al.*, 2002). This value seems to be better justified than the previous value of 0.49 MPa. Lynch *et al.* estimated the Young's modulus using the experimentally measured compliance of the stapes, the surface area of the footplate, and dimensions of the annular space and oval window. De Souza *et al.* (1991) have reported seeing elastin-related fibres in histological slices of this ligament. Because of the elastin, this ligament's stiffness would be expected to be much lower than that of the other ligaments in our model.

Another value that has been used for this ligament is 65 kPa (Prendergast *et al.*, 1999).

6.4.2 Incudomalleal Joint

Because the incudomalleal joint is generally considered to be rigid at low frequencies, we decided to completely fix the joint. We set its Young's modulus to that of the bones which it joins, i.e., to 200 MPa.

6.4.3 Muscles

The Dalhousie measurements to which we are comparing our model's response were done on a cadaver temporal bone, so the muscles were not active. Studies done on live but deeply anaesthetized animals, also with no muscle activity, have shown that removing the middle-ear muscles has no effect on middle-ear response (Rosowski *et al.*, 2004). We therefore excluded both muscles from the model.

6.5 LOADING

A unit pressure was applied normal to the surface of the entire tympanic membrane to represent static loading. Such a load is comparable to low audio frequencies, e.g., 100-300 Hz, where the inertial and damping effects can be neglected.

The stapes load is a combination of two individual loads: the load of the stapes annular ligament and the load of the cochlear liquid. Since the cochlear load may be represented as a damper (e.g., Koike *et al.*, 2002), this implies that it can be ignored in our low-frequency model, leaving only the effect of the stapes annular ligament.

CHAPTER 7

RESULTS

7.1 INTRODUCTION

This chapter presents the responses of the final middle-ear model. Section 7.2 presents simulated TM and footplate displacements. Section 7.3 presents an evaluation of the sensitivity of the model to its parameters. A comparison is then made between our model's results and existing experimental measurements in Section 7.4. Another comparison follows in Section 7.5, this time between our model's results and those of other models. The chapter concludes with a discussion in Section 7.6 where we comment on our observations and speculate about possible causes for differences between the response of our model and other existing responses.

7.2 DISPLACEMENTS OF THE FINITE-ELEMENT MODEL

This section will include many screen shots taken from the post-processor Fod, a home-grown programme implemented in Fortran. It displays the results of simulations made in the finite-element programme SAP IV. Displacements for each material type are listed on the left side, along with the direction along which the displacements are measured (e.g., DW 0), the number of displacement contours, the angle at which the model is rotated from its original position, and the model's volume displacement. Contours on the structures indicate iso-displacement contours; the range of displacements is represented by a colour scale.

7.2.1 Eardrum Displacements

Figure 7.1 shows the pattern of eardrum displacements (both pars flaccida and pars tensa). The pars flaccida moves by a maximum of 38.3 nm. On the pars tensa there are two displacement maxima, in the posterior and anterior portions of the membrane. The larger of the two is in the posterior region and displaces by 109.1 nm.

As expected, smaller displacements are seen around the mid-region of the TM (Figure 7.1) where it attaches to the manubrium, extending from point A to point D. No membrane displacement increases are observed in the TM regions which are weakly connected to the manubrium (i.e., between points B and C of Figure 7.1).

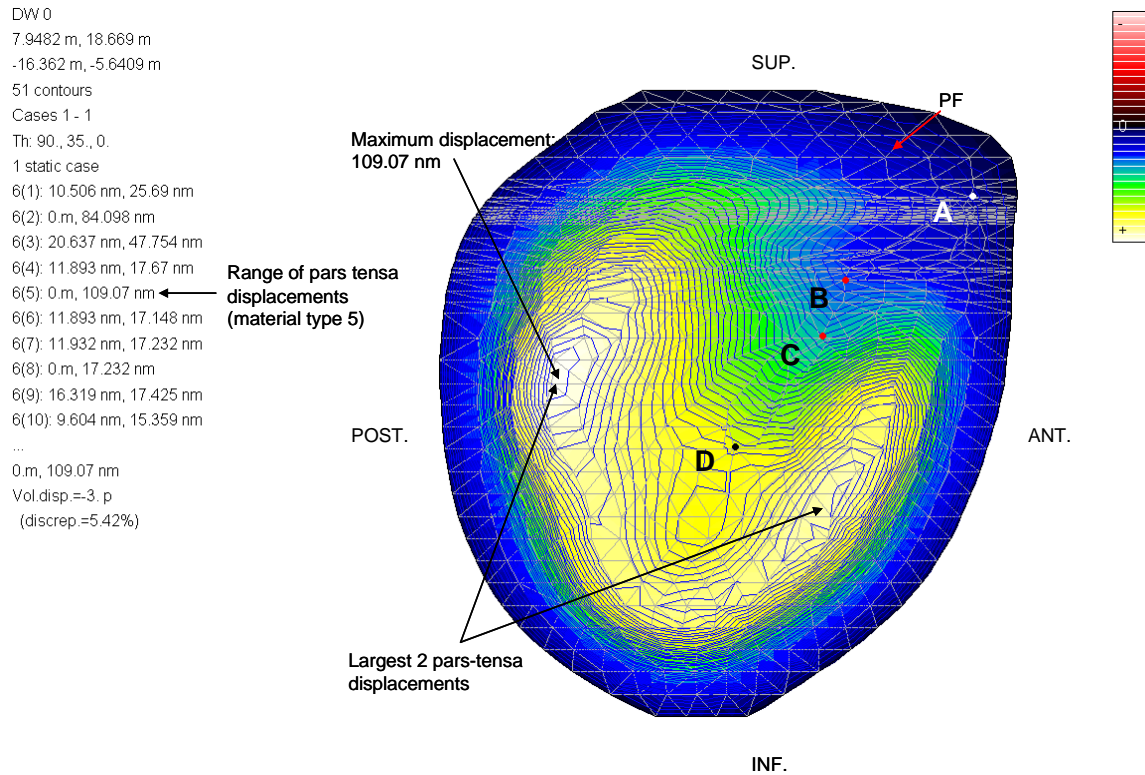


Figure 7.1 Magnitude (DW 0) of the TM's response (medial view) to a static pressure of 1 Pa as viewed in Fod. The pars flaccida (PF) moves very little and pars tensa displacement is the greatest in the posterior (POST.) and anterior (ANT.) regions. The TM-malleus attachment extends from the malleus' lateral process (point A) to the umbo (point D). The weak mid-region of this attachment extends from point B to point C. SUP: superior; INF: inferior.

Equidistant displacement contours along the manubrium in Figure 7.2 indicate that there is no manubrial bending. The maximum manubrial displacement, 84.1 nm (see Figure 7.2), is at the umbo, which also corresponds to point D of Figure 7.1.

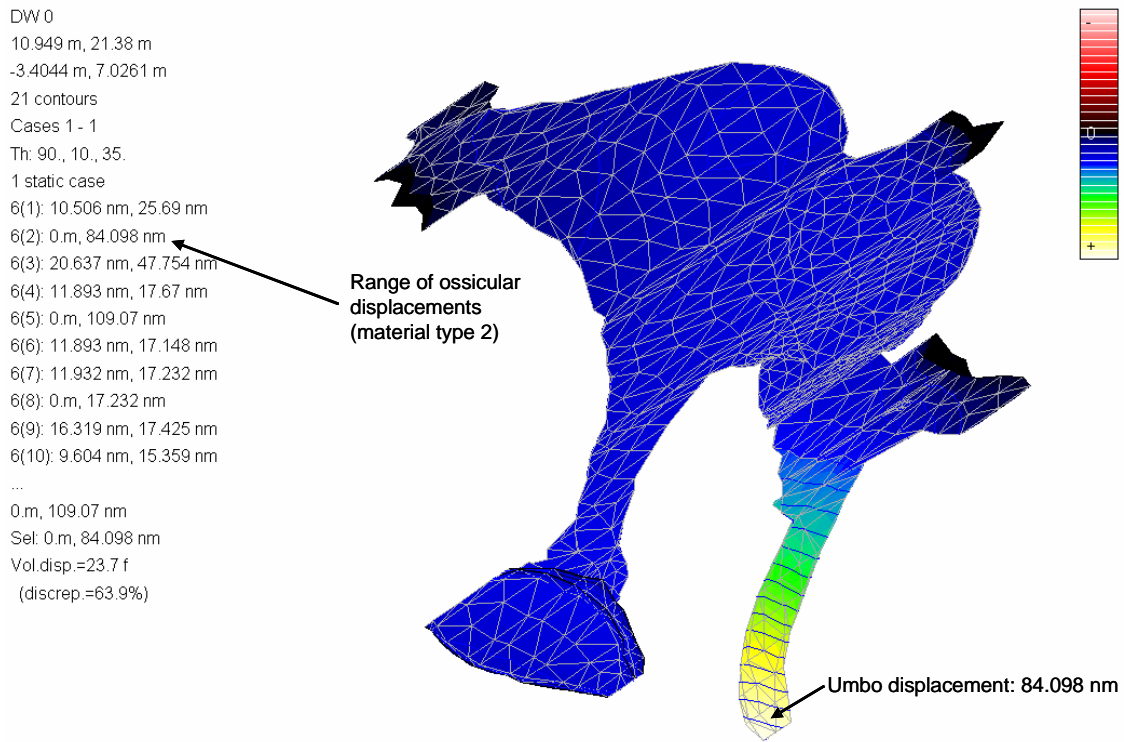


Figure 7.2 A medial view of ossicular chain displacement. Maximum displacement is at the umbo (~ 84.1 nm).

7.2.2 Axis of Rotation and Incudomalleolar Displacements

Figure 7.3 shows a medial view of the ossicles as they rotate about the imaginary axis of rotation. The magnitudes of their displacements range from 0 nm (at the clamped ligament ends) to 84 nm at the umbo. This axis extends from the posterior incudal ligament to the superior portion of the malleus head.

From the displacement vectors of the final model shown in Figures 7.4 and 7.5, we can see that the malleus and incus rotate about an axis that is slightly lateral to the middle-ear structures and parallel to the axis mentioned above.

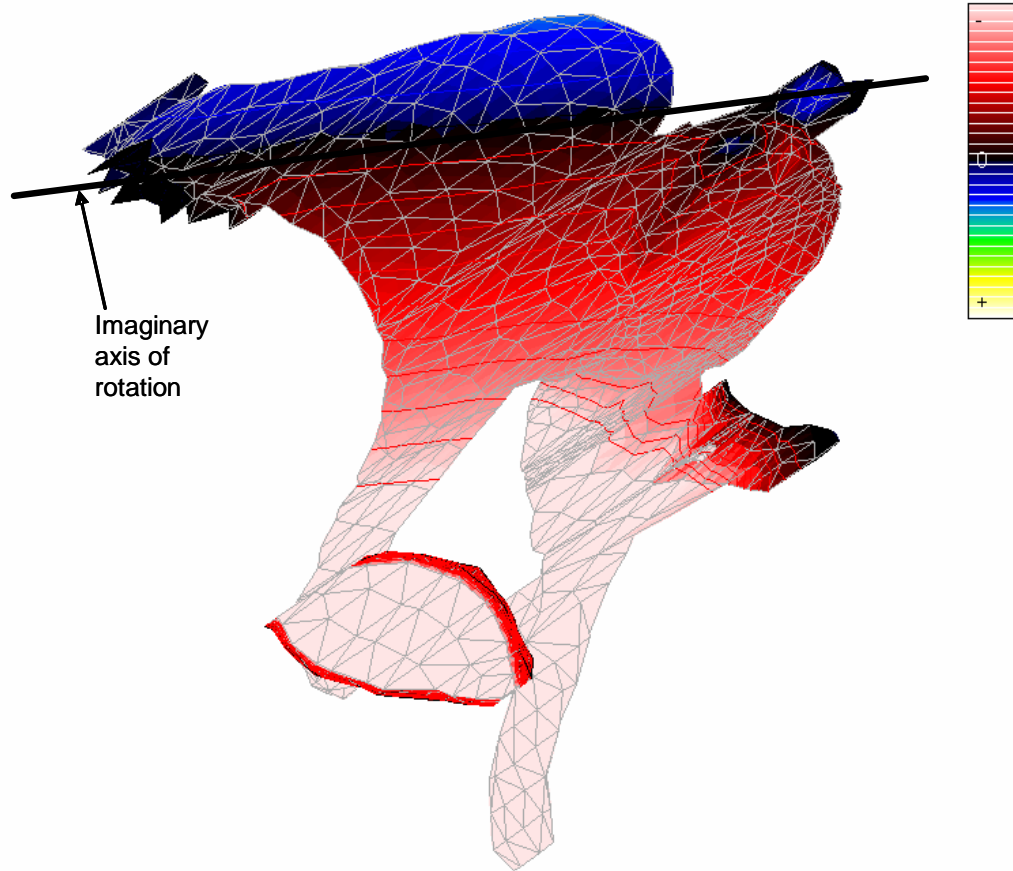


Figure 7.3 Ossicular displacements along the direction that is normal to the footplate (and page). The imaginary axis of rotation is indicated by the region with zero displacement (seen in black). This axis passes through the posterior incudal ligament to the superior portion of the malleus head. The parts above it move out of the page (towards the reader) while those below it move into the page (away from the reader).

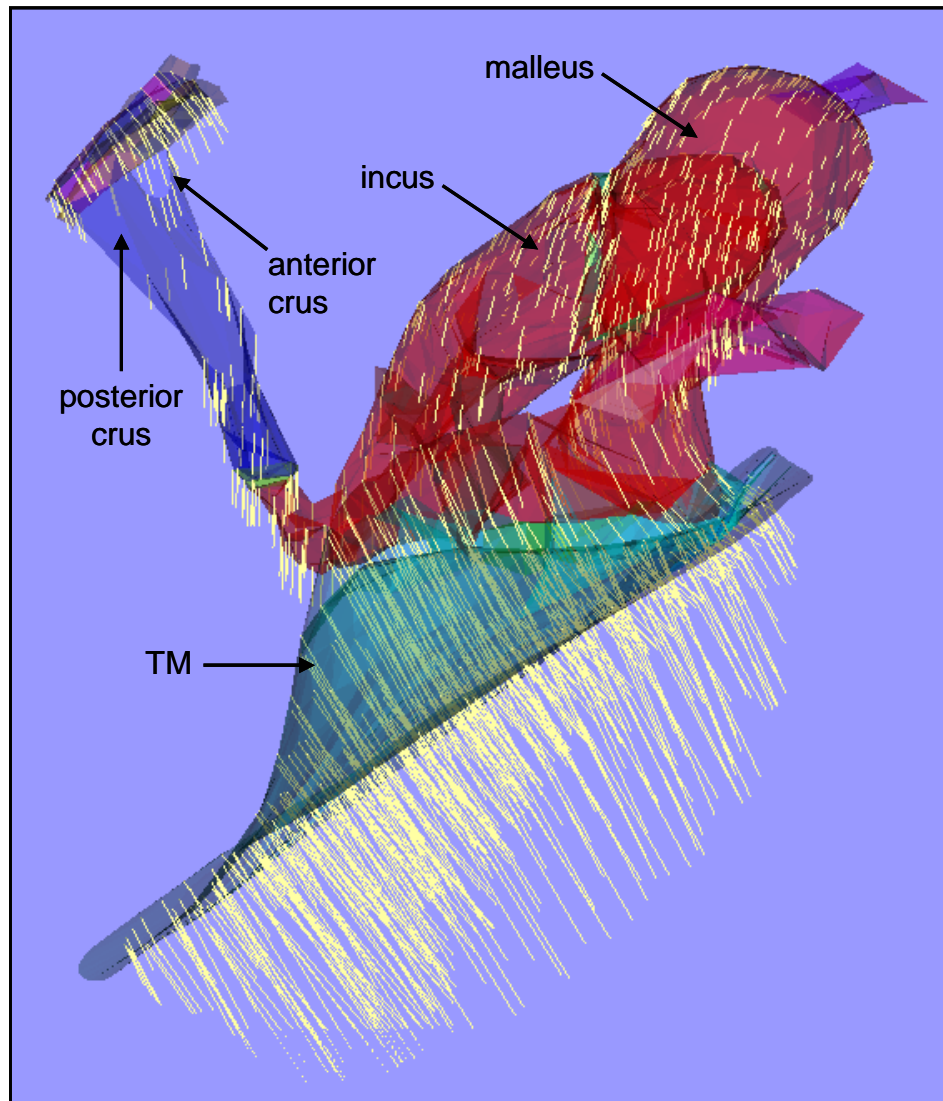


Figure 7.4 A VRML model of the middle ear (supero-anterior view) shows malleus and incus rotation about a distant axis to the right of the malleus and parallel to the classical axis of rotation. Predominantly piston-like displacements at the footplate can also be seen.

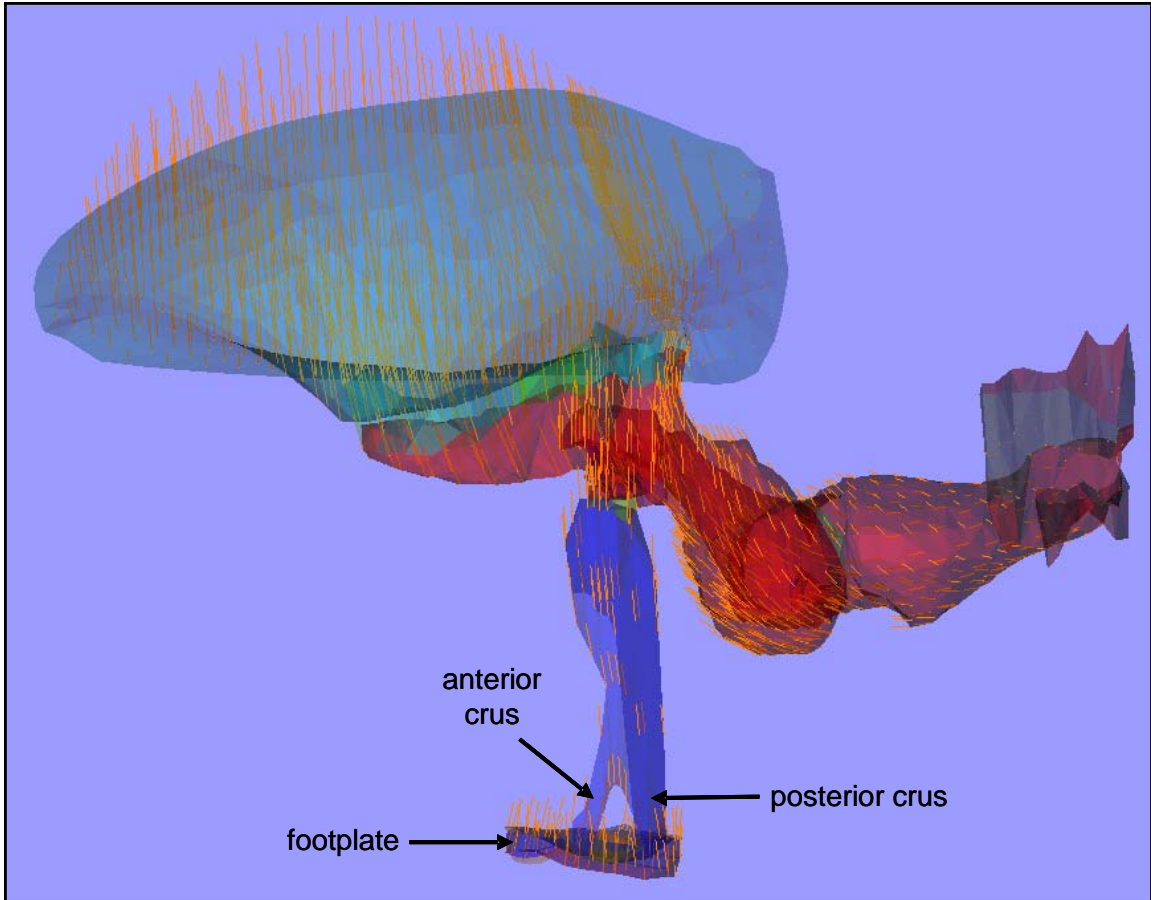


Figure 7.5 Displacement vectors at the footplate are normal to the surface implying overall piston-like motion for the stapes (supero-medial view).

7.2.3 Stapes Displacement

As seen in Figure 7.4, the angles that the displacement vectors form with the stapes gradually decrease medially, i.e., from the head and down the crura, indicating some stapes rotation. At the footplate, these vectors are approximately normal to the surface, implying predominantly piston-like motion for the stapes footplate.

Figure 7.6 shows a medial view of the magnitudes of ossicular displacement patterns. The maximum magnitude of displacement at the footplate is 17.23 nm. Figure 7.7 provides a medial view of the ossicular-displacement component which is normal to the footplate surface. Maximum footplate displacement along this direction is equivalent to 16.47 nm. These two values (17.23 nm for the vector magnitude and 16.34 nm for the

perpendicular component) are very similar, implying that there is little footplate motion in other directions.

A slight difference in displacement between the superior and inferior regions of the footplate is also noticeable in Figures 7.6 and 7.7. This implies that the footplate is rotating; the axis of rotation is closer to the inferior footplate region. This axis is also parallel to the long axis of the footplate since the iso-displacement contours along the footplate surface are parallel to the long axis. Furthermore, because the entire range of displacements is of the same sign (positive), we conclude that the axis of rotation does not lie within the footplate. The piston-like displacement is still dominant.

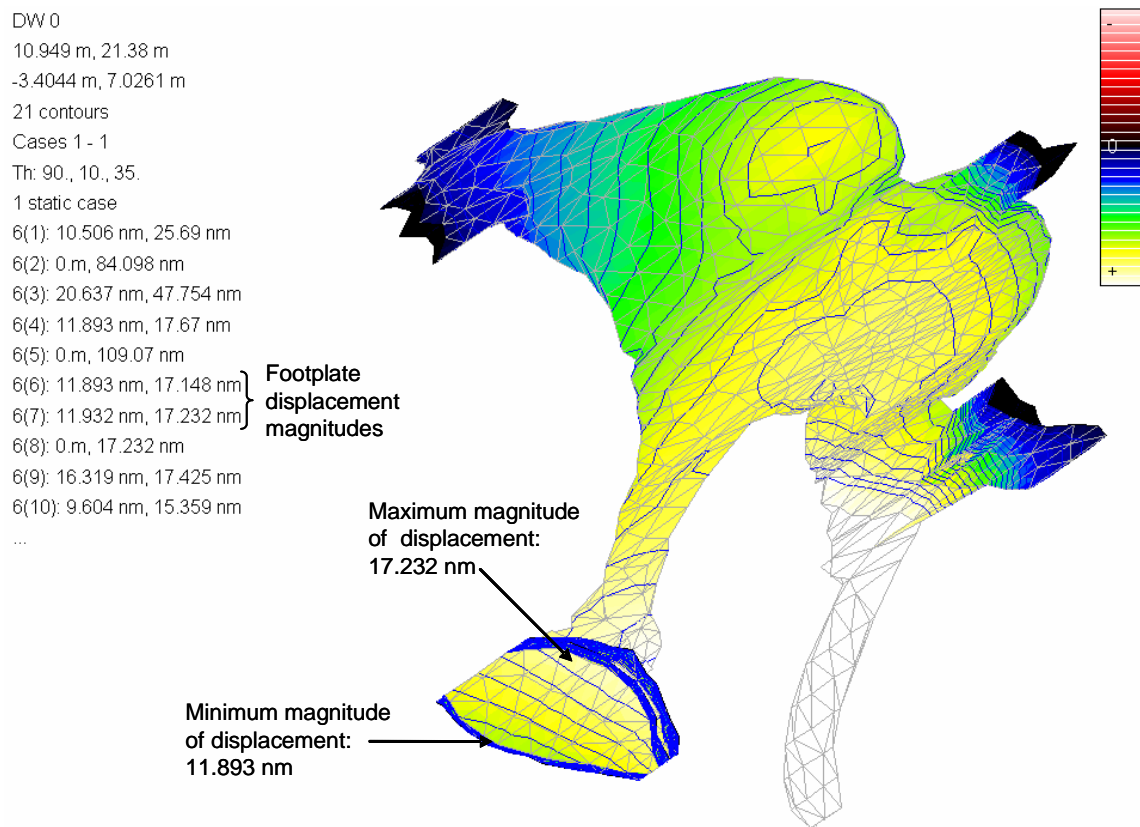


Figure 7.6 Middle-ear response shows varying magnitudes of displacement across the footplate (material types 6 and 7). The minimum magnitude is 11.9 nm and the maximum magnitude is 17.2 nm.

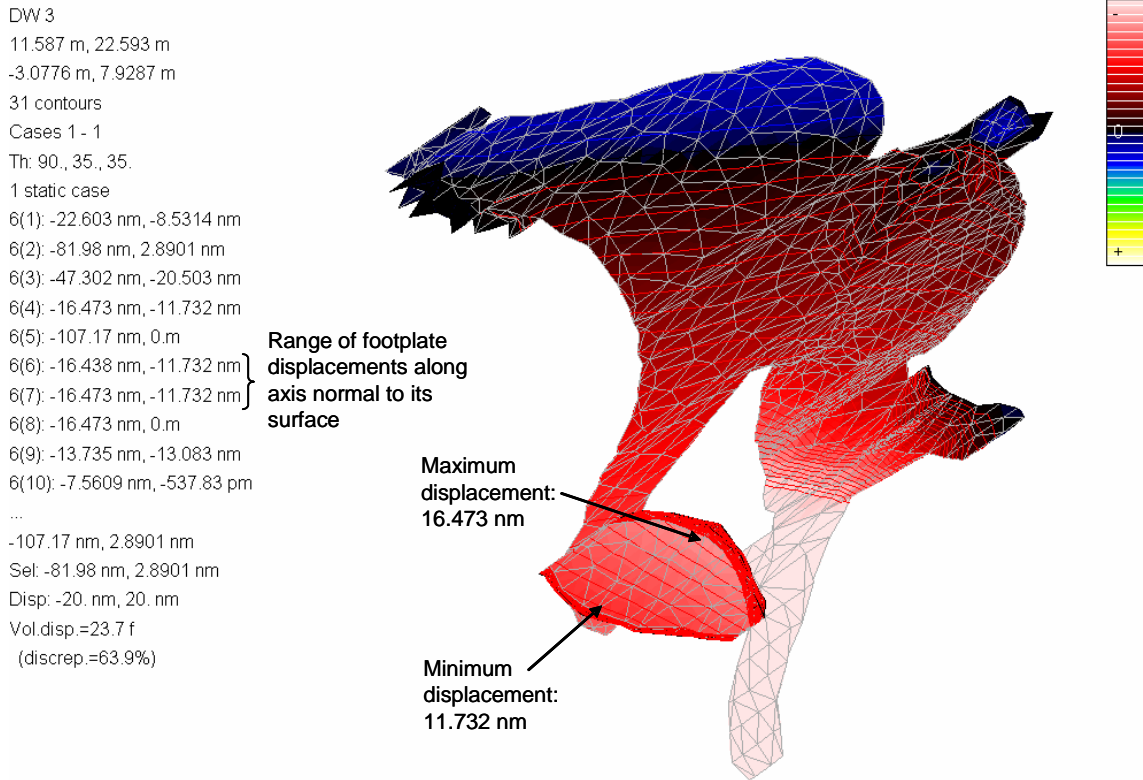


Figure 7.7 Displacement of the ossicles along an axis that is normal to the footplate. Footplate displacements (of material types 6 and 7) range from 11.732 nm to 16.473 nm.

7.3 PARAMETER SENSITIVITY

7.3.1 Sensitivity Analysis

The sensitivity of the model to nine of its parameters (mentioned in Section 5.6) is summarized in Figures 7.8 and 7.9. The focus is on the response of the pars tensa and the stapes footplate. In Figure 7.8, we see that the parameters with the greatest effect on pars-tensa displacement are T_{PT} and Y_{PT} , in decreasing order. Decreasing these parameters' values to $\frac{1}{4}$ of their nominal values, for example, will increase pars-tensa displacements by a factor of 2.3 and 3.8, respectively. The remaining seven parameters have relatively little effect.

The parameters which most influence pars-tensa displacement also influence footplate displacement most (Figure 7.9), although less so. Decreasing their parameter values here

to $\frac{1}{4}$ of their nominal values only increases displacements by factors of 1.8 and 2.5. Less influential are the parameters T_{PF} , Y_{SML} , Y_{PF} , and Y_{AML} (with a maximum factor of 1.4); they have greater effect on the stapes than they do on the pars tensa. The parameters Y_{PIL} , Y_{SAL} and Y_{ISJ} had insignificant effects.

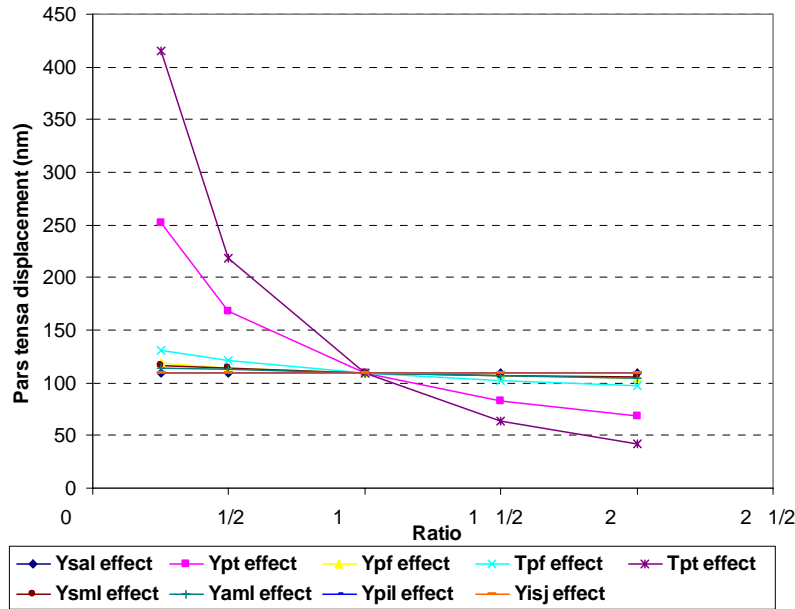


Figure 7.8 Sensitivity of the pars tensa (or TM in general) to nine parameters at $\frac{1}{4}$, $\frac{1}{2}$, $1\frac{1}{2}$, and 2 times their nominal values.

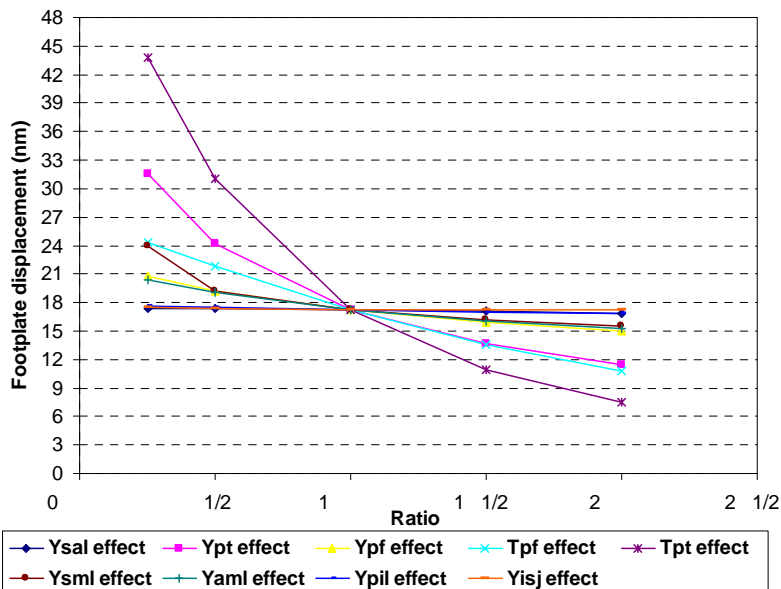


Figure 7.9 Footplate sensitivity to nine parameters at $\frac{1}{4}$, $\frac{1}{2}$, $1\frac{1}{2}$, and 2 times their nominal values.

Two of the apparently important structures, the incudostapedial joint and the stapedial annular ligament, seem in this analysis to have little effect on footplate displacement. We therefore decided to explore the individual effects of their Young's moduli (Y_{ISJ} and Y_{SAL}) beyond the initially chosen ranges.

Figure 7.10 shows that footplate displacement steadily increases for incudostapedial joint stiffness values (Y_{ISJ}) up to 1.5 MPa, then drops slightly. This is presumably because (1) a too-flexible joint causes loss of energy at the joint and, in turn, reduces footplate displacement; and (2) a too-stiff joint requires excessive sideways footplate displacement and leads to reduced motion in the direction normal to the footplate. Changes in the stiffness beyond 25 MPa have very little or no effect on the footplate's displacement.

The result of expanding the range of Y_{SAL} is plotted in Figure 7.11. Footplate displacement is insensitive to changes in Y_{SAL} values between about 2.5 kPa and 20 kPa. Smaller stiffness values simulate greater annular-ligament flexibility and permit slightly greater displacement. On the other hand, higher stiffness values simulate increasing degrees of fixation, hence the significant progressive drop in the footplate's response.

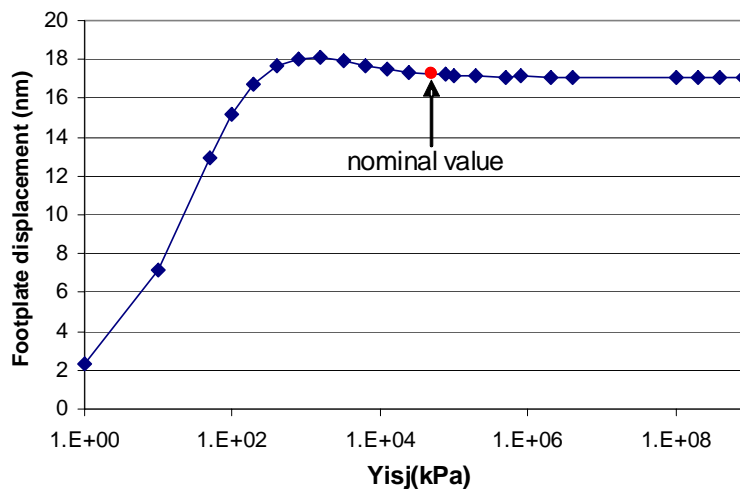


Figure 7.10 Footplate displacement is highly sensitive to Y_{isj} values varying between 1 MPa and 1.5 MPa, and much less sensitive to those varying between 25 MPa and 800 GPa.

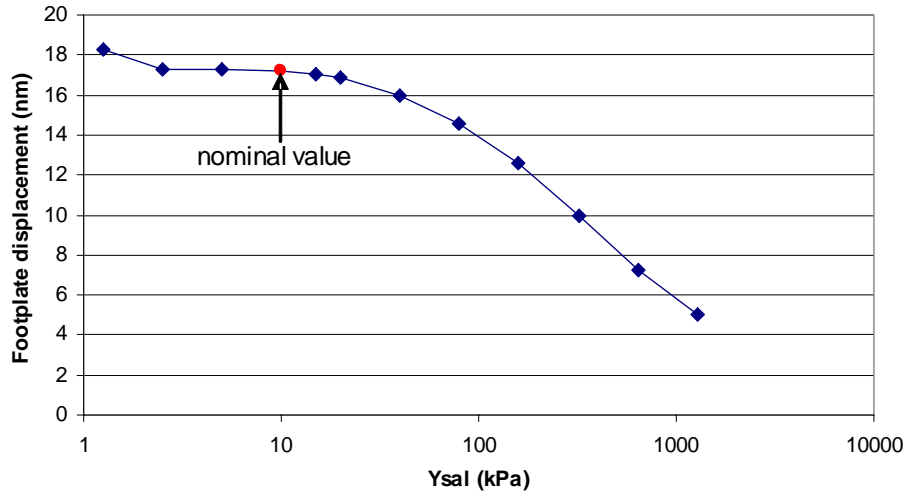


Figure 7.11 Increasing the stiffness of the stapes annular ligament (Y_{sal}) beyond 20 kPa increases the degree of fixation and limits footplate displacement.

7.3.2 Effect of TM-Malleus Attachment

Koike *et al.* (2002) found that weakening the mid-region of the TM-malleus attachment in his latest model, by a factor of 1000, had no effect on the overall middle-ear response. For testing purposes, we generated a finite-element model that was identical to our final model with the exception of the Young's modulus of the middle region of the TM-malleus attachment; this value (in the test model) was set to 20 MPa, the same as for the upper and lower regions of the attachment.

Comparing the TM, umbo and stapes responses of the two models (one of which had a weakened mid-region at the attachment) showed practically identical behaviour for both models. Therefore, as Koike *et al.* concluded, weakening the mid-region of the TM-malleus attachment has no effect on the overall middle-ear response.

7.4 COMPARISON WITH EXPERIMENTAL MEASUREMENTS

To evaluate our model's response, it is essential to first compare it with the response of the same ear measured using LDV. We shall also compare it with other experimental responses, all of which have been discussed in Chapter 3. The quantitative comparisons

are between the displacements of our model and the corresponding normalized (to 1 Pa) peak displacements summarized in Tables 3.1, 3.2 and 7.1.

Correlation of our model’s response with Bance's measurements in the same middle ear is essential as one of the goals of our work is to avoid the effects of ear-to-ear variability. Displacements for our model and for the actual ear are listed in Table 7.1, along with percentage differences between the two.

Our model’s TM displacement is similar to that of the actual ear, differing by approximately 22.4% (~2.2 dB). The response of our umbo is approximately 46% (~3.4 dB) greater than the corresponding experimentally measured value.

The stapes of our finite-element model displaced by 17.2 nm, and that of the actual specimen displaced by 29 nm (at its centre). Therefore, the simulated and averaged experimental responses of the same middle ear differ by 40.7% (~4.5 dB).

	Response of final finite-element model (in nm/Pa)	Average LDV measurements (in nm/Pa)	% Difference between model and specimen
TM (pars tensa)	109.1	140.6	22.4%
Umbo	84.1	57.4	46%
Footplate	17.2	29.0	40.7%

Table 7.1 Maximum simulated and experimental 0-to-peak displacements at the TM, umbo and footplate of the same ear.

It is also important to compare our model with other experimental findings pertaining to the middle ear. As we saw in Figure 7.1, the model’s two largest displacements are in the posterior and anterior regions of the TM. This is consistent with the findings of Dirckx and Decraemer (1991), for example. The maximum TM response of our model, however, differs from theirs; they reported a displacement that is 6.6 times greater than ours,

probably related to the fact that their measurements were pseudo-static whereas Bance's measurements and our model involve low audio frequencies. We did not observe extra membrane complications across the region which connects to the manubrium (i.e., between points A and D of Figure 7.1), as did Dirckx and Decraemer (1991) at low pressures.

Umbo displacement of our model (84.1 nm) falls in the middle of the corresponding experimentally measured range (from 13.7 nm to 200.7 nm) of Table 3.1. In Figures 7.4 and 7.5, we saw that the model's overall footplate motion is piston-like. Similar observations at low frequencies have been reported in the literature (e.g., Gyo *et al.*, 1987; Huber *et al.*, 2001). Our simulated footplate displacement (17.2 nm) also lies between the two corresponding displacements reported in Table 3.1 (10.6 nm and 89.2 nm).

A comparison of the models' umbo/stapes displacement ratios indicates large differences. The reported experimental ratios are between 1.9 (Bance, Dalhousie University) and 2.2 (Dirckx and Decraemer, 1991), while ours is 4.9.

7.5 COMPARISON WITH OTHER FINITE-ELEMENT MODELS

Our model's peak displacements are in fair agreement with the peak model displacements summarized in Table 3.2. A difference of less than 3 nm exists between the TM displacements of Gan *et al.* (2004) (111.9 nm) and that of our model (109.1 nm). Umbo displacements of the cited models fall between 28.3 nm and 74.3 nm while our corresponding displacement is 84.1 nm, close to their upper limit. As for stapes displacement, that of our model (17.2 nm) is close to the lower limit of the corresponding tabulated model displacements (23 nm to 70.7 nm).

7.6 DISCUSSION

The displacements of our model lie within or close to the ranges of displacements reported in the literature but our umbo/stapes ratio is higher than expected.

Our axis of rotation does not correspond to the classical axis. The incudal end corresponds to its classical location reported in the literature for low frequencies, but its malleal end is higher than expected. Several factors may have contributed to this unexpected position. For example, we may have overestimated the thickness and/or stiffness of the SML. This could limit motion in the malleal head area, hence raising the location of the axis of rotation. Modeling an AML that is thinner or less stiff than what has been reported in the literature could also affect the position of the axis of rotation. This would lead to a wider range of motion (or greater freedom for displacement) for the lower portions of the malleus. Another possible influence is our exclusion of the LML from the model (because it was unidentifiable). Doing so may have given the inferior incudal and malleal portions less stability in the middle-ear space, hence the rise in the location of the axis. The unexpected position of the axis of rotation may also account for the unexpectedly high umbo/stapes displacement ratio.

Different structure material properties, structure thicknesses, and ligaments in our model and other models presumably contributed to the differences in their responses. Regarding our model and the experimental studies, inter-ear variability and cavity status can have an impact. Aritomo and Goode (1987) reported individual differences in umbo and stapes displacements to be greater than 2 times at low frequencies. Differences between the authors we reference in Chapter 3 are even greater (a factor of ~14 difference between the maximum and minimum umbo displacements).

CHAPTER 8

CONCLUSION

8.1 SUMMARY

The goal of this work was to generate a finite-element model of a human middle ear. We based it on accurate geometry and *a priori* material-property estimates from the literature.

A human temporal bone was obtained and its dynamic response was measured by Bance (Ear & Auditory Research Laboratory, Dalhousie University) by means of laser Doppler vibrometry. It was then scanned by us using x-ray micro-CT. The middle-ear structures were carefully outlined via manual and semi-automatic segmentation techniques and reconstructed to form a 3-D model. All structures were assigned material-property values which were obtained from the literature.

The final finite-element model consists of the tympanic membrane (pars flaccida and pars tensa), the three middle-ear ossicles, and three ligaments (superior malleolar ligament, anterior malleolar ligament and posterior incudal ligament). To simulate loading, the entire tympanic-membrane surface was subjected to a static pressure of 1 Pa.

By convergence testing, we determined an appropriate overall mesh resolution taking the computation-time factor into consideration.

To validate our model, we compared its overall vibration pattern (at the pars tensa, umbo and stapes) with both simulated and experimentally measured low-frequency data from the literature; the data include measurements for the same middle ear. Some ambiguity was present in what several groups were measuring (whether zero-to-peak, peak-to-peak, or rms values). During this process, no iterative alterations were made in the material-property values for matching model and reported data.

Our model's displacements differ by a maximum factor of 1.5 (~4.5 dB, at the umbo) from those measured on the same ear.

When compared with the displacements measured experimentally by other groups, the model's pars-tensa, umbo and stapes displacements lie within the corresponding reported ranges. They are, however, slightly outside the ranges of simulated displacements reported for the models of other groups. Such small differences, however, have been discussed and accepted in the literature.

The classical axis of rotation extends from the anterior process of the malleus to the posterior incudal ligament. That of our model, however, was parallel and lateral to a line which extended from the superior portion of the malleus head to the posterior incudal ligament. We believe that this may have been caused by the wrong choice of malleal ligament thicknesses and/or material properties.

Stapes motion was predominantly piston-like, with minor footplate rocking, consistent with experimental observations.

The sensitivity of the finite-element model to several parameters was also investigated. We found that T_{PT} and Y_{PT} have the greatest influence on pars-tensa and stapes displacements. Parameters with insignificant influence are Y_{PIL} , Y_{SAL} , and Y_{ISJ} . The remaining parameters have intermediate effects, but greater on the stapes than on the pars tensa. In a separate study, we saw that a model with a uniform Young's modulus across the entire TM-malleus attachment produces the same response as does a model with a weaker mid-region attachment

8.2 FUTURE WORK

The next steps in this project involve several enhancements to our current model. These include the following:

- The triangulation programme that we are currently using generates meshes made of shell elements. In the future, however, it would be better to represent the structures of our model (except for the TM) by solid elements. This will yield more realistic structures, hence more accurate displacements. A convergence test following this would also be of interest.

- This study focused on the (low-frequency) response of the middle ear. For a more complete analysis of the model, however, dynamic analysis across the audible frequency range is essential. Since the model's behaviour was limited to low frequencies, damping and inertial effects were neglected. To investigate a wider range of frequencies, we will need to take structure mass and damping coefficients into consideration.
- As a preliminary investigation, we only studied the effects of ten parameters on the behaviour of our model. Sensitivity analysis involving all the model's parameters should still be done. The ranges within which these parameters are varied also need to be extended for a broader analysis.
- Several methods have been developed for studying parameter sensitivity. The full-factorial method and the method of Taguchi (1987) are capable of determining interactions between parameters; the Taguchi method, however, can determine them with fewer simulations, and is therefore more efficient. We were the first to apply this approach to a middle-ear model (Qi *et al.*, 2004a,b). To test its applicability, we studied the effects of nine parameters (Y_{PT} , T_{PT} , P_{PT} , Y_{PF} , T_{PF} , Y_{LIG} ¹, Y_{IMJ} , Y_{ISJ} , Y_{SAL}) and four interactions (Y_{PT} and T_{PT} , Y_{PT} and Y_{LIG} , Y_{PF} and P_{PT} , and Y_{IMJ} and Y_{ISJ}). A total of 16 simulations were run, where the nine parameters under investigation were varied by $\pm 50\%$ of their initially estimated values. We observed that T_{PT} and Y_{PT} have the greatest effects on TM volume displacements, while T_{PT} , Y_{PT} , T_{PT} , and Y_{LIG} have the greatest effects on footplate displacements (41.2% and 21.0%, and 17%, respectively). We also found a strong interaction between the Young's moduli of the incudomalleal and incudostapedial joints.
- Given the comparability between the responses of other models and ours, we see that this technique is very promising. We believe that it should also be applied to models of other ear specimens (of humans or other species).
- To closely represent structure geometry, we used a combination of manual and semi-automatic segmentation. Additional structure smoothing in the future will help refine the model. Recently analysed details of incudostapedial coupling

¹ Y_{LIG} corresponds to the Young's modulus of the SML, AML, and PIL.

(Siah, 2002; Funnell *et al.*, in press) and the footplate (Hagr *et al.*, 2004) should also be incorporated.

REFERENCES

Abel EW, Lord RM, Mills RP (1998): “Magnetic resonance imaging in the measurement of the ossicular chain for finite element modeling” Proceedings of the 20th Annual International Conference of the IEEE Engineering in Medicine & Biology Society, 20(6), 3170-3172

Aritomo H (1989): “Ossicular vibration in human temporal bones” J. Oto-Rhino-Laryngol. Soc., Japan, 92, 1359-1370

Aritomo H, Goode RL (1987): “Cochlear input impedance in fresh human temporal bone” 91st Meeting, American Academy of Otolaryngology, Chicago Research Forum (as cited by Koike *et al.*, 2002).

Ayache N (1995): “Medical computer vision, virtual reality and robotics” Image and Vision Computing, 13 (4), 295-313

Bathe KJ (1982): “*Finite Element Procedures in Engineering Analysis*” Prentice-Hall, New Jersey

Becker AA (2004): “*An Introductory Guide to Finite Element Analysis*” ASME Press, 51-64

Beer HJ, Bornitz M, Drescher J, Schmidt R, Hardtke HJ, Hofmann G, Vogel U, Zahnert T, Hüttenbrink KB (1996): “Finite element modelling of the human eardrum and applications” Proceedings of Middle ear mechanics in Research and Otorhinolaryngology, Dresden, 40-47

von Békésy G (1960): “*Experiments in Hearing*” New York, McGraw Hill

Bess FH, Humes LE (1995): “*Audiology: The Fundamentals 2nd Edition*” Baltimore: Williams & Wilkins

Caselles V (1995): “Geometric models for active contours” IEEE proceedings of Int. Conf. on Image Processing, (3) 9-12

Cohen LD (1991): “On active contour models and balloons” Computer Vision, Graphics, and Image Processing: Image Understanding, 53 (2), 211-218

Cook RD, Malkus DS, Plesha ME (1989): “*Concepts and Applications of Finite Element Analysis 3rd edition*” John Wiley and Sons, New York

Courant R (1943): “Variational Methods for the Solution of Problems of Equilibrium and Vibrations” Bulletin of the American Mathematical Society, 49

Crane Jr. HL, Gibbs NE, Poole Jr. WG, Stockmeyer PK (1976): “Algorithm 508. Matrix bandwidth and profile reduction” ACM Trans. Math. Software 2, 375-377, Complete source in “*Collected Algorithms*” from ACM

Cross H (1932): “Analysis of Continuous Frames by Distributing Fixed-End Moments” Trans ASCE, 96, 1-10

Clough RW (1960): “The Finite Element Method in Plane Stress Analysis” Proceedings, American Society of Civil Engineers, Second Conference on Electronic Computation, Pittsburgh

Dafydd Gibbon, Roger Moore, Richard Winski, eds. (1997): “*Handbook of Standards and Resources for Spoken Language Systems*” Mouton de Gruyter, Berlin, New York

Decraemer WF, Khanna SM, Funnell WRJ (2000): “Measurement and modelling of the three-dimensional vibration of the stapes in cat” Proc. Internat. Symp. on Recent

Developments in Auditory Mechanics (Sendai, Japan, 1999 July), World Scientific Pub., US, UK, Singapore, 36-43

Desai CS, Abel JF (1972): "*Introduction to the Finite-Element Method: A Numerical Method for Engineering Analysis*" Van Nostrand Reinhold, New York

Dirckx JJJ, Decraemer WF (1991): "Human tympanic membrane deformation under static pressure" *Hear. Res.*, 51, 93-106

Eiber A (1996): "Mechanical modeling and dynamic investigation of middle ear" proceedings of Middle ear mechanics in Research and Otorurger, Dresden, 61-66

Federative Committee on Anatomical Terminology (FCAT) (1998): "*Terminologica Anatomica: International Anatomical Terminology*" Thieme, Stuttgart New York, 150

Ferris P, Prendergast PJ (2000): "Middle-ear dynamics before and after ossicular replacement" *Journal of Biomechanics*, 33, 581-590

Fung YC (1965): "*Foundations of Solid Mechanics*" Prentice Hall, Englewood Cliffs, N.J., 353

Funnell WRJ (1975): "*A theoretical study of eardrum vibrations using the finite-element method*" Ph.D. Thesis, McGill University, Montréal

Funnell WRJ (1984a): "On the choice of a cost function for the reconstruction of surfaces by triangulation between contours" *Comp. and Struct.*, 18, 23-26

Funnell WRJ (1984b): "On the calculation of surface areas of objects reconstructed from serial sections" *Journal of Neuroscience Methods*, 11, 205-210

Funnell WRJ (1996a): “Finite-element modelling of the cat middle ear with elastically suspended malleus and incus” 19th Midwinter Res. Mtg., Assoc. Res. Otolaryngol., St. Petersburg Beach

Funnell WRJ (1996b): “Low-frequency coupling between eardrum and manubrium in a finite-element model” J. Acoust. Soc. Am., 99, 3036-3043

Funnell WRJ (2001): “High-frequency time-domain behaviour of a finite-element model of the eardrum” 24th Midwinter Res. Mtg., Assoc. Res. Otolaryngol., St. Petersburg Beach

Funnell WRJ, Decraemer WF, Khanna SM (1987): “On the damped frequency response of a finite-element model of the cat eardrum” J. Acoust. Soc. Am., 81(6), 1851-1859

Funnell WRJ, Khanna SM, Decraemer WF (1992): “On the degree of rigidity of the manubrium in a finite-element model of the cat eardrum” J. Acoust. Soc. Am., 91, 2082-2090

Funnell WRJ, Laszlo CA (1978): “Modelling of the cat eardrum as a thin shell using the finite-element method” J. Acoust. Soc. Am., 63, 1461-1467

Funnell WRJ, Laszlo CA (1982): “A critical review of experimental observations on eardrum structure and function”, O.R.L. 44(4), 181-205

Funnell WRJ, Siah TH, McKee MD, Daniel SJ, Decraemer WF (in press): “On the coupling between the incus and the stapes in the cat”, preprint of article accepted for J. Assoc. Res. Otolaryngol., September 2004.

Fuse T, Aoyagi M, Koike Y, Sugai Y (1992): “Diagnosis of the ossicular chain in the middle ear by high-resolution CT” O.R.L. J. Otorhinolaryngol. Relat. Spec. 54, 251-254

Galerkin BG (1915): "Series Solution of Some Problems of Elastic Equilibrium of Rods and Plates" in Russian *Vestn. Inzh. Tekh.* 19

Gallagher, Richard H (1975): "*Finite Element Analysis: Fundamentals*" Prentice-Hall, Inc., Englewood Cliffs, New Jersey, 135-185

Gan RZ, Feng B, Sun Q (2004): "Three-dimensional finite element modeling of human ear for sound transmission" *Annals of Biomedical Engineering*, 32(6), 847-859

Graham MD, Reams C, Perkins R (1978): "Human tympanic membrane, malleus attachment" *Ann. Otol. Rhin. Laryng.*, 87 (3), 426-432

Greene, RE, RE Jones, RW McLay, DR Strome (1969): "Generalized Variational Principles in the Finite-Element Method" *AIAA J.*, 7 (7), 1254-1260

Guinan JJ, Peake WT (1967): "Middle-ear characteristics of anesthetized cats" *J. Acoust. Soc. Am.*, 41, 1237-1261

Gulya AJ & Schuknecht HF (1995): "Anatomy of the temporal bone with surgical implications 2nd edition" Parthenon Press, Pearl River, New York

Gundersen T, Hogmoen K (1976): "Holographic vibration analysis of the ossicular chain." *Acta otolaryngol.* 82, 16-25

Gyo K, Aritomo H, Goode RL (1987): "Measurements of the ossicular vibration ratio in human temporal bones by use of a video measuring system" *Acta. Otolaryngol.*, Stockholm, 103, 87-95

Hagr AA, Funnell WRJ, Zeitouni AG, Rappaport JM (accepted 2003 Nov 19): "High-resolution x-ray CT scanning of the human stapes footplate" *J. Otolaryngol.*

Ham AW, Cormack DH (1979): "*Histology*", JB Lippincott Company, 8th edition, 12-16

Hariharan P (2003): "*Optical Intereferometry 2nd edition*" Elsevier Science, 201-206

Hatamzadeh-Tabrizi J (2003): "*Using Active Contours for Segmentation of Middle-ear Images*" Master's thesis, McGill University, Montréal

Heiland K, Goode R, Asai M, Huber A. (1999): "A human temporal bone study of stapes footplate movement" *Am. J. Otol.* 20,81-86

Helmholtz HLF (1869): "The mechanism of the middle-ear ossicles and of the eardrum" *Plfügers Archiv. f. Physiol., Bonn*, 1, 1-60, (German). Translated by Buck AH and Smith N, Wood W, New York, 69 pp., 1873 and by Hinton J, Publ. New Sydenham Soc. London, 62, 97-155 1874

Hendee WR, Ritenour R (1992): "*Medical Imaging Physics 3rd edition*" Mosby-Year Book, 414-428

Henson MM (2001): "The human tympanic membrane: Smooth muscle in the region of the annulus fibrosus" 24th Midwinter Res. Mtg., Assoc. Res. Otolaryngol., St. Petersburg Beach

Henson OW Jr., Henson MM (2000): "The tympanic membrane: highly developed smooth muscle arrays in the annulus fibrosus of mustached bats" *JARO*, 1(1), 25-32

Herrera DG, Maysinger D, Almazan G, Funnell WRJ, Cuello AC (1997): "Quantification of CFOS and glial fibrillary acidic protein in (GFAP) expression following topical application of potassium chloride to the brain surface" *Brain Res.*, 784, 71-81

Herrera D, Maysinger D, Funnell WRJ, Cuello AC (1991): "Quantification of c-fos and GFAP expression following topical application of KCl to the brain surface" 3rd IBRO World Cong, Neuroscience, Montréal

Huber A, Asai M, Ball G, Goode RL (1996): "Analysis of ossicular vibration in three dimensions" Proceedings of Middle ear mechanics in Research and Otorurger, Dresden, 82-87.

Huber A, Linder T, Ferrazzini M, Schmid S, Dillier N, Stoeckli S, Fisch U (2001): "Intraoperative assessment of stapes movement" Ann. Otol. Rhin. Laryng., 110 (1), 31-35

Hutton DV (2004): "*Fundamentals of finite element analysis*" McGraw Hill, Boston

Kass M, Witkin A, Terzopoulos D (1986): "Snakes: active contour models" International Journal of Computer Vision, 3, 321-331

Kelly DJ, Prendergast PJ, Blayney AW (2003): "The effect of prosthesis design on vibration of the reconstructed ossicular chain: A finite element analysis of four prostheses", Otolology & Neurotology, 24(1), 11-19

Kempe C, Stasche N, Barmann M, Foth HJ, Baker-Schreyer A, Hormann K(1996): "Laser Doppler velocimetry – a method supporting differential diagnosis of middle and inner ear disorders" Proceedings of Middle ear mechanics in Research and Otorurger, Dredsen, 95-99

Khanna SM, Decraemer WF (1996): "Vibration modes and the middle ear function" Proceedings of Middle ear mechanics in Research and Otorurger, Dredsen, 21-26

Khanna SM, Tonndorf J (1972): "Tympanic membrane vibrations in cats studied by time-averaged holography" J. Acoust. Soc. Am., 51 (6) 1904-1920.

Kirikae I (1960): "*The Structure and Function of the Middle Ear*" The University of Tokyo Press

Kobrak HG (1948): "Construction material of the sound conduction system of the human ear" J. Acoust. Soc. Am., 20, 125-130

Koike T, Wada H, Kobayashi T (2002): "Modeling of the human middle ear using the finite-element method" J. Acoust. Soc. Am. 111, (3), 1306-1317

Ladak HM, Funnell WRJ (1995): "On the effects of geometric nonlinearities in a finite-element model of the cat eardrum" Proc. IEEE EMBS 17th Annual Conference & 21st Can. Med. & Biol. Eng. Conf., Montréal, 1439-1440

Ladak HM, Funnell WRJ (1996): "Finite-element modelling of the normal and surgically repaired cat middle ear" J. Acoust. Soc. Am., 100, 933-943

Lemmerling MM, Stambuk HE, Mancuso AA, Antonelli PJ, Kubilis PS (1997): "CT of the normal suspensory ligaments of the ossicles in the middle ear" Am. J. Neuroradiol., 18, 471-477

Lesser THJ & Williams KR (1988): "The tympanic membrane in cross-section: A finite element analysis" J. Laryngol. Otol. 102, 209-214

Lobregt S, Viergever MA (1995): "A discrete dynamic contour model" IEEE Trans on Medical Imaging, 14 (1), 12-24

Lord Rayleigh (1870): "On the Theory of Resonance" Transactions of the Royal Society, London, A161

Lynch TJ, Nedzelnitsky V, Peak WT (1982): "Input impedance of the cochlea in cat" J. Acoust. Soc. A.M., 72, 108-130

Mach E., Kessel J (1872): “Die Funktion der Trommelhoehle und der Tuba Eustachii. Sitzungsber. Akad. Wiss Wien (Math.- Phys. Kl.) Abt.3, 66, 337-343

Malladi R, Sethian JA, Vemuri BC (1995): “Shape modelling with front propagation: A level set approach” IEEE Trans. on PAMI (17) 158-175

Maney GB (1915): “Studies in Engineering” No. 1, U. of Minnesota, Minneapolis, Minn

Merchant SN, Ravicz ME, Voss SE, Puria S, Peake WT, Rosowski JJ (1996): “Middle ear mechanics in normal, diseased and reconstructed ears” Proceedings of Middle ear mechanics in Research and Otosurgery, Dresden, , 175-182

Miller JV (1990): “*On GMD’s: Geometrically deformable models for the extraction of closed shapes from volume data*” Master’s thesis, Rensselaer Polytechnic Institute, New York

Mikhael CS, Funnell WRJ, Bance M (2004): “Middle-ear finite-element modelling with realistic geometry and *a priori* material-property estimates” Proc. 28th Ann. Conf. Can. Med. Biol. Eng. Soc., 2004

Nishihara S, Goode RL (1996): “Measurement of Tympanic Membrane Vibration in 99 Human Ears” Proceedings of Middle ear mechanics in Research and Otosurger, Dresden, 91-94

Noor AK (1991): “Bibliography of Books and Monographs on Finite Element Technology” Applied Mechanics Reviews 44, no. 6

Ostenfeld A (1926): “*Die Deformationsmethode*” Springer-Verlag OHG, Berlin

Prendergast PJ, Ferris P, Rice HJ, Blayney AW (1999): "Vibro-acoustic modelling of the outer and middle ear using the finite-element method" *Audiol. Neurootol.*, 4: 185-191

Proctor B (1989): "*Surgical Anatomy of Ear and Temporal Bone*" Thieme, New York

Qi L, Mikhael CS, Funnell WRJ (2004): "Application of the Taguchi method to middle-ear finite-element modelling" *Proc. 28th Ann. Conf. Can. Med. Biol. Eng. Soc.*

Relkin EM (1988): "Introduction to the analysis of middle-ear function" in "*Physiology of the Ear*" ed. Jahn AF and Santos-Sacchi J, Raven Press, New York, 103-123

Ritz W (1909): "Über eine neue Methode zur Lösung gewissen Variations-Probleme der mathematischen Physik." *J. Reine Angew, Math*, 135

Rosowski JJ, Huber AM, Ravicz ME, Goode RL (2004): "Are temporal bones useful models of human middle-ear mechanics?" *27th Midwinter Res. Mtg., Assoc. Res. Otolaryngol., Daytona Beach*

Siah TS (2002): "*Finite Element Modeling of the Mechanics of the Coupling Between the Incus and Stapes in the Middle Ear*" M.Eng. Thesis, McGill University, Montréal

Silverstein H (1972): "*Atlas of the human and cat temporal bone*" Thomas, Springfield, Illinois

Som PM, Curtin HD (1996): "Temporal bone embryology and anatomy" in "*Head and Neck Imaging 3rd edition*", 2, 1319-1321

Stytz M, Frieder G, and Frieder O (1991): "Three-dimensional medical imaging algorithms and computer systems" *ACM Computing Surveys*, 23 (4) 421-499

Sun Q, Gan RZ, Chang H.K., Dormer KJ. (2002): "Computer-integrated finite element modeling of human middle ear" *Biomechan. Model. Mechanobiol.*, 1, 109-122

Swartz JD (1983a): ".High-resolution computed tomography of the middle ear and mastoid, I: normal radioanatomy including normal variations" *Radiology* 148, 449-454

Swartz JD, Goodman RS, Marlowe FI, Wolfson RJ (1983a): "High-resolution computed tomography of the middle ear and mastoid, II: tubotympanic disease" *Radiology*, 148, 455-459

Swartz JD, Goodman RS, Russell KB, Landenheim SE, Wolfson RJ (1983b): "High-resolution computed tomography of the middle ear and mastoid, III: surgical altered anatomy and pathology" *Radiology*, 148, 461-464

Taguchi G (1987): "*System of Experimental Design*" UNIPUB Kraus International Publications, New York

Thompson TT (1985): "*A practical approach to modern medical imaging techniques 2nd edition*" Little Brown and Company, 169-190

Tonndorf J, Khanna SM (1970): "The role of the tympanic membrane in middle ear transmission" *Ann Otol Rhinol Laryngol.*, 79,743-753

Tonndorf J, Khanna SM (1972): "Tympanic membrane vibrations in human cadaver ears studied by time-averaged holography" *J. Acoust. Soc. Am.*, 52, 1221-1233

Wada H, Metoki T, Kobayashi T. (1992): "Analysis of dynamic behavior of human middle ear using a finite-element method" *J. Acoust. Soc. Am.* , 92, 3157-3168

Wever EG, Lawrence M (1954): "*Physiological Acoustics*" Princeton University Press, Princeton, New Jersey

van Wijhe RG (2000):” *A finite-element model of the middle ear of the moustached bat*”
Master’s thesis, McGill University, Montréal

Wolff D, Bellucci RJ, and Eggston AA. (1957): “*Mircoscopic anatomy of the temporal bone: A photographic survey of serial sections of the temporal bone cut in the three routine planes of sectioning human specimens*” The Williams & Wilkins Co., Baltimore

World Health Organization (WHO) (11 July 2001): “W.H.O. calls on private sector to provide affordable hearing aids in developing world” Press Release, WHO/34

Xu C, Prince JL (1997): “Gradient vector flow: a new external force for snakes” Proc. IEEE Conf. on Computer Vision and Pattern Recognition, 66-71

Yang X, Henson OW Jr. (2002): “Smooth muscles in the annulus fibrosus of the tympanic membrane: physiological effects on sound transmission in the gerbil” *Hear. Res.*, 164, 105-114

Zienkiewicz OC (1970): “Finite Element Method: From Intuition to Generality,” *Appl. Mech. Rev.*, 23, No. 23, March, 249-256

ALGOR. Pittsburgh: Algor Interactive Systems

ANSYS. Houston, PA: Swanson Analysis Systems Inc.

COSMOS/M. Los Angeles: Structural Research and Analysis Corp.

MSC/NASTRAN. Lowell, MA: MacNeal-Schwindler Corp.

<http://www.skyscan.be>

<http://www.ctlab.geo.utexas.edu/overview>

http://www.polytec.com/int/_files/LM_Vibrometry_Tutorial.pdf

http://www.polytec.com/int/158_942.asp